Präparation und Untersuchung von Submikrometer Strukturen auf der Basis magnetischer Dünnschichten

Dissertation

zur Erlangung des Grades
Doktor der Naturwissenschaften (Dr. rer. nat.)
am Fachbereich Physik
der Johannes Gutenberg-Universität Mainz

von
Nicole Auth
geb. in Mainz

Mainz, 2005

D 77

Preparation and study
of magnetic thin film based
sub-micron structures

Ph.D. thesis
by
Nicole Auth

universität mainz

Mainz, Germany 2005

Contents

List of Figures

List of Tables

Introduction

Fundamental research on magnetic storage techniques has developed into a broad field. During the last years a multitude of different approaches has emerged, starting from the optimisation of current fabrication processes to various methods of miniaturisation and the implementation of new material classes. Essentially they all follow a common aim: reduction of the minimum feature size, which is necessary in order to store one bit.

Since 1959 it was possible to achieve a doubling of the data density about every 18 month, generally known as Moore's Law. Several times its break-down has been predicted but due to the introduction of new technological concepts this trend continued. When inductive read/write heads became a limiting factor, spintronics entered the stage. Magnetoresistive heads, which exploit the giant magnetoresistive (GMR) effect became a tremendous success. With the discovery of colossal magnetoresistance (CMR) in oxide materials, a variety of new candidates for spintronics applications have become available. Consequently this sector grew into a popular field of research, where the development of GMR read heads is only one aspect. Considerable effort is put into the construction of a magnetic random access memory (MRAM), which exploits the tunnelling magnetoresistance of a ferromagnet/insulator/ferromagnet (FM/I/FM) sandwich. The idea is fairly simple as explained in Fig. 1. A commercial MRAM device with 256kByte was launched by Cypress [1] lately, yet its technological implementation is complex and offers room for improvement.

In near future we will face yet another challenge — the hard disc concept needs to be revised. Up to now the functional layer of a hard disk consists of a continuous magnetic thin film where the data is stored by the magnetisation state of adjacent domains. With this technology about 100 Gbits/in^2 can be achieved. If the domain size is further decreased coupling effects between neighbouring bits occur and may lead to loss of information. A promising path to increase the capacity beyond this limit is the use of patterned media. Potential fabrication strategies include nano-imprinting [2], interference lithography [3, 4]

1
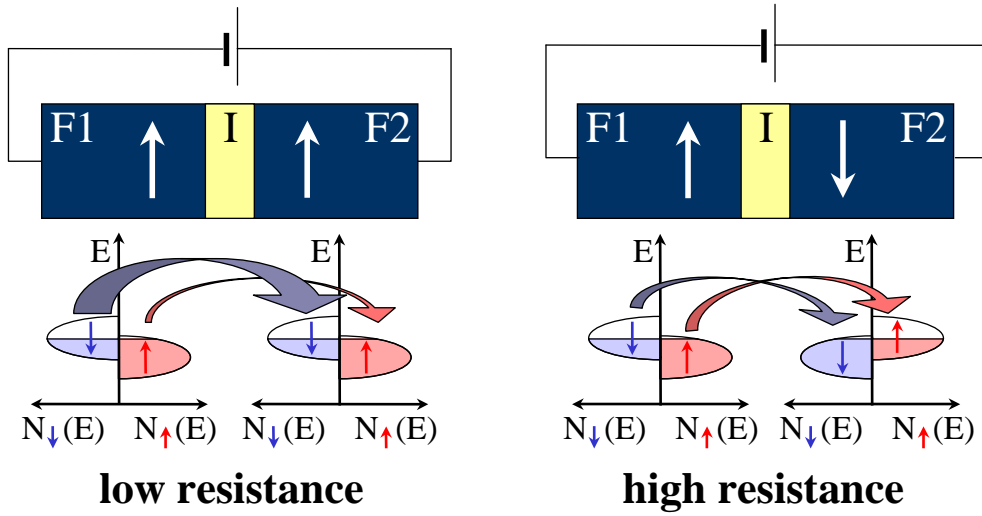
Figure 1: *The conductance of a system consisting of two ferromagnetic layers which are separated by a thin insulating barrier results from tunnelling. The current through the junction is proportional to the density of states N(E) of the participating electrodes. For a tunnelling process without spin flip the density of states product has to be evaluated separately for the two spin directions. As a result the device can adopt two distinct resistance states depending on the relative orientation of the two ferromagnetic layers. The resistance may be identified with the logic states "0" and "1".*

and self-organisation processes [5]. The requirement of a high reproducibility is also fulfilled by electron beam lithography (EBL) and focused ion beam etching (FIB). Though these techniques are particularly suitable for studying the physical properties of different shapes of nanostructures, they are not competitive in terms of throughput and cost reduction. Amongst the former concepts the bottom-up approach has a special position due to future visions of building up electronics on the molecular level.

Along with these developments the specimen characterisation has become more difficult and new methods are under investigation. To keep track of the rapid progress, the reliability of the sample evaluation process is of major importance. Therefore it has to be checked as minutious as the specimen itself. This is an important task, where the competence and responsibility of basic research is in demand.

This thesis will take up some of the above mentioned questions. In a detailed study epitaxial thin films of the double perovskite material Sr_2FeMoO_6 are investigated. As a potential candidate for half-metallicity this material has attracted much interest. Nevertheless, little is known on the intrinsic behaviour of epitaxial thin films of this compound, which is necessary to evaluate the material properties in view of a possible technological usability. In this respect also the

phase stability under variation in the preparation conditions is of interest and the influence of possible defects, specifically anti-site disorder, will be addressed. Thematically this part of the thesis is subdivided into two chapters. Chapter 1 is dedicated to the thin film preparation and the resulting structural and magnetic properties of the specimen. The technologically relevant magneto-transport behaviour is discussed in chapter 2.

The pre-selection of suitable materials for spintronics could be facilitated by a direct determination of the spin polarisation. A popular method for this task is point contact Andreev reflection (PCAR). This technique makes use of the characteristic deviations from Ohm's law in a metal-superconductor nanocontact. Junctions in the tunnelling regime, i. e. metal and superconductor are separated by an insulating barrier, may be used to image the density of states in the superconductor with the characteristical gap for energies below $\pm\Delta$. For resolving the influence of the spin polarisation, transparent junctions are required, as the Andreev reflection process takes place only there. In this case an electron approaching the superconductor with energy smaller than Δ may be converted into a Cooper pair by reflecting a hole in the opposite spin band at the junction. This process is suppressed for a spin polarised material, as the probability of the conversion depends on the density of states product $N_\uparrow(E)N_\downarrow(E)$ of the metal electrode.

While the behaviour of junctions between 3d metals and BCS superconductors is well reproduced with a simple theoretical model, the materials of main interest often require the use of correction terms to obtain a reasonable approximation of the data. On the basis of these observations the PCAR method is evaluated. In chapter 3 it is shown that the deviations from the model can be understood if the constriction, which is subject to the probe current, is affected by heating. Furthermore, with this analysis it is possible to define an upper limit for the specific resistivity of possible probe materials. For resistivities beyond this limit, the PCAR method is not a robust method and may lead to an overestimation of the spin polarisation value.

A device oriented characterisation of the probe materials has to cover the investigation of possible size effects in micro- and nano-patterned prototypes. Despite of the technological emphasis this is becoming part of academic research activities. In the highly competitive, fast moving market of microelectronics the companies are subject to a rigid time-to-market plan. In most cases this concept does not allow to carry out elaborate studies with a rather vague prognosis.

In view of this development EBL and FIB etching systems are implemented to extend the group's patterning capabilities into the nanoworld. The basic properties of these tools, especially accessible structure sizes and versatility, are ad-

dressed in chapter 4 of this thesis. As an instructive example, the fabrication of arrays of identical nano-structures by EBL is discussed. Since this kind of application includes a single patterning step, it is convenient for determining the resolution limit of the system. Moreover, the magnetisation behaviour of nanomagnets is a fascinating topic of current research activity. Not only it is interesting for next generation storage techniques, also magnetic logic has been shown to operate on the basis of coupled single domain dots [6].

The FIB system is used for pattern definition by etching. With a suitable layout a FM/I/FM trilayer thin film can be modified such, that a magnetic tunnelling junction with submicron dimensions results. Subsequent EBL and optical lithography steps are needed to add the contacts. Apart from good depth control, it is necessary to achieve proper alignment of the subsequent lithography steps. Consequently the whole process relies on a clever mask layout with adequate marker structure. The conceived mark layouts and first fabrication steps will be presented.

Chapter 1

Epitaxial Sr$_2$FeMoO$_6$ thin films: preparation and properties

Since the first report of room temperature magnetoresistance in polycrystalline Sr$_2$FeMoO$_6$ this double-perovskite material has been widely studied. Due to its high Curie temperature of 420 K and band structure calculations predicting 100 % spin polarisation [7], Sr$_2$FeMoO$_6$ is a potential candidate for spintronic devices. Yet most studies are concerned with bulk material while the preparation of good quality thin films has proven to be a non-trivial task.

Epitaxial thin films of Sr$_2$FeMoO$_6$ were prepared on SrTiO$_3$ (100) substrates by pulsed laser deposition. With the substrate choice film growth may be influenced in a well defined manner, e. g. by the introduction of strain or by modifying the grain size and crystal orientations. Therefore a series of films was deposited on a Ba$_{0.4}$Sr$_{0.6}$TiO$_3$ buffer layer and on DyScO$_3$ substrates. Both types of seed crystals offer a nearly perfect lattice match for the formation of the Sr$_2$FeMoO$_6$ thin film. The preparation is followed by a detailed analysis of the structural and magnetic properties of the samples.

1.1 Sr$_2$FeMoO$_6$ basics - consolidated findings

As a short overview this section summarises recent results that I would consider as being well-established. Yet most of it has only been researched for bulk samples. The main part of this chapter will therefore be committed to closing some of these gaps with our results obtained from thin film studies.

1.1.1 Crystal structure and magnetism

The remarkable properties of Sr_2FeMoO_6 are not a surprise in view of the large number of perovskite-like materials, which are challenging the curiosity of scientists all over the world. Therefore it is useful to start with a closer look at the crystal structure and its interrelation with other material properties.

Sr_2FeMoO_6 belongs to the group of the $A_2BB'O_6$ double-perovskites. The introduction of two cations (B, B'), usually transition metals, adds a lot of complexity to the simple perovskite cell. From a structural point of view these ions can be randomly distributed or, as frequently observed, form a sublattice with alternating layers or rock salt configuration. The latter is the case for Sr_2FeMoO_6. From an electronic point of view the variety of possible elements occupying B and B' sites introduces an additional degree of freedom, which allows to tune the electronic structure in a wide range. Band structure calculations employing the LMTO method using GGA [8, 9] or the FLAPW method in the LDA(+U) scheme [9, 10, 11] have been performed. They predict the occurrence of diverse phenomena like a transition from metallic to insulating behaviour or, in another case, the existence of ferro(i)magnetic and even spin glass systems. Neither do these results always reflect the behaviour of real systems, nor are the findings based on different approaches fully consistent, and still - a great opportunity to find and combine manifold properties within one class of materials has been unveiled.

In this context the ferro(i)magnetic, halfmetallic compound Sr_2FeMoO_6 belongs to the materials of major interest. Neutron and x-ray diffraction studies show that Sr_2FeMoO_6 adopts a tetragonal structure with $I4/m$ symmetry and lattice constants of $a = 5.570$ Å, $c = 7.899$ Å at room temperature have been reported [12]. Compared to the simple perovskite, which is described by the space group $Pm\overline{3}m$, the unit cell of this structure is doubled along the c-axis and the a/b-directions are oriented along the diagonals in the a/b-plane of the original $Pm\overline{3}m$ structure. The absolute value of the a/b base vectors is thus increased by a factor of $\sqrt{2}$. In Fig. 1.1 a model of the structure is drawn. It should be noted that this is not a representation of the Sr_2FeMoO_6 unit cell since all extensions are doubled as compared to the normal perovskite cell.

1.1.2 Saturation magnetisation and antisite disorder

For halfmetallic ferro(i)magnets the expected saturation magnetisation M_s is integer. This is a direct consequence of the half-metallic state, which is characterised by a band gap in one spin direction while the other one has metallic character. In the case of Sr_2FeMoO_6 the saturation magnetisation of the system is determined by the unpaired spins while the orbital moments are quenched. Due to an antiferromagnetic (AFM) coupling between the Fe and Mo spins, a saturation
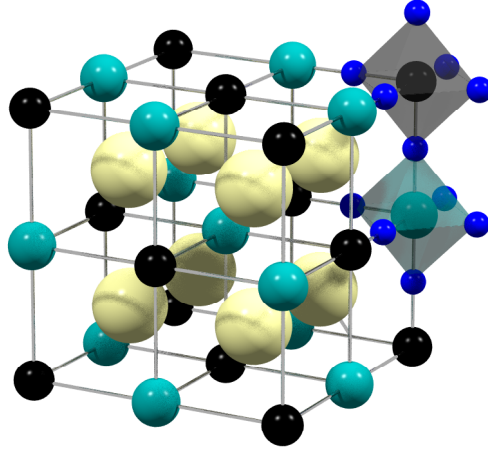
Figure 1.1: *Graphical representation of the Sr$_2$FeMoO$_6$ crystal structure. For clarity the O-atoms (blue) on the centre positions of the Fe-Mo interconnections have been omitted. Only two octahedras enclosing one Fe (green) and one Mo (black) atom, respectively, are shown. The Sr-atoms (yellow) mark the corners of a simple perovskite cell.*

magnetisation of $M_s = 4\mu_B$/f.u. is predicted.

As we will see the AFM interactions are a consequence of a pseudo double exchange mechanism. In analogy to the Zener double exchange [13] for manganese atoms interacting via an oxygen atom the following scenario has been developed. In the place of the Mn we find Fe and Mo atoms in a alternating arrangement separated by oxygen atoms. In a gedanken experiment we attribute an initial oxidation state of 3+ to the Fe and 5+ to the Mo. As confirmed by band structure calculations the remaining electrons in the Fe t$_{2g}$ and e$_g$ subbands are localised whereas the Mo t$_{2g}$ electron is itinerant, occupying the Mo (4d) and Fe(3d) orbitals hybridised with the bridging oxygen. In the double exchange picture it can therefore perform a hopping process to the oxygen which involves the transfer of a down electron from the oxygen to the Fe at the same time. As it is obvious this process only works if the electron coming from the Mo is also down spin (Fig. 1.2). So the energetically favourable state which can be understood in the pseudo double exchange picture mediates the AFM interactions of the Fe/Mo sublattice.
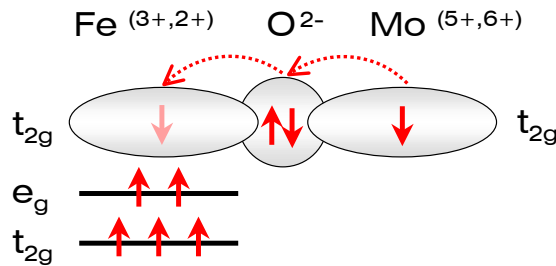
Figure 1.2: *Sketch of the pseudo double exchange mechanism which induces an AFM coupling of the Fe/Mo sublattice.*

Mössbauer spectrometry [14, 15] confirmed the existence of an intermediate valence state $Fe^{2.5+}$ and electron spin resonance measurements [16] provide evidence for the strong antiferromagnetic coupling between the localised and itinerant electrons.

Since the value of 4 μ_B/f.u. is at the very heart of the ongoing Sr_2FeMoO_6 discussion a lot of effort has been put into its experimental validation. Yet only few works were able to report a value close to the expected 4 μ_B/f.u. [17]. In the meantime it has been understood that a major problem is the preparation of samples with fully ordered Fe/Mo sublattice.

For bulk material the synthesis temperature has been identified as an important parameter by which the Fe/Mo antisite disorder can be tuned. Its effect has been investigated quantitatively by Balcells *et. al.* [18] in a series of five samples as shown in Fig. 1.3. In this study the relation between saturation magnetisation M_s and cationic order x was found to obey $M_s = (4 - 8x)$ μ_B/f.u., where x is zero for a fully ordered sample and 0.5 for absence of ordering. This result is one clue for understanding the influence of disorder on the material properties.
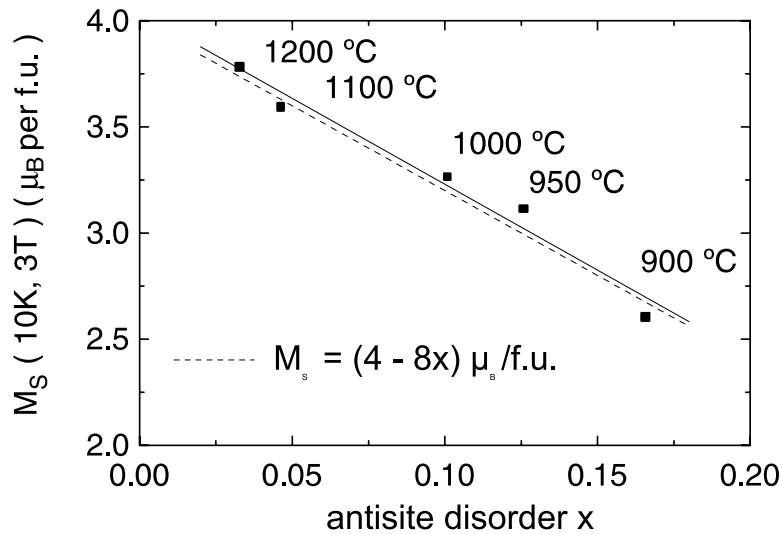
Figure 1.3: *Relation between cationic ordering and saturation magnetisation for Sr_2FeMoO_6 bulk samples prepared at various temperatures. The solid line is the linear best fit of the experimental data and the dashed line represents the expected dependence according to the discussed model. Data taken from Ref. [18].*

According to the simple picture of localised spins, the identified relation corresponds to a situation where all antisites couple antiferromagnetically with their nearest neighbours. For Fe-O-Fe sites this behaviour is expected since $SrFeO_3$ is known to be an antiferromagnet [19]. For Mo antisites the spin orientation is initially not clear, since the ternary compound $SrMoO_3$ is a paramagnetic metal [20]. Another possibility, namely the formation of small clusters of the parent

compounds SrFeO$_3$ and SrMoO$_3$ can be excluded, due to NMR experiments [21]. In this study on a series of Sr$_2$FeMoO$_6$ ceramic powders with different levels of cationic ordering it was shown that the position of the Mo line is not affected by disorder.

1.1.3 Magnetotransport and sample texture

Bearing in mind the initial motivation for studying this material, the investigation of its magnetotransport behaviour plays a crucial role. Of course antisite disorder is one parameter which strongly influences the transport properties but another aspect, namely the existence of physical grain boundaries (GB) becomes important. These two different aspects are discussed in terms of intra- and inter-grain contributions to the resistance.

Intra-grain magnetotransport behaviour

As discussed previously, metallic behaviour is expected for a perfectly ordered, single crystalline Sr$_2$FeMoO$_6$ sample. Indeed the resistance versus temperature characteristics of a weak metal has been found for bulk single crystals (Fig. 1.4).
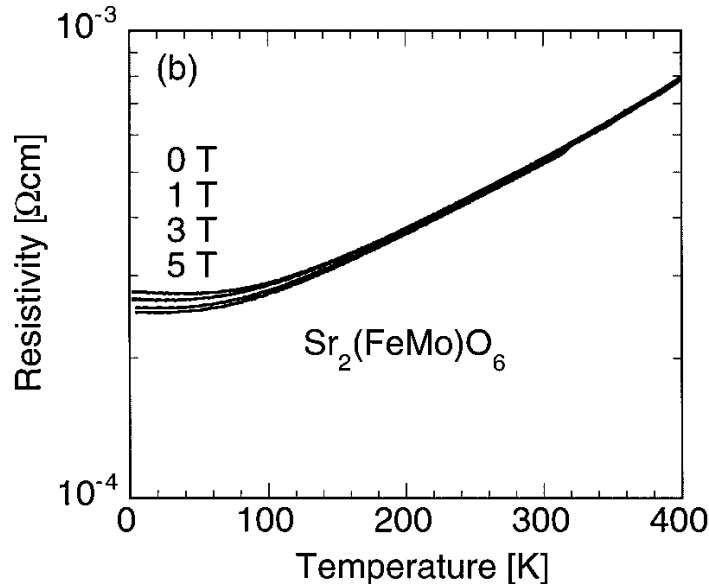
Figure 1.4: *Resistance versus temperature behaviour of a Sr$_2$FeMoO$_6$ bulk single crystal. Taken from [22].*

The Fe/Mo ordering of these samples reached 92% and a saturation magnetisation of $M_s = 3.2\mu_B$/f.u. was achieved [22, 23]. In both reports a small magnetoresistance (MR) at high magnetic fields of several Tesla was observed, where MR is defined as the optimistic ratio of the resistance change under an applied external magnetic field:

$$MR[\%] = 100 \cdot \frac{R(H) - R(H = 0)}{R(H)}, \qquad (1.1)$$

where $R(H)$ is the resistance value for an external magnetic field H. It is argued that the small negative MR arises from scattering of the charge carriers at the magnetic antisite defects. This assumption is confirmed by measurements of the anomalous Hall effect which have been explained by a classical skew-scattering mechanism [23]. Alternatively the interaction between charge carriers and magnetic defects can be understood in the hopping transport picture by sampling of a Berry phase [24, 25].

Though antisite disorder contributes to the magnetoresistance as elucidated above, substantial Fe/Mo disorder levels always lead to a reduction of MR. These findings are supported by ab-initio band structure calculations [26]. Saha *et. al.* used the LMTO-ASA formalism to model super-cells with different disorder configurations. Their result suggests the destruction of the half-metallic state due to the antisites.

Further studies were concerned with the effects of doping. By partially substituting La for Sr, Navarro *et. al.* [27] succeeded in raising the Curie temperature as a result of electron doping. Yet with this modification the amount of antisite disorder in the samples increased substantially. In turn the magnetoresistance ratio is suppressed which outweighed the positive effect of a higher T_C.

Spin polarised inter-grain tunnelling

When polycrystalline samples are investigated, a simple assumption is, that the material consists of a large number of randomly oriented grains which are separated by insulating barriers between them. The contribution of these grain boundaries manifests in a distinct resistance rise, since the electronic transport has to take place through tunnelling. It is assumed that the grain structure coincides with the magnetic domains as the formation of a domain wall is energetically favoured in the GB regions. Therefore the tunnelling probability between two adjacent grains depends on the transport spin polarisation of the charge carriers P_T and the relative orientation of the magnetic moments M_s in the material.

Due to the averaging over different grain boundary and magnetisation angles it is handier to use a single artificial GB for investigating its contribution to the total resistance. Detailed studies were carried out for manganite thin films prepared on bicrystal substrates [28, 29, 30, 31] with the objective to clarify the microscopic nature of this effect. When recording the resistance R under an applied magnetic field a strong suppression of R in the low field region $\mu_0 H < 1$ T, i.e. low field magnetoresistance (LFMR), is observed. In contrast to this, bicrystal Sr_2FeMoO_6

thin films did not display a significant LFMR [32]. It is speculated that in this material a spin dependence of charge transport across the GB is absent due to a domain pattern which remains unaffected by the induced structural disturbance.

Even though the influence of a single artificial GB could not be demonstrated undoubtedly, the LFMR shows up in measurements of polycrystalline Sr_2FeMoO_6 samples. In analogy to the results obtained for manganites, this feature is mostly attributed to spin polarised tunnelling [7, 33, 34]. By slow oxidation of single phase Sr_2FeMoO_6 ceramic samples Niebieskikwiat *et. al.* [34] induced the formation of a small amount of a $SrMoO_4$ impurity phase. This insulating oxide seems to appear at the grain boundaries enhancing the barrier while the bulk is not changed. In these samples an enhancement of the LFMR was found. Furthermore a nonlinear *I-V* characteristics was observed, which is a strong indication of tunnelling transport.

In general the intra- and inter-grain contributions to the resistance are both important. As their relative weight depends strongly on the structural details of the samples, it is difficult to determine from the complex transport behaviour. However, a series of well characterised samples with systematic variation of the structural properties can be prepared in thin film geometry, as presented in the following chapter. These type of samples are most suitable for investigating the complex nature of charge transport in Sr_2FeMoO_6.

1.2 Preparation and structural characterisation

For several compounds of the perovskite family thin film preparation has proven to work best with the pulsed laser deposition (PLD) method. Our choice to grow epitaxial Sr_2FeMoO_6 thin films by PLD was based on these findings and has been confirmed by numerous reports on thin film preparation of this compound [35, 36, 37, 38, 39, 40].

1.2.1 Pulsed laser deposition of Sr_2FeMoO_6 films

Pulsed laser deposition, like sputtering, utilises a stoichiometric target of the desired composition. The material is ablated from the target surface by 20 ns short laser pulses. In order to break up the chemical bonds of the material, energy densities of about 2 J/cm^2 are needed. To reach such high values, the spot of a KrF excimer laser ($\lambda = 248$ nm) is focussed onto an area of about 2 mm^2. We used a COMPex 301 with a maximum pulse energy of 1 J/pulse operating at repetition rates from 1 to 10 Hz. The ablated target material forms a plasma plume and expands into a small solid angle perpendicular to the target surface. At a distance of a few centimetres the propagating ions and atoms hit a

substrate where they can adsorb and - with the right choice of parameters - form an epitaxial layer. In our case the target-substrate distance was fixed at 35 mm. To allow for some reorganisation of the ions the substrate surface is heated. The interplay between energy density, target-substrate distance and choice of ablation atmosphere leads to a comparably small area of 5 x 10 mm^2 where homogeneous films are achieved. Therefore exclusively 5 x 5 mm^2 substrates are used.

Epitaxial thin film preparation yet requires the accurate control of several preparation parameters. Apart from those already mentioned, the ambient conditions at different stages of the deposition process are of main importance. The setup is located in a HV chamber with a base pressure of about $4 \cdot 10^{-7}$ mbar. When heating up the substrate the pressure can be kept in the low 10^{-6} mbar range. After stabilising the substrate temperature T_S ($800 - 895°$C) an Ar flow giving rise to a total pressure of $p_D = 0.1$ mbar is set. For most of our films an annealing step is performed after the deposition process. When the desired amount of material has been deposited the substrate temperature is increased to $T_A = 880°$C, at the same time the turbo pump is started. As soon as the turbo pump works in normal mode the Ar flow is stopped. At a low oxygen partial pressure in the range of $1 - 2 \cdot 10^{-5}$ mbar, which is adjusted by a needle valve, the annealing is carried out. When cooling down the oxygen inlet is closed. After 2 hours a temperature below $100°$C at a pressure below 10^{-6} mbar is reached. The sample is removed from the chamber after floating with Ar. In case of floating with air the base pressure deteriorates due to the adhesion of water on the inner chamber walls. A photograph of the employed system is shown in Fig. 1.5.
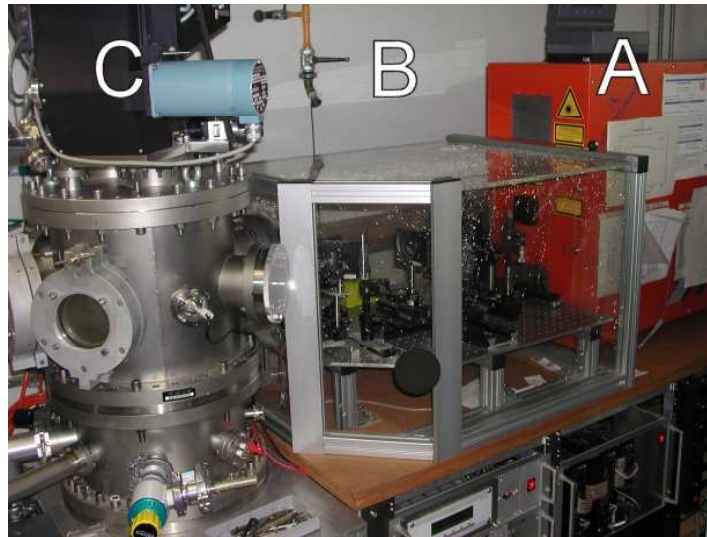
Figure 1.5: *Pulsed laser deposition setup with the main components: (A) KrF eximer laser (B) optical path (C) HV chamber.*

Care is also taken concerning the homogeneity of the material ablation. The

laser hits the target disc while it is rotating. In addition the laser spot is scanned horizontally utilizing a moving mirror in the optical path. This way most of the target surface is homogeneously removed and thus the amount of material stemming from edges can be minimized. To ensure the reproducibility of T_S and T_A the substrate is attached with silver glue to a stainless steel holder and screwed in the heating unit. It has to be noted that the absolute temperature values may still be subject to systematic deviations. The thermowire used to determine the substrate temperature is situated in a bore inside the holder about 5mm from the substrate surface. Furthermore the initial calibration remained unchanged throughout the timeframe of this work. A schematic drawing of the HV chamber summarises the main principle of this technique in Fig. 1.6.
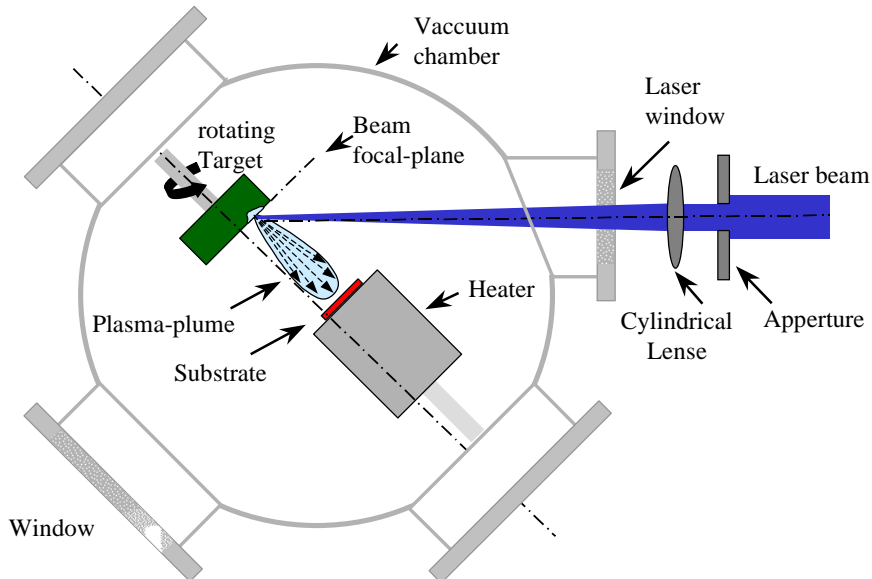
Figure 1.6: *Schematic drawing of the HV chamber in top view. The illustrated situation shows the expanding plasma plume shortly after a laser shot has hit the target surface.*

The target used for the deposition of Sr_2FeMoO_6 samples was prepared by standard solid state reaction. Stoichiometric amounts of Fe_2O_3, MoO_3 and $SrCO_3$ are mixed into a red powder which turns dark green after calcinating for one day at 950°C. The obtained material is carefully re-ground and pressed into a pellet of 25mm diameter with a force of 130 kN. The final sintering step yields a black ceramic disc which is used as the target. In Fig. 1.7 the two sintering procedures and their parameters are summarised.

2-circle x-ray diffraction of the target material reveals that it is not single phase. Besides the sought Sr_2FeMoO_6 a large $SrMoO_4$ phase is detected. This is not surprising since $SrMoO_4$ favourably forms when sufficient oxygen is present. For the pulsed laser deposition this is not a drawback as long as the grain sizes

950 (1300) °C

1(3) day(s)

20°C   1°C/min   30°C/min   20°C
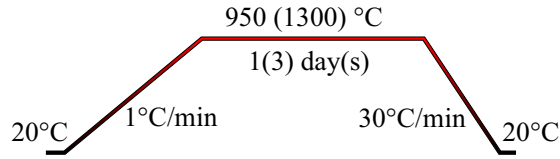
Figure 1.7:   *Target preparation routine. Values in brackets are for the sintering step. Otherwise the same parameter has been used for both heat treatments.*

compared to the laser spot size are small. In this case the ablated material will overall have a stoichiometric composition.

Several protocols have been followed in the thin film preparation resulting in quite different sets of samples. In the following sections the properties of 3 series of films, referred to as series A,B and C will be studied exhaustively. All those samples have been prepared on SrTiO$_3$ (001)-oriented substrates. A few films where a Ba$_{0.4}$Sr$_{0.6}$TiO$_3$ buffer layer or DyScO$_3$ substrates have been employed will also be discussed in detail.

1.2.2   Samples on SrTiO$_3$ (001)-oriented substrates

The choice of a standard substrate for growing epitaxial Sr$_2$FeMoO$_6$ films clearly falls on the perovskite SrTiO$_3$ for a couple of reasons. Firstly the lattice constant of 3.905 Å deviates only about 1% from the Sr$_2$FeMoO$_6$ value ($a/\sqrt{2} =$ 3.944 Å [22]). As an ideal perovskite its crystal structure is descibed by the cubic $Pm\bar{3}m$ space group. Concerning measuring the magnetic properties and magneto-transport behaviour of the thin film sample the diamagnetic and insulating nature of SrTiO$_3$ is essential. Furthermore it is well known and has been widely studied due to its frequent use as a substrate material for high T_C superconductors.

In this context it was found that under certain treatment the SrTiO$_3$ (001) surface can recrystallize and form an atomically smooth, stepped surface [41]. We applied this method to ensure identical starting conditions for all films. The treatment routine as described below was mainly adopted from reference [42]. By ultrasonically soaking in H$_2$O for 10 min, the SrO terminated surface parts will react to form a Sr(OH)$_2$ layer while the TiO$_2$ remains unchanged. An etching step in a buffered HF solution (88 ml 10 M NH$_4$F, 13 ml 40% HF) is performed to remove the Sr-hydroxide. Recrystallisation takes place when the substrate is annealed at 950°C for 1 h in an oxygen flow of 20 cm^2/min. The resulting surface morphology with atomically flat terraces of one unit cell height difference between adjacent steps is visible in the AFM micrograph in Fig. 1.8.

Sample series A, B and C were prepared by employing different modifications of the general preparation routine which has been described in the previous sec-
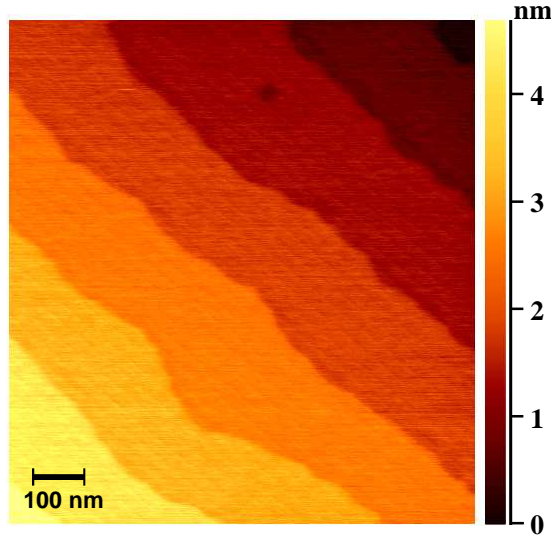
Figure 1.8:   *AFM micrograph of an atomically flat SrTiO₃ surface after pre-treatment with BHF and annealing. The height step between two adjacent terraces corresponds to a single SrTiO₃ unit cell of 3.905 Å.*

tion. Series A samples were grown with a mixture of Ar and O_2 whereas no annealing step was performed. Deviating from the usual routine some samples were cooled down in the ablation atmosphere. To identify the optimum parameter settings, T_S, p_D and the laser fluence were varied. Yet films of series A cover a wide range of sample qualities independent of the systematic parameter changes. We attribute this to the poor control over the O_2 partial pressure during deposition. Although it was limited to be less than 0.5% of p_D, the fine tuning of this parameter proved to be essential to assure the reproducibility of the films. Accompanied by the deterioration of the material properties the nucleation of a parasitic $SrMoO_4$ phase has been clearly detected by 2-circle x-ray diffractometry in a couple of films. In the SEM micrograph those samples have a very inhomogenuous surface. The bright appearance of some regions in Fig.1.9 is attributed to charging effects of the insulating $SrMoO_4$ impurities.

As a consequence of the encountered problems the deposition atmosphere was changed to pure Ar for sample series B and C and an additional 30 min annealing step at elevated temperature was introduced. During this time the sample was exposed to a low oxygen partial pressure of $1-8\cdot10^{-5}$ mbar while the base pressure of the chamber at the annealing temperature T_A=880 °C is in the low 10^{-6} mbar range. Therefore we have gained good control over the oxidising conditions by post-deposition annealing.

For both series the substrate temperature was fixed at $T_S = 820$ °C but the energy densities and deposition rates were different. Within series B the reduction of the laser fluence from about 2.5 J/cm² to 1.7 J/cm² resulted in a strong decrease of the deposition rate ranging from 90 Å/min down to 20 Å/min. In contrast,
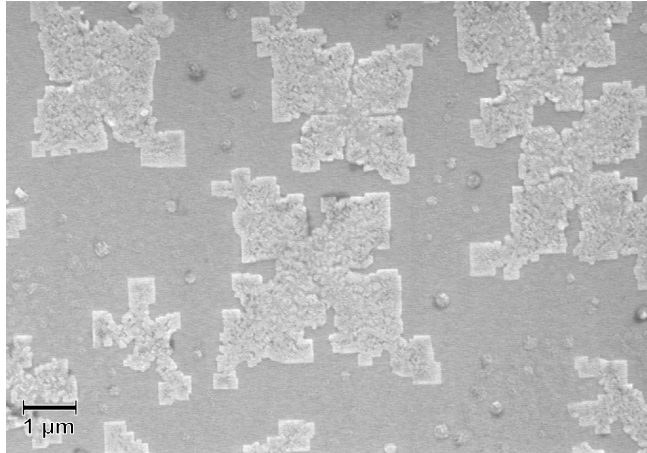
Figure 1.9:   *SEM micrograph of a Sr$_2$FeMoO$_6$ thin film with SrMoO$_4$ impurity phase.*

all samples of series C were prepared with low laser fluence of approximately 1.7 J/cm^2 and deposition rates between 15 Å/min and 20 Å/min. Any further decrease has a detrimental effect on the film properties. Presumably at this point the laser fluence falls below the minimum energy density, which is necessary in order to achieve an element independent ablation of the target material. Using the saturation magnetisation as an indicator for the film quality, Fig. 1.10 reveals that the best samples are obtained with ablation rates around 20 Å/min. In the following only these films be be discussed in detail.
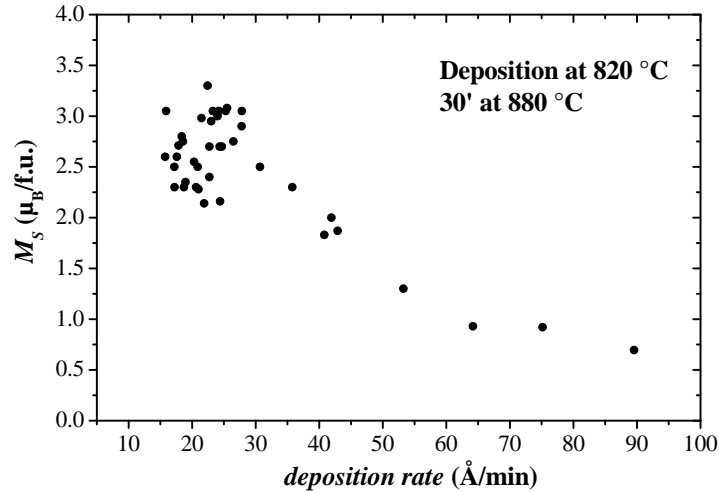
Figure 1.10:   *Influence of the deposition rate on the saturation magnetisation, which is an indicator for the film quality.*

In a recent report by Fix *et. al.* [43] the same causal relation between deposition rate and quality of the thin films has been established, though their preparation routine differs drastically. Thus it can be concluded that the film

quality is strongly dependent on the available time for diffusion processes at the free surface during film growth.

In a narrow region of deposition rates, where good films are obtained, a sudden change of the surface morphology has been observed. Sr_2FeMoO_6 films prepared at deposition rates of $20 - 25$ Å/min have a rather granular aspect with a mean roughness of about 10 nm. They are counted among sample series B. For series C prepared at $15 - 20$ Å/min the mean roughness of the film surfaces was up to ten times smaller as determined by atomic force microscopy (AFM). Typical examples of series B and C are shown in Fig. 1.11.
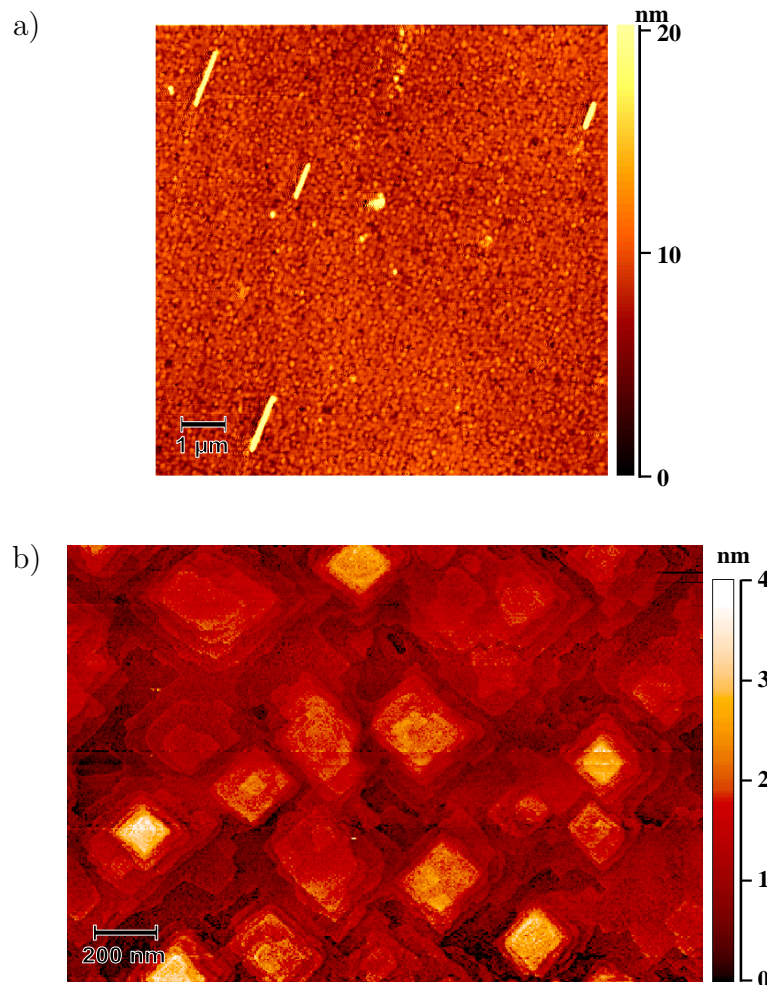
Figure 1.11: *a) AFM picture of a typical sample from series B, b) scanning tunnelling microscopy (STM) picture of a typical sample from series C.*

X-ray diffraction studies to check the c-axis epitaxy are performed for every film usually within one day after preparation. In the $2\theta - \omega$-scans $SrMoO_4$ peaks were not detected for films of B and C series but a small Fe_3O_4 impurity phase was identified in a few cases. A detailed analysis of the 2-circle x-ray data can be found in section 1.3.1.

Table 1.1: *Variation in the preparation conditions and sample classification into three series: A, B and C.*

Series	Deposition rate	Depos. temperature T_S	Depos. pressure p_D
A	30 - 60 Å/min	800 - 895°C	0.1 mbar Ar+O$_2$
B	20 - 90 Å/min	820°C	0.1 mbar Ar
C	15 - 20 Å/min	820°C	0.1 mbar Ar

Series	Annealing temperature T_A	Annealing pressure p_A
B	880°C	$\leq 8 \cdot 10^{-5}$ mbar
C	880°C	$\leq 8 \cdot 10^{-5}$ mbar

1.2.3 Samples on SrTiO$_3$ with Ba$_{0.4}$Sr$_{0.6}$TiO$_3$ buffer layer

The use of a substrate as template for epitaxial thin film growth always entails a more or less pronounced influence on the sample structure depending on their lattice mismatch. As the material properties of Sr$_2$FeMoO$_6$ are extremely sensitive to structural defects, we have employed a buffer layer to adapt the lattice parameters beyond the 1% deviation of SrTiO$_3$. Motivated by a recent report from Asano *et. al.* [44], we focussed on the preparation of a Ba$_{0.4}$Sr$_{0.6}$TiO$_3$ layer. With the specified composition the face-diagonal of the perovskite cell matches exactly the in-plane constant of Sr$_2$FeMoO$_6$ making it the ideal choice.

For depositing Ba$_{0.4}$Sr$_{0.6}$TiO$_3$ by pulsed laser ablation a stoichiometric target was fabricated similar to the preparation of the ceramic Sr$_2$FeMoO$_6$ disc. The parameters for the two sintering procedures are given in the inset of Fig. 1.12. The resulting polycrystalline powder was checked by 2-circle x-ray diffractometry (Fig. 1.12). The 2θ-ω scan has been analysed with the FULLPROF software [45] to extract the lattice constant. A value of $a = 3.9413(7)$ Å is obtained, which is about 0.1% less than expected. One cause could be a slight deviation in the Ba:Sr ratio. Oxygen off-stoichiometries are another aspect that influence the lattice constant but these dependencies cannot be resolved in the presented x-ray data. Therefore a further discussion is abandoned.

When Ba$_{0.4}$Sr$_{0.6}$TiO$_3$ is deposited under an oxygen pressure of $p_D = 0.07$ mbar at $T_D = 750$°C, it develops an atomically flat surface. Even for a 135 nm thick layer, which corresponds to roughly 2730 unit cells, the terraced surface of the SrTiO$_3$ substrate is maintained (Fig. 1.13(a)). In accordance to this, these films
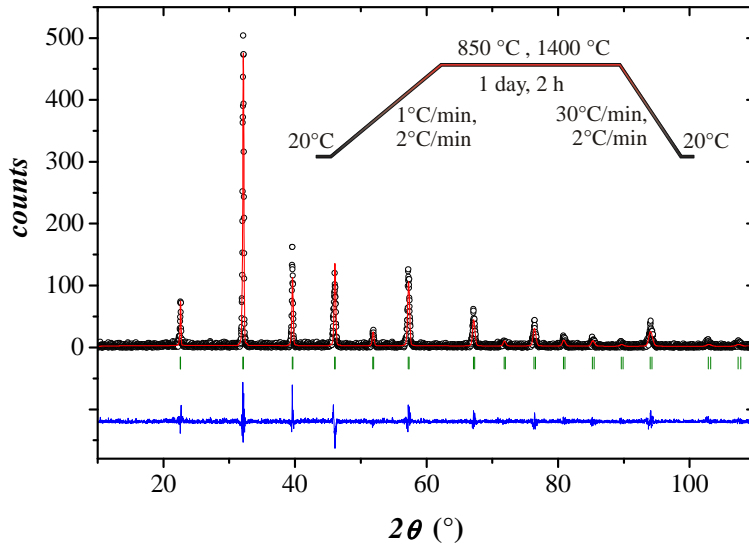
Figure 1.12:   *Preparation parameters and x-ray analysis of $Ba_{0.4}Sr_{0.6}TiO_3$ target material. The measured data (black circles) has been fitted (red line) with the FULLPROF analysis software [45]. The blue curve is the difference between the previous two datasets, while the green marks indicate the peak positions.*

are characterised by a high crystal quality. The x-ray diffractogram in Fig. 1.13(b) has been recorded from a 30 nm thick film. Due to the finite number of scattering planes higher order maxima of the film peaks occur, but they can be resolved only for narrow linewidth. In the inset of Fig. 1.13(b) these side maxima are enlarged. Since limited volumes of coherent scattering, i. e. small grain sizes, lead to a peak broadening, one has to conclude that these films are good single crystals with only few defects. Consequently the full width half maximum of the rocking curve (FWHM < 0.08°) recorded at the respective peak positions is predominantly determined by the diffractometer resolution rather than the true mosaic spread of the epitaxial layer.

Close to the interface the in-plane lattice constant of the $Ba_{0.4}Sr_{0.6}TiO_3$ layer is expected to adopt the substrate value while a relaxation from a distorted to the cubic unit cell with increasing film thickness is common. In the case of $Ba_{0.4}Sr_{0.6}TiO_3$ a tetragonal distortion persists even for thick layers presumably due to the vicinity of a ferroelectric phase transition. For a slightly different composition this effect has been calculated on the basis of a phenomenological model [46]. Apart from the remaining lattice mismatch, the use of an oxygen atmosphere in the PLD chamber prior to the deposition of the Sr_2FeMoO_6 phase constitutes a drawback for the preparation of high quality thin films.

A different growth behaviour is observed when the ablation atmosphere consists of 0.07 mbar Ar instead of O_2. The AFM micrograph Fig. 1.14(a) shows the

a)

b)
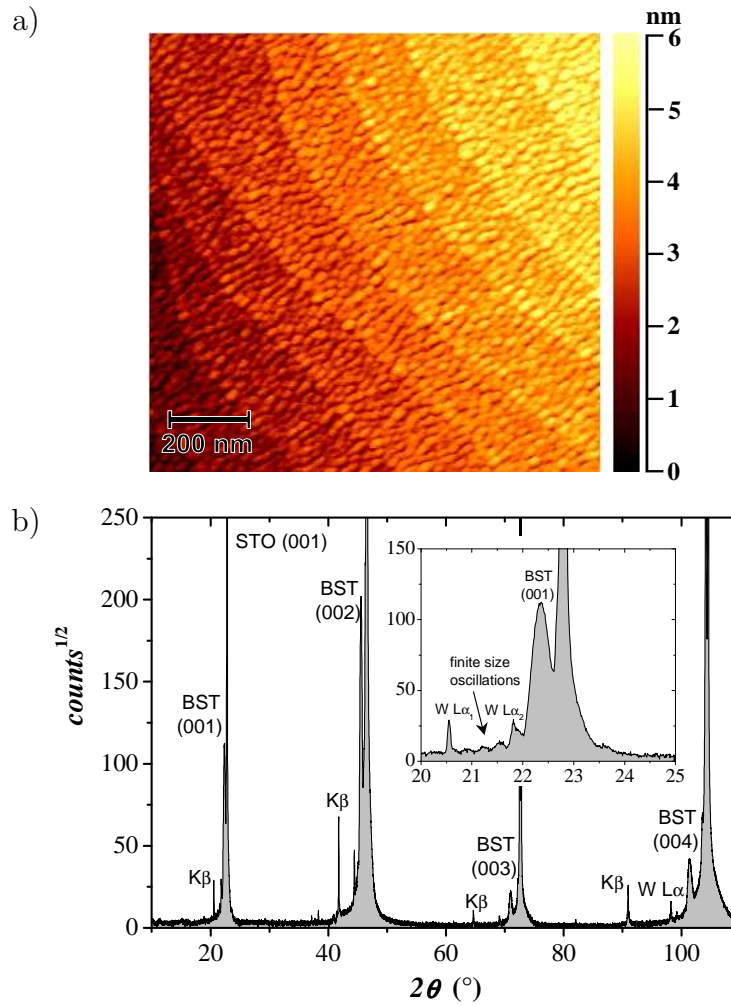
Figure 1.13:   a) AFM picture and b) 2-circle x-ray diffraction pattern of
an epitaxial $Ba_{0.4}Sr_{0.6}TiO_3$ sample. Besides the peaks originating from the
$Cu_{K_{\alpha1,\alpha2}}$ radiation, Cu_{K_β} reflections with much lower intensity occur at the
marked positions.

surface of a $Ba_{0.4}Sr_{0.6}TiO_3/Sr_2FeMoO_6$ layer sequence deposited in situ on a pre-
treated $SrTiO_3$ substrate. In this case the unit cell steps have vanished and the
mean roughness of the film has increased tremendously by more than one order of
magnitude. The 2-circle x-ray diffraction pattern (Fig. 1.14(b)) reveals that also
the film crystallinity has changed from epitaxial to textured. A small shoulder
on the left side of the (002) and (004) substrate reflection is visible where the
$Ba_{0.4}Sr_{0.6}TiO_3$ and Sr_2FeMoO_6 (00l) peaks are expected to show up. No intensity
is observed though at the peak positions belonging to any other crystal orienta-
tion. In conclusion the material still exhibits a preferential c-axis alignment, but
due to the broad distribution and low intensities the rocking curve width was not
determined.
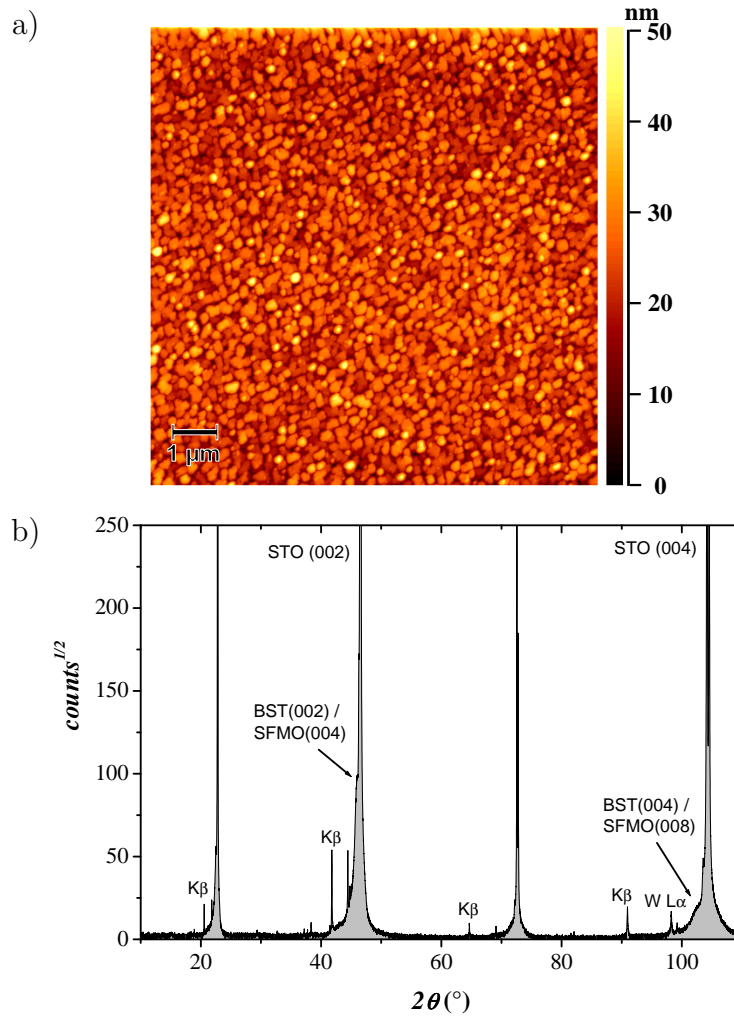
Figure 1.14:   a) AFM micrograph and b) x-ray diffractogram of a Sr_2FeMoO_6 thin film on textured $Ba_{0.4}Sr_{0.6}TiO_3$.

The Sr_2FeMoO_6 thin films were deposited using the optimised parameter settings of sample series C. The small lattice mismatch between the buffer layer and the Sr_2FeMoO_6 thin film gives reason to assume that epitaxial growth on the differently oriented $Ba_{0.4}Sr_{0.6}TiO_3$ grains is achieved. For typical film thicknesses ≥ 50 nm Sr_2FeMoO_6 forms a continuous layer incorporating a large number of grain boundaries (GB). Compared to films grown fully epitaxially on $SrTiO_3$ or $DyScO_3$ substrates where some GB's may also be present, the average angle between grain boundaries is much larger, which is changing the transport properties of the material.

These samples are not considered as being of interest for technical application. But as a link between bulk polycrystals and epitaxial thin films they provide an additional access for investigating fundamental questions like the role of GB's for the magnetoresistance. Detailed results will be presented in section 1.3 and chapter 2.

1.2.4   Samples on DyScO$_3$ (110)-oriented substrates

Another perovskite material which can serve as a substrate with very small lattice mismatch is DyScO$_3$. In contrast to previously discussed materials DyScO$_3$ possesses a strongly distorted orthorhombic unit-cell with space group *Pbnm* and lattice constants $a = 5.43$ Å, $b = 5.71$ Å, $c = 7.89$ Å [47]. But when cut parallel to the (110) plane, the surface structure is nearly cubic and a good template for Sr$_2$FeMoO$_6$ thin film growth (see Fig. 1.15).
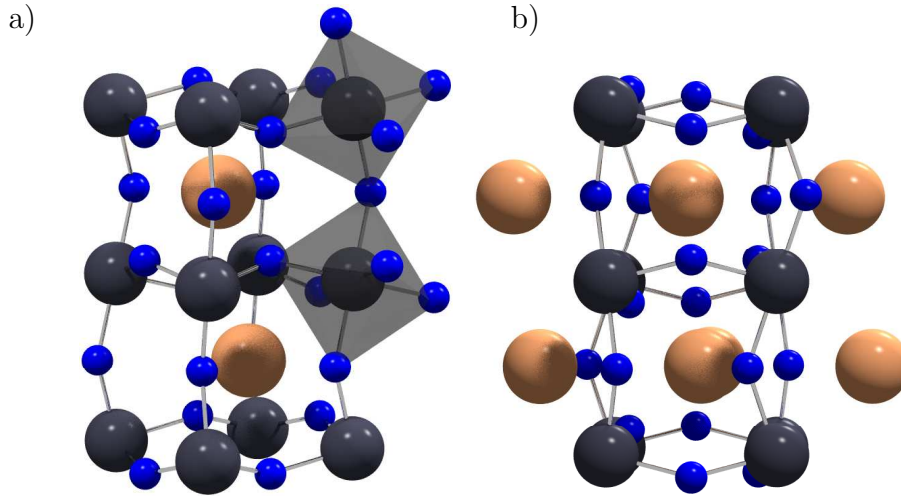
Figure 1.15:   *a) Graphical representation of the DyScO$_3$ crystal structure. b) Projection of the (110) plane with nearly cubic arrangement of the Sc-cations (dark grey): $a/\sqrt{2} + b/\sqrt{2} = 7.88$ Å $\approx c$.*

DyScO$_3$ also fulfils the pre-requisite of good electrical insulation. Amongst other perovskite materials it is being considered as a potential gate dielectrics in silicon MOSFETs [48]. Despite this and the good lattice matching DyScO$_3$ is unsuitable as a standard substrate. Its paramagnetic nature does not allow magnetic characterisation of the thin film samples by SQUID or VSM magnetometry. Yet these are the standard methods applied for monitoring the success of preparation optimisation. Therefore DyScO$_3$ substrates were used only when samples with reproducible properties could be fabricated.

Sr$_2$FeMoO$_6$ thin films were prepared with the same set of parameters employed in sample series C. Accordingly, smooth films were obtained (Fig. 1.16 (a)). The x-ray diffractogram reveals an improvement of the crystal quality compared to samples on SrTiO$_3$. Finite size oscillations (compare section 1.2.3) were observed in all samples of thickness $d \leq 80$ nm. With a full width half maximum of $0.07°$ the rocking curve width in the example of Fig. 1.16 (b) matches the value obtained for the substrate and reflects the resolution limit of the x-ray diffractometer. It

has to be considered as an upper limit for the true value. To determine the Sr_2FeMoO_6 out-of-plane lattice constant c only the position of the (008) peak could be analysed since lower order reflections are strongly overlapping with the respective substrate peaks. The following section is dedicated to the analysis of structural and magnetic sample properties and their interrelation. With a discussion of the respective lattice constants will be proceeded in this context.
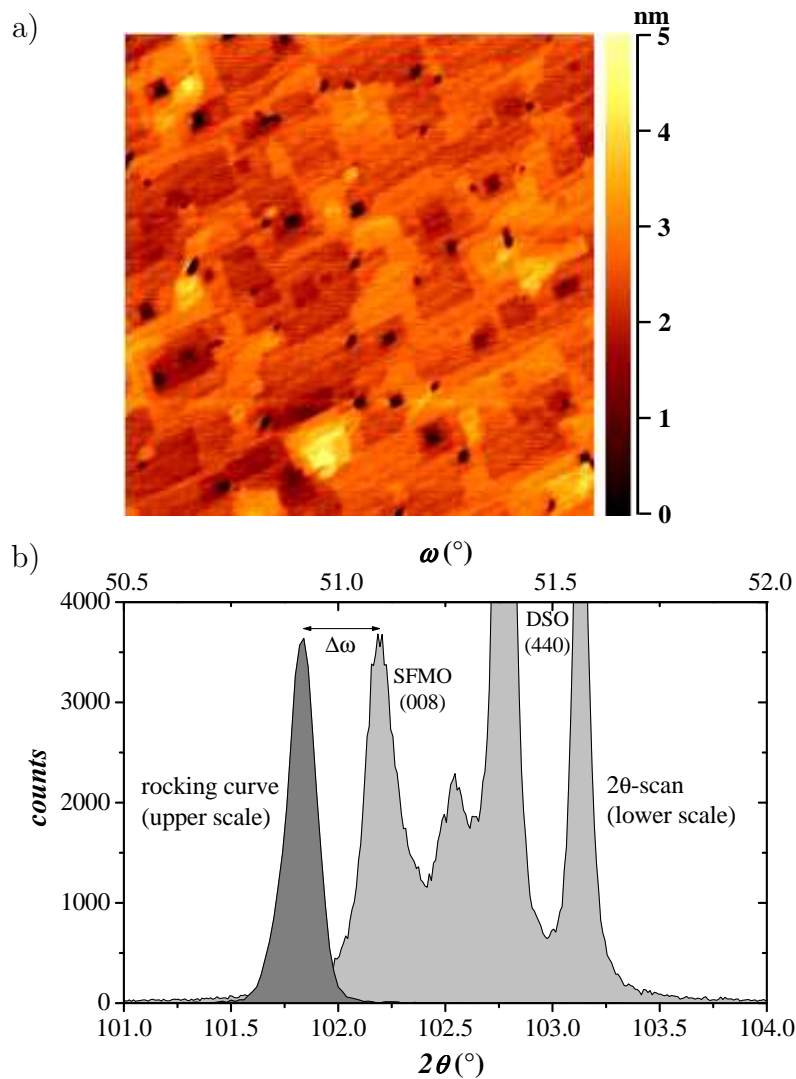
Figure 1.16:   a) AFM picture and b) 2-circle x-ray diffraction pattern of an epitaxial Sr_2FeMoO_6 thin film on $DyScO_3$. The difference between the maximum of the rocking curve and the respective peak position in the 2θ-scan ($\Delta\omega$) arises due to the substrate miscut angle and a possible misalignment of the sample surface with respect to the diffractometer geometry.

1.3   Interplay of structure and magnetism

The structural and magnetic properties of the thin film samples have been carefully studied. First of all they are decisive for a successful optimisation of the preparation process. Moreover, it is possible to promote the microscopic understanding of magnetism in this material, due to the close interrelation between structure and magnetism.

Complementary to the 2-circles x-ray diffractometer, which has the advantage of a high angular resolution, a 4-circle x-ray diffractometer has been used. It provides access to the in-plane lattice constants and texture. Furthermore the relative intensity of the Sr$_2$FeMoO$_6$ (101) reflection can be studied, which is characteristical for the ordered double-perovskite phase associated with a regular Fe/Mo arrangement.

Magnetisation measurements were performed in a vibrating sample magnetometer (VSM) and superconducting quantum interference device (SQUID). While the saturation magnetisation of every sample was checked in the VSM at $T = 4$ K, the SQUID was used to record the remanent magnetisation below and above the Curie temperature. From this data the value of T_C is extracted.

1.3.1   Strain and ASD by x-ray diffractometry

X-ray diffractometry in Bragg-Brentano geometry was used to characterise the structural properties of all prepared samples. The two-circle and four-circle setups including their standard notation, which is adopted throughout the text, are sketched in Figs 1.17 and 1.18.
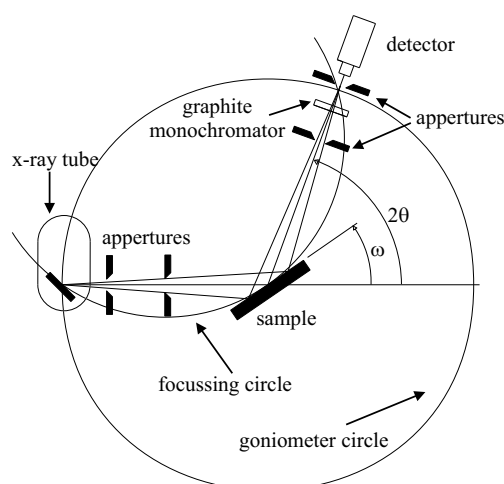
Figure 1.17:   *Sketch of the 2-circle x-ray diffractometer in Bragg-Brentano geometry.*
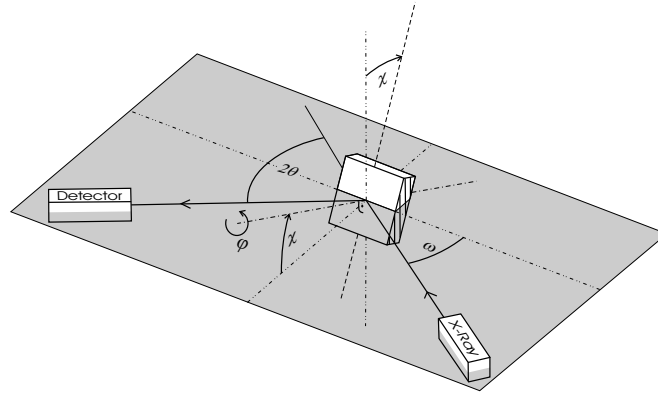
Figure 1.18: *Plane of x-ray source, sample and detector in a four-circle diffractometer in Bragg-Brentano geometry.*

During the optimisation process the structural analysis was mostly limited to the two-circle x-ray diffractometer. Therefore the c-axis lattice parameter, which coincides with the growth direction, was systematically monitored while the in-plane lattice constants were checked subsequently for a random selection of samples. Judging from the available four-circles x-ray data, the volume of the Sr_2FeMoO_6 unit cell is almost constant for all our films. Accordingly, the c-axis length provides all necessary information to study strain and its relaxation. In Fig. 1.19 the evolution of c for high quality samples of series B and C is illustrated by means of the Sr_2FeMoO_6 (004) peak displacement.
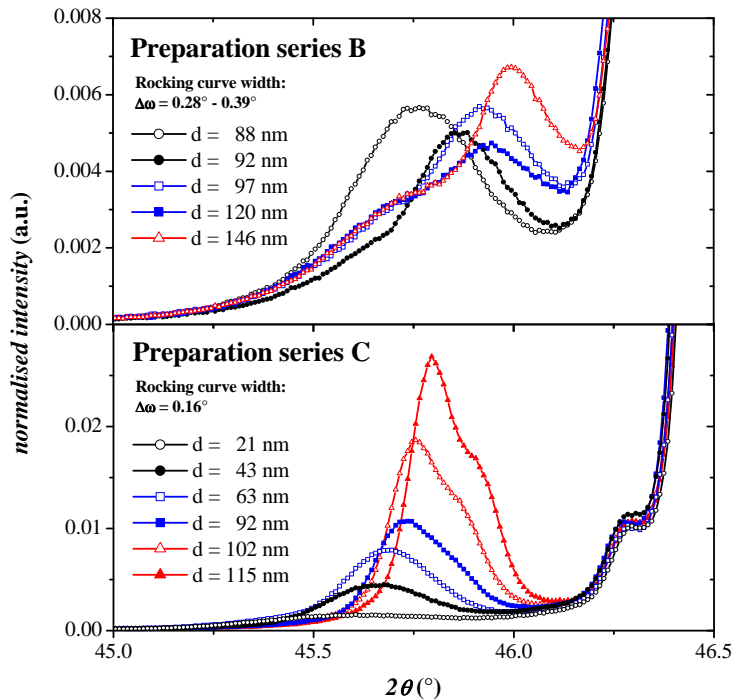
Figure 1.19: *2-circle x-ray diffractograms of the Sr_2FeMoO_6 (004) reflection for various samples of preparation series B and C.*

For both series changing the sample thickness has a marked effect on c, which decreases (2θ increases) for thicker samples. While the rocking curve width in series C is very small with an upper limit of 0.16°, a distribution of $\Delta\omega$ ranging from 0.28° to 0.39° was measured in series B. Consequently, the peak height in the $2\theta - \omega$-scan of these samples does not scale with the film thickness. Furthermore, the smearing of the (004) peak signalises a large distribution in the c-axis length which is absent for samples of series C.

In a direct comparison of the evolution of c as function of the samples thickness, see Fig. 1.20, it is evident that strain relaxation is more effective in sample series B. This is in accordance with the morphology and crystal spread, since these films incorporate a larger number of crystalline defects.
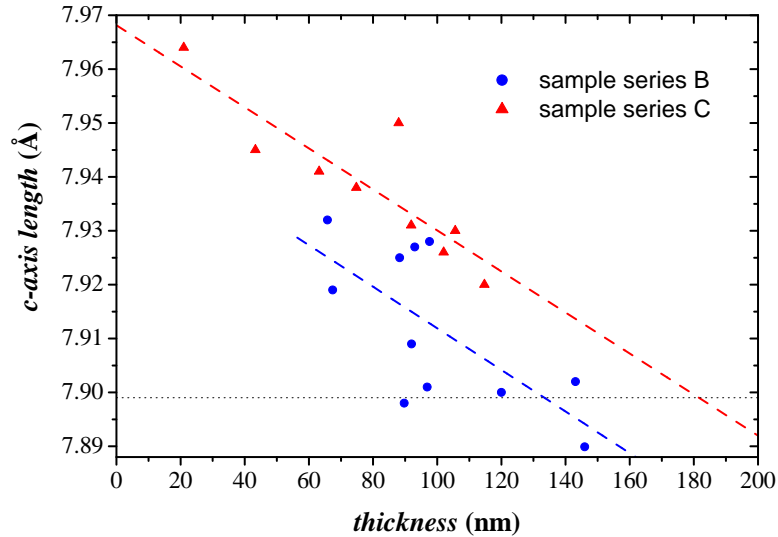
Figure 1.20: *Evolution of the c-axis for sample series B and C as function of the sample thickness. The dotted line marks the bulk lattice constant.*

The main aspect which has been studied in the 4-circle x-ray diffractometer is the variation in the (101) superstructure peak intensity. To have a common standard the (101) reflection has been measured and normalised to the intensity of the Sr$_2$FeMoO$_6$ (004) peak. Both peaks were recorded in a rocking curve scan, i. e. ω is scanned while 2θ remains fixed at the centre position of the peak, which was previously determined by an automatic centring routine. The integrated peak intensities were obtained by fitting Gaussian peak shape functions. A simple numerical integration of the peak intensities does not produce reliable results due to the vicinity of the SrTiO$_3$ (002) and Sr$_2$FeMoO$_6$ (004) reflections. By using a double peak fit function the two contributions in the (004)-scan can be separated. An example illustrating this routine is presented in Fig. 1.21.
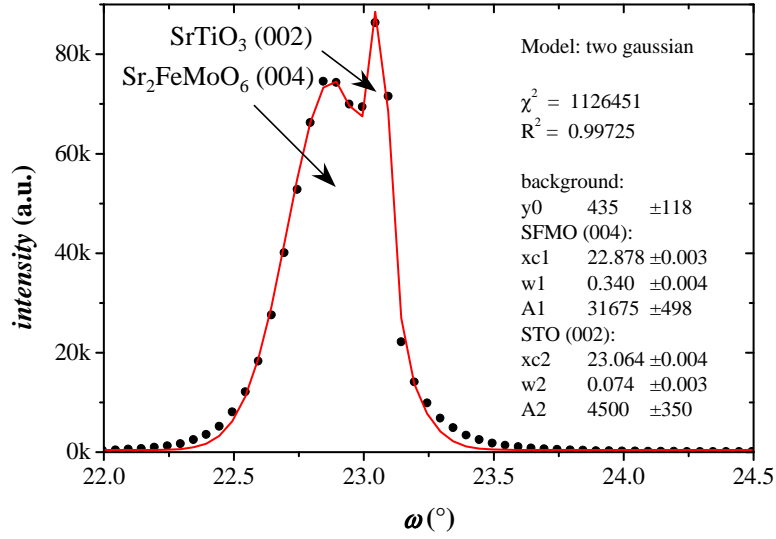
Figure 1.21: *To determine the contribution of the Sr_2FeMoO_6 (004) and $SrTiO_3$ (002) reflections, two Gaussian distributions have been fitted. The respective parameters are stated in the graph.*

The importance of a detailed structural analysis lies in the close connection between strain, Fe/Mo ordering and the achievable saturation magnetisation-Therefore the magnetisation data is presented in the next section and a detailed discussion follows after that.

1.3.2 Magnetisation measurements and data treatment

Magnetisation measurements were performed in commercially available systems, i. e. a SQUID magnetometer by Quantum Design and a VSM by Oxford Instruments. The accessible temperature range is 4 K to 400 K and 4 K to 350 K respectively. The SQUID can be alternatively equipped with a high temperature inset, offering the possibility to measure in the temperature range from 300 K to 700 K. Since the Curie temperature of our thin film samples is slightly depressed compared to bulk material, the use of the high temperature inset was not necessary. Due to the instability of Sr_2FeMoO_6 when exposed to oxygen at high temperatures [32], measurements above 400 K should only be performed in vacuum or a clean inert gas atmosphere. In the SQUID the temperature control is achieved by a continuous helium flow which is heated but the purity of the sample environment cannot be controlled precisely. Therefore the measurement range was kept within the limit of $T < 400$ K.

Hysteresis loops were recorded in the VSM at fixed temperatures of 4 K and 300 K while the magnetic field was varied from $\mu_0 H = -5$ T to 5 T. The measurements were performed with the field direction parallel to the film surface, so that the demagnetisation factor is negligible. For all Sr_2FeMoO_6 samples small

coercive fields ranging from 20 mT to 60 mT were found. Nevertheless a field of about 1.5 T is necessary to reach the full saturation magnetisation.

The measurement points taken in the high field range from 2 T to 5 T primarily serve to distinguish between three different contributions to the raw data. The ferromagnetic signal from the Sr$_2$FeMoO$_6$ layer is superimposed by the diamagnetic response of the SrTiO$_3$ substrate. As the volume fraction of the substrate is very large these two contributions can have the same order of magnitude for high fields. By linearly fitting the high field regions the diamagnetic background can be eliminated. A further complication is the hysteretic, non-monotonic yet reproducible background signal stemming from the VSM electronics itself. It was eliminated by subtracting a reference measurement of the empty sample holder from the recorded data. In Figure 1.22 the process of data refinement is illustrated using a typical dataset.
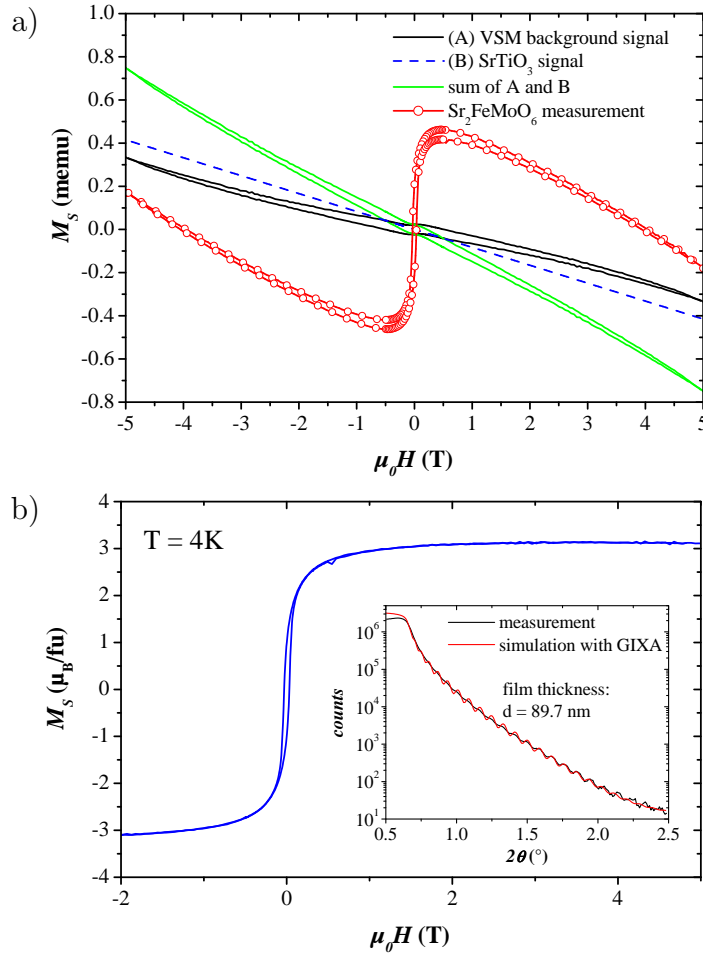
Figure 1.22:   a) *The as measured magnetisation data is corrected by subtracting an empty measurement signal (A) and a linear background (B) stemming from the substrate. b) To obtain the final curve the magnetisation is converted from emu to μ_B/fu. The critical parameter for this step is the film thickness, which can be determined by small angle x-ray diffractometry (see inset).*

This procedure adds some additional noise to the results, but the statistical error is comparatively small. The main uncertainties result from the inaccuracy of measuring the film thickness, which enters into the calculation when M_s is expressed in units of μ_B/fu. Depending on the sample morphology the thickness determination by small angle x-ray diffraction is afflicted with an error of about 5% to 10%.

Due to the relatively high background signal at low fields an analysis of the remanent magnetisation M_{rem} on the basis of VSM measurements was abandoned. For this purpose the SQUID magnetometer proved to be the appropriate tool. While M_{rem} was measured for all samples at a field of 2 mT in the temperature range of 4 K to 400 K, full hysteresis loops were recorded only sporadically as a cross-check. Typical magnetisation curves for the different types of samples are shown in Fig. 1.23.
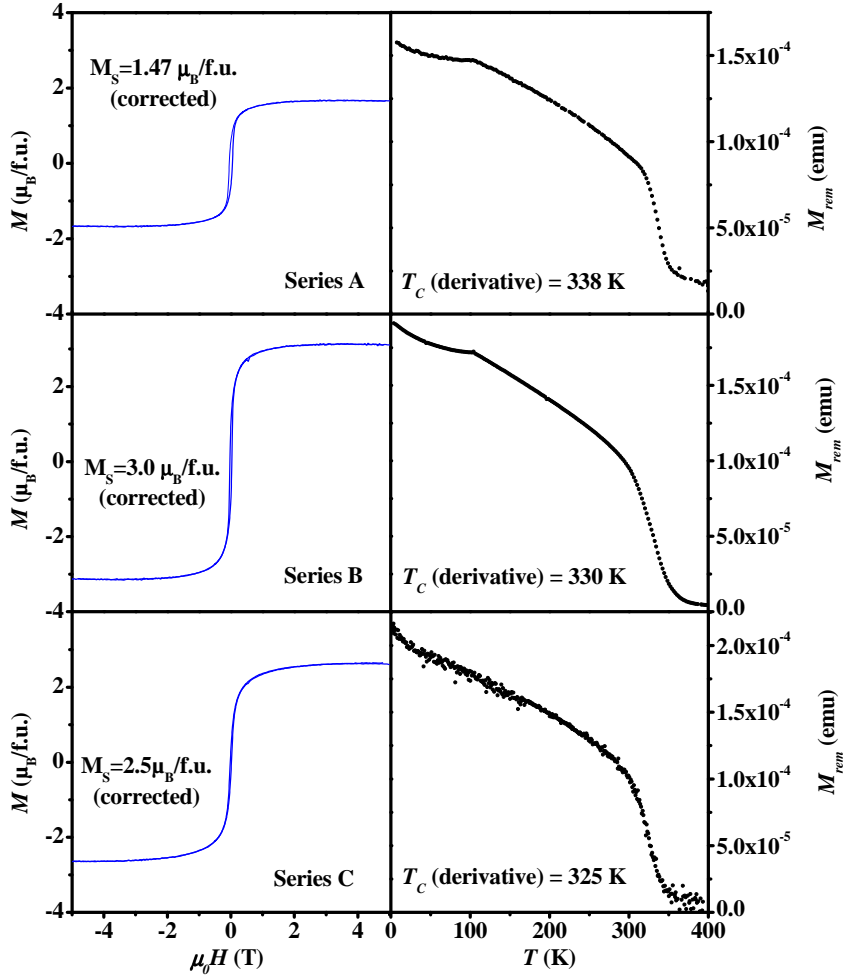
Figure 1.23:   *Typical magnetisation curves for sample series A, B and C. The magnetisation curves (left) have been corrected by subtracting the SrTiO$_3$ contribution and VSM background signal.*

The magnetic ordering temperature was extracted from the M_{rem} versus T plot by finding the minimum of the numerical derivative. Thus the T_C value is nearly independent of the transition width. One should keep in mind that compared to the frequently used definition of T_C as the onset temperature of magnetic ordering, the applied method will always yield lower values.

For B and C samples, which were grown under optimised conditions, M_{rem} approaches zero for temperatures well above T_C. In contrast, samples prepared with different process parameters often show a non-vanishing signal of the remanent magnetisation at 400 K. This behaviour is attributed to the existence of ferromagnetic impurities with higher T_C, such as magnetite. If these contributions are ignored, the saturation magnetisation M_s of the Sr$_2$FeMoO$_6$-phase is overestimated. Therefore we reduced M_s by the percentage of remanent magnetisation above T_C. A striking feature of the temperature dependent remanent magnetisation is the kink at around 100 K. It may arise due to the structural phase transition of the SrTiO$_3$ substrate [49] or stem from the antiferromagnetic phase transition of some SrFeO$_3$ impurities [19].

1.3.3 Antisite disorder limited saturation magnetisation and the role of strain

Based on the analysis of the (101) superstructure peak the relation between saturation magnetisation and antisite disorder can be studied. The possibility to introduce a lattice distortion of variable strength, which is quantified by the elongation of the c-axis is unique to the thin film geometry. Details will be discussed in the following.

Recalling from section 1.1.2, the antisite disorder parameter x is defined as the fraction of Mo atoms occupying Fe positions and vice versa. Thus the normalised superstructure peak intensity $I_{(101)/(004)}$ is a direct measure of the quantity x. But the calculated peak intensities, which are determined by the atomic positions and scattering coefficients of the different elements in the unit cell, are only valid for powder studies. For epitaxial thin films additional geometric corrections need to be introduced since the scattering is no longer isotropic with respect to the plane of incidence. In order to calculate the correction factors, one has to be sure that either the whole sample/detector is illuminated or the full intensity hits the sample/detector at all times. Since it is not sure whether this requirement is met, it was not proceeded with calculating the theoretically expected value. Alternatively, the measured data (see Fig. 1.24(a)) was extrapolated to the ideal case with a nominal saturation magnetisation of 4 μ_B/f.u. With this procedure $I_{(101)/(004)}$ can be matched to the antisite disorder parameter x.
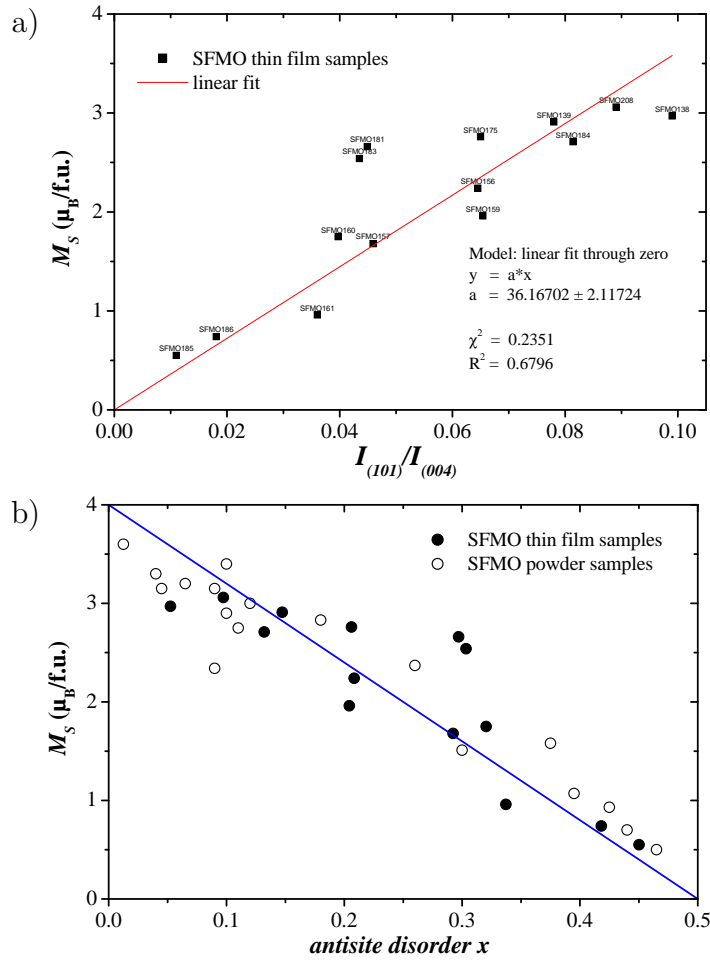
Figure 1.24: *Saturation magnetisation versus antisite disorder. (a) With decreasing intensity of the (101) reflection the saturation magnetisation is suppressed. (b) The evolution of the saturation magnetisation is well described by $M_s = (4 - 8x)\mu_B/\text{f.u.}$ The data points in the plot referring to powder samples are courtesy of D. Sánchez and M. García-Hernández [50].*

When M_s is plotted as function of x the present data can be compared to previous powder studies. Figure 1.24 (b) demonstrates that both types of samples obey the relation $M_s = (4 - 8x)\mu_B/\text{f.u.}$ in accordance with Ref. [18]. From this result it is concluded that disorder, like in bulk samples, is the prominent mechanism of magnetisation decay.

This raises the question of how the formation of disorder is promoted. One can assume that the morphology and structure of the films does have a direct influence. A well controlled parameter of structural variation is the elongation of the c-axis. A plot of the evolution of the antisite disorder x with respect to the c-axis length is shown in Fig. 1.25 a). As c approaches the bulk value of 7.899 Å, the antisite disorder tends to decrease. Consequently, the saturation magnetisation varies as function of the lattice distortion, which is presented in Fig. 1.25 b).
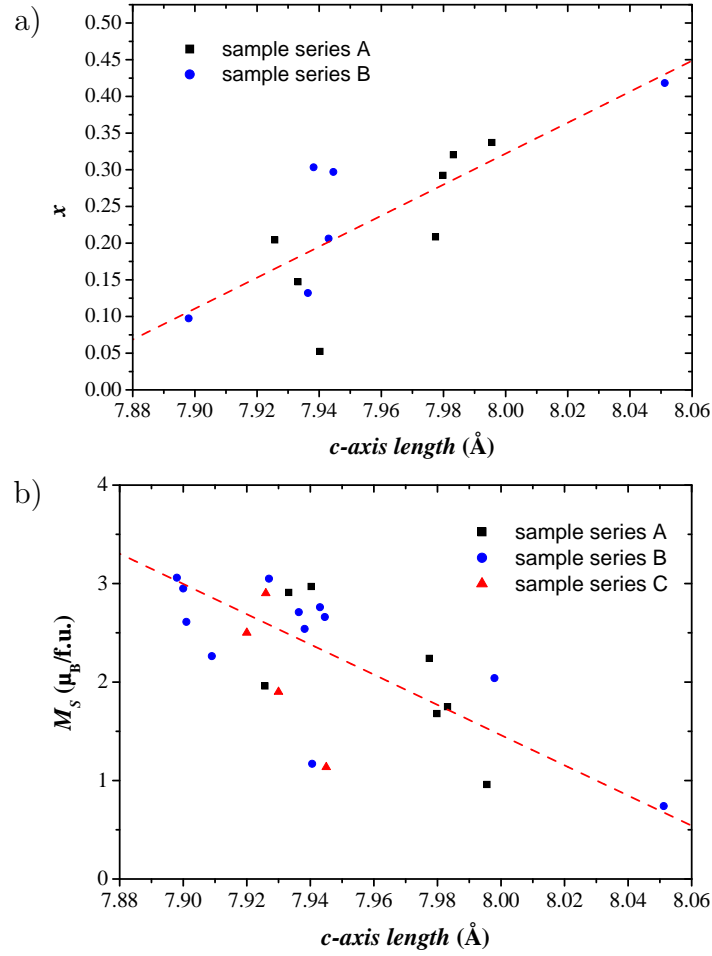
Figure 1.25: *Influence of strain on (a) the antisite disorder and (b) the saturation magnetisation.*

The observed behaviour strongly suggests that the ordered phase is incompatible with lattice deformations. However, full strain relaxation is not a guarantee for a perfectly ordered sample, as judged by the extrapolation and the large spread in the data of Fig. 1.25 a). These deviations are associated with the influence of point defects, impurity phases or an inhomogeneous distribution of strain, which are hardly accessible to a systematic study.

Reproducible, high quality thin films of the double-perovskite material Sr$_2$FeMoO$_6$ have been prepared by pulsed laser deposition. A thickness dependence of the substrate induced strain has been found. Moreover, it was shown that stain relaxation is strongly affected by the defect density in the thin films.

By structural and magnetic analysis of the epitaxial layers the close relation between strain, antisite disorder and the magnetic properties of the films could be verified. In the following chapter the relation to magnetotransport will be discussed.

Chapter 2

Magnetotransport in Sr_2FeMoO_6 thin films

Magnetotransport measurements are of vital importance both for studying the fundamental transport mechanism in this material as well as for testing its application potential. While polycrystals were optimised in order to exhibit maximum magnetoresistive effects by modifying the grain sizes, antisite disorder and oxygen content of the samples, the situation in the thin films is somewhat different. In order to gain a deeper insight into the microscopic origin of charge transport and to separate different contributions to the resistance high quality epitaxial material as well as samples of different quality with well characterised properties are required. The prepared Sr_2FeMoO_6 layers are most suitable for this task.

The magnetotransport behaviour of a large number of films was studied in a cryogenic system operating at temperatures from 4 K to 300 K. The cryostat is equipped with a variable temperature inset (VTI), allowing fast temperature sweeps as well as a high stability within most of the accessible temperature range. Under normal conditions a magnetic field of up to 12 T can be applied by means of a superconducting coil magnet. Further reducing the temperature of the helium bath allows to work at fields of up to 15 T.

2.1 Temperature dependent residual resistivity

Resistivity measurements were performed while sweeping the temperature from 275 K to 5 K at a rate of 1 K/min, which is a good compromise between temperature accuracy and duration. The films were contacted in van-der-Pauw geometry [51, 52] and measured by standard 4-probe method with a DC current of $10\mu A$. A representative selection of samples from all types were analysed in zero field and with an applied field of 1 T or 8 T perpendicular to the sample surface.

2.1.1 Thin film series A, B and C

The results obtained from sample series A again reflect the bad reproducibility
which was already seen in the structural and magnetic analysis. Two contrasting
examples are presented in Fig. 2.1. For some films metallic behaviour is observed
while others show an increase of the resistance with decreasing temperature, usu-
ally associated with insulating behaviour. In the present case the resistivity was
raised by a about two orders of magnitude compared to the metallic samples, not
enough to pass as insulators. The pronounced decrease of the resistivity with an
applied magnetic field can be found in both sorts of samples. This may be a hint
that the difference seen in the transport behaviour is not due a change of the
transport mechanism in the Sr_2FeMoO_6 phase itself but rather due to an addi-
tional contribution. An increase of the resistivity with decreasing temperature is
also frequently found in polycrystalline samples of this compound, see for exam-
ple Ref. [53], and has been related to an enhanced grain boundary contribution.
Therefore one can assume that the $SrMoO_4$ impurities, which have been clearly
identified in these films, lead to a modification of the grain boundaries.
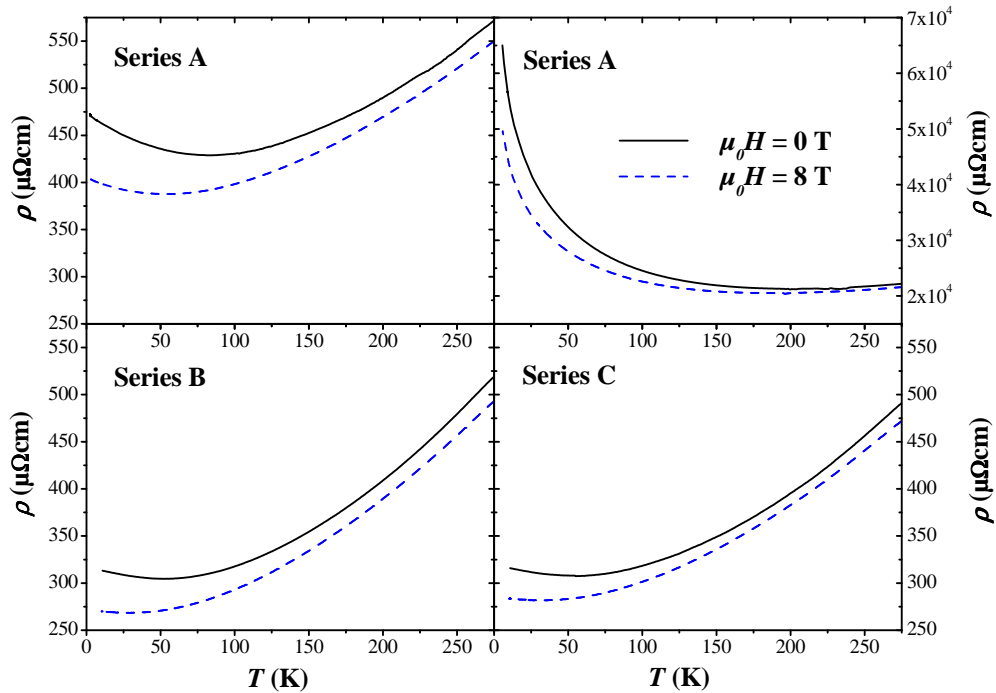
Figure 2.1: *Resistivity versus temperature in sample series A, B and C.
The black curves represent measurements at zero magnetic field, while the
measurements at a constant field of $\mu_0H = 8$ T are plotted in blue. For all
samples a negative magnetoresistance is found.*

Employing optimized preparation conditions we exclusively received metallic
samples (series B and C) with a resistivity of approximately 500 $\mu\Omega$cm at room
temperature. The residual resistivity ratio $\rho_{min}/\rho(275 \text{ K})$ is of the order of 0.5

which reveals that the quality of our films is very similar to single crystals of this compound. Typical transport measurements for thin film series B and C are presented in the lower panel of Fig. 2.1.

2.1.2 Thin films on $DyScO_3$ and $Ba_{0.4}Sr_{0.6}TiO_3$

In accordance with our expectations Sr_2FeMoO_6 thin films on $DyScO_3$ show a similar overall transport behaviour as described above for series B and C. To reveal the substrate influence a reference sample on $SrTiO_3$ was prepared prior to each film on $DyScO_3$ using the same preparation conditions. Since bulk behaviour is approached for very thick layers, samples of only 50 nm thickness were used for this study. In Fig. 2.2 resistivity versus temperature measurements of Sr_2FeMoO_6 on $DyScO_3$ and the respective reference sample are shown.
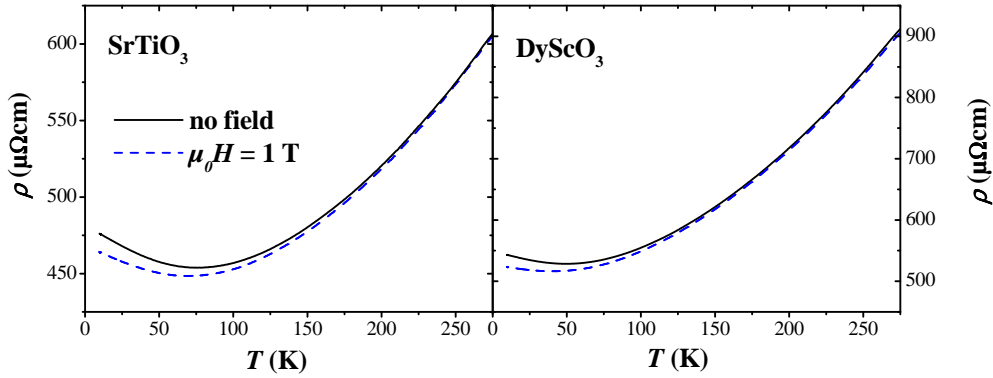
Figure 2.2: *Resistivity versus temperature in samples on $DyScO_3$.*

Compared to the reference sample the resistivity ratio $\rho_{min}/\rho(275\,K)$ is clearly improved from 0.75 to 0.58 which agrees with the nearly perfect crystal structure as described in section 1.2.4. The enhancement of metallicity and crystal quality provides evidence that Sr_2FeMoO_6 thin films with a low density of point defects and grain boundaries have been produced and emphasises the remarkably high sensitivity of this material with respect to the external strain caused by the lattice mismatch between sample and substrate. Due to the paramagnetic nature of the $DyScO_3$ substrate, magnetisation data from the thin films could not be extracted, but it is very likely that the saturation magnetisation will exceed the highest value of 3.06 μ_B/f.u. obtained in the case of $SrTiO_3$ substrates.

By introducing a buffer layer of $Ba_{0.4}Sr_{0.6}TiO_3$ we were able to minimise the substrate induced strain between $SrTiO_3$ and Sr_2FeMoO_6. But in contrast to the $DyScO_3$ substrate the $Ba_{0.4}Sr_{0.6}TiO_3$ buffer layer is not a single crystal and its grain structure is adopted by the Sr_2FeMoO_6 film due to the good lattice match between buffer layer and thin film material. Though the number of grain

boundaries in the sample has been strongly increased, no significant change is observed in the transport behaviour (Fig. 2.3). This indicates that the grain boundary contribution to the resistance is of minor importance for our films in contrast to polycrystalline samples of this material [7]. Nevertheless a slight increase of the MR ratio compared to all other sample types is seen. This issue will be discussed in detail in section 2.2.
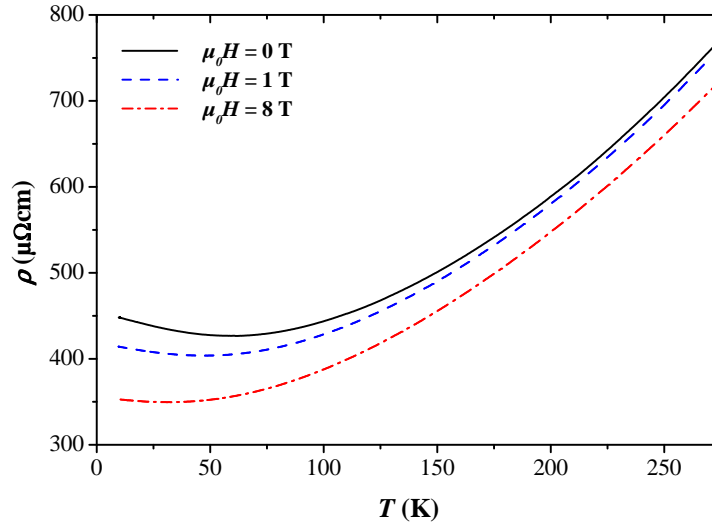
Figure 2.3: *Resistivity versus temperature in samples on $Ba_{0.4}Sr_{0.6}TiO_3$.*

2.1.3 Universal temperature dependence and resistivity minimum

As previously mentioned in Ref. [32] all samples exhibit a characteristic power law dependence for temperatures above T_{min}, i. e. the temperature where a resistance minimum is observed. In this range, the data can be well described with $\rho(T) = \rho_0 + \rho_2 T^2$, where ρ_2 is of the order of $10^{-9}\Omega\text{cm/K}^2$. Commonly such behaviour is associated with two possible interaction processes, i. e. electron-electron scattering or the absorption and emission of a single magnon. Yet electron-electron interaction should only contribute markedly at low temperatures and in systems with strongly enhanced carrier masses, which is not the case here. Single magnon interaction, on the other hand, gives rise to a T^2 behaviour in conventional ferromagnetic metals [54]. But this contribution, as it involves a spin-flip process, should be exponentially suppressed by $\exp(-E_G/k_B T)$ in a half-metal [55]. According to *ab initio* calculations [8] the majority up spin bands of Sr_2FeMoO_6 exhibit a bandgap of $E_G \approx 0.8$ eV implying a very substantial suppression of the electron-magnon contribution in the examined temperature range.

As shown by Wang and Zhang [56] the situation changes completely when a finite number of spin up states, which are Anderson localised and therefore do not

contribute to transport, is present. In this case the contribution of single magnon processes will recover due to Anderson localisation and give rise to a resistivity law of the form

$$\rho(T) = \rho_0 + \rho_{1.5}T^{1.5} + \rho_{2.5}T^{2.5}. \tag{2.1}$$

Using this concept a good agreement between measurement and simulation is achieved with $\rho_{1.5} \approx 10^{-2}\mu\Omega\text{cm}/\text{K}^{1.5}$ and $\rho_{2.5} \approx 10^{-4}\mu\Omega\text{cm}/\text{K}^{2.5}$. Therefore the latter approach seems to offer a plausible explanation for the observed temperature dependence. But one has to be aware that the coefficients cannot be treated as independent fitting parameters since they are determined by the derivative of the density of states at the Fermi energy. Accordingly the crossover temperature between domination of the $T^{1.5}$ term at low temperature and $T^{2.5}$ behaviour should be universal for all samples, which is not the case. Another drawback is encountered when the magnetic field dependence is studied. It is expected that the application of a magnetic field reduces the disorder and in turn the Anderson localisation length should increase. Consequently the single magnon scattering should be reduced. In contrast to this the resistivity curves measured at high magnetic fields are basically shifted to lower resistivity values whereas a reduction of the $T^{2.5}$ term is outweighed by a strong increase of the $T^{1.5}$ contribution (see Fig. 2.4).
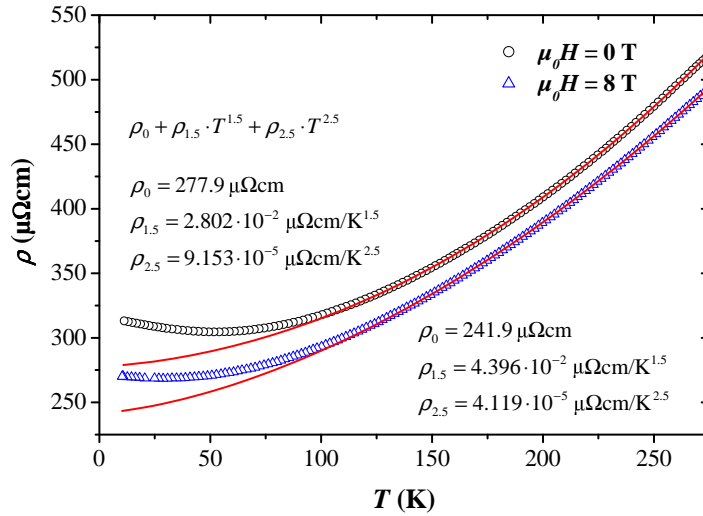
Figure 2.4: *Analysis of single-magnon scattering as a possible contribution to the resistance.*

Another scenario has been proposed on the basis of small-polaron transport by Zhao *et. al.* [57]. Initially developed for understanding the low temperature resistivity in manganites it is assumed that a strong polaronic effect as a second fundamental mechanism besides double exchange needs to be considered in order to explain basic physics in these compounds. While there is compelling evidence for the existence of polaronic carriers in manganese oxides, conclusive

studies about polarons in Sr_2FeMoO_6 are lacking. Nevertheless it is plausible to assume a similar mechanism being operative in this class of materials. Recalling the analogy between Fe/Mo pseudo double exchange and Zener double exchange, a strong interrelation between charge carrier transport and tilting of the oxygen octahedra is expected in both systems. Zhao *et. al.* argue that it is only the softest optical phonon branch associated with this tilting of the oxygen octahedra which contributes to the resistivity at low temperatures. Therefore the concept of small-polaron transport may also be considered for double perovskite materials. It should be noted that in manganites the existence of polarons is often associated with the Jahn-Teller distortion. Though these high-frequency Jahn-Teller modes are strongly coupled to the carriers their contribution is small due to an exponentially small relaxation rate and do not enter into this model. Pursuing a theory of small-polaron conduction worked out in the sixties Zhao *et. al.* propose the following expression

$$\rho(T) = \rho_0 + E\omega_s/\sinh^2(\hbar\omega_s/2k_BT), \tag{2.2}$$

where ω_s (average frequency of the softest optical phonon mode) and E (proportional to the effective mass of polarons) are introduced as fitting parameters. The result of applying this model to our data is displayed in Fig. 2.5.
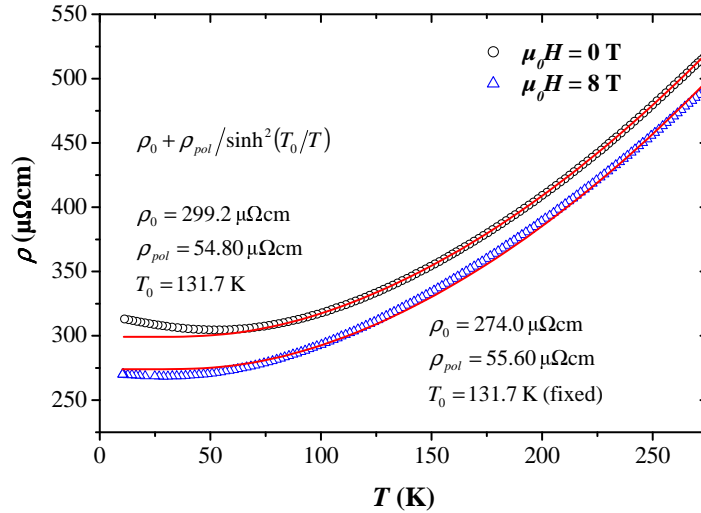
Figure 2.5: *Analysis of the temperature dependent resistivity with a model of small-polaron transport according to Zhao et. al. [57].*

At moderately low temperature a very good agreement between our data and the proposed simulation model could be established. It cannot attribute though for the resistance minimum which is commonly observed in the Sr_2FeMoO_6 samples. Additionally, deviations from the model become more pronounced when the high field resistance is analysed. These are strong indications that the choice of a single contribution dominating the temperature dependence is oversimplified.

Certainly this is not surprising given the large number of possible interaction mechanisms among which only the single magnon process and the small-polaron model have been discussed in detail. Nevertheless the small-polaron model does indeed give the best description of our data, suggesting that further studies in order to confirm the assumption of strong polaronic effects in double perovskites, specifically Sr_2FeMoO_6, are required.

Having largely ignored the influence of disorder and possible grain boundary contributions for some time, I shall now address their consequences. In several examples of standard solid state theory the introduction of defects into an ideal metal is accompanied by a characteristical resistance rise approaching zero temperature, with the most prominent example in this context certainly being the Kondo effect [58]. In turn it is natural to assume that the resistance rise which is typically observed in our samples originates also from the above mentioned defects. In the high quality samples of series B and C the resistance minimum is typically reached around 50 K and shifts to lower temperatures by an applied magnetic field.

A work by Rozenberg *et. al.* [59], where similar effects in magnetoresistive manganites are discussed, utilises two different approaches which will be introduced and applied to Sr_2FeMoO_6 in the following. One is based on the concept of bulk-scattering, supposing that the resistance is dominated by elastic and inelastic scattering processes in the bulk material, while the other is using the approach of inter-grain tunnelling. For sufficiently high barriers between adjacent grains antiferromagnetic exchange interactions have been predicted. They eventually modify the resistivity by a factor which is a decreasing function of T. So both models in principle are able to explain the occurrence of a resistivity minimum. The important point which has been elucidated in Ref. [59] is the behaviour upon the application of a magnetic field which is a crucial test for the discussed models. While the bulk-scattering approach did not allow to model the large shift of the minimum to lower temperatures, the inter-grain tunnelling model provides a qualitative description of the experiment.

Analogous to the calculations in Ref. [59] the bulk-scattering model was thus evaluated for Sr_2FeMoO_6 with the respective parameters of carrier density and mean free path. The latter approach is starting from the following representation of the resistance

$$\rho = \rho_{el} + \rho_{in}, \tag{2.3}$$

where ρ_{el} and ρ_{in} are the contributions due to elastic (electron-impurity and Coulomb interaction) and inelastic (e. g. electron-phonon and electron-single magnon interaction) processes. The inelastic term is increasing with temperature and can usually be described by a power law $\rho_{in} = bT^p$, which is also a good approximation for Sr_2FeMoO_6 as discussed above [32]. The coefficient b is

regarded as being independent of the applied field H. As a result of disorder temperature and field dependencies appear in ρ_{el} due to Coulomb interaction (CI) and decoherence effects. Using the CI correction from Ref. [60] valid for $H = 0$, Eq. 2.3 can be rewritten as:

$$\rho(T, 0) = \rho_0 - aT^{-1/2} + bT^p, \tag{2.4}$$

At zero field we thus obtain an expression with increasing as well as decreasing temperature-dependent terms. In a more recent work Aleiner *et. al.* [61] addressed the problem of CI and dephasing (DP) at non-zero magnetic fields. The residual conductivity $\sigma_{el} = 1/\rho_{el}$ then takes the form

$$\sigma_{el}(T, H) = \sigma_0 + \delta\sigma_{CI}(T, H) + \delta\sigma_{DP}(T, H). \tag{2.5}$$

Since only one- and two-dimensional cases are considered in Ref. [61] Rozenberg *et. al.* recalculated the correction terms in the high field limit to obtain approximations applicable in 3 dimensions, yielding Eq. 2.6 for the CI correction

$$\frac{\delta\sigma_{CI}(T, H) - \delta\sigma_{CI}(T, 0)}{\delta\sigma_{CI}(T, 0)} = -0.7510(k_F^2 ll_H)^{-1}, \tag{2.6}$$

where $l_H = \sqrt{\hbar/eH}$ is the magnetic length. Using a free electron approximation, the Fermi wave number for Sr_2FeMoO_6 $k_F \approx 6 \cdot 10^{10}$ m^{-1} is derived from the carrier density $n \approx 8 \cdot 10^{21}$ cm^{-3}. The mean free path $l \approx 1$ nm as well as n have been determined by Hall effect measurements [62]. With these values the relative change of $\delta\sigma_{CI}$ for an external magnetic field of 10 T amounts to about -0.3%. This result is very similar to what has been deduced by Rozenberg *et. al.* for the manganites. The dephasing term is given by

$$\delta\sigma_{DP}(T, H) = \frac{e^2}{(2\pi)^2\hbar}\sqrt{4l_H^{-2} + L_\varphi^{-2}}, \tag{2.7}$$

where

$$L_\varphi = \left[14.7336(k_F^2 lL_T^3)^{-1} \left(1 - 1.2794\frac{2L_T}{l_H}ln\frac{l_H}{2L_T}\right) \right]^{-1/2}, \tag{2.8}$$

is the length of dephasing by CI and $L_T = \sqrt{\hbar D/k_B T}$, with $D = v_F l/3$ the carriers diffusion constant and v_F the Fermi velocity. Plugging in the respective values for Sr_2FeMoO_6 yields $l_H \ll L_\varphi$ verifying that this calculation is consistent with the prerequisite of small l_H/L_φ.

By employing the MATLAB software, resistance versus temperature curves were simulated but the size of dephasing and CI corrections are too small to account for the observed increase at low temperatures and the magnetic field dependency. Adapting the magnitude of these corrections by introducing additional fitting factors reveals that dephasing and CI have to be raised by about one and four orders of magnitude, respectively. It has to be concluded that these quantum corrections to conductivity do not play an important role here.

2.2 Magnetoresistance

The nature of the magnetoresistance effect can be studied in more detail when the resistance dependency on the applied magnetic field is measured while the temperature remains fixed. A representative MR curve for an epitaxial Sr_2FeMoO_6 thin film is shown in Fig. 2.6. For comparison the typical resistance versus field behaviour of a polycrystalline bulk sample, taken from Ref. [50], is plotted.
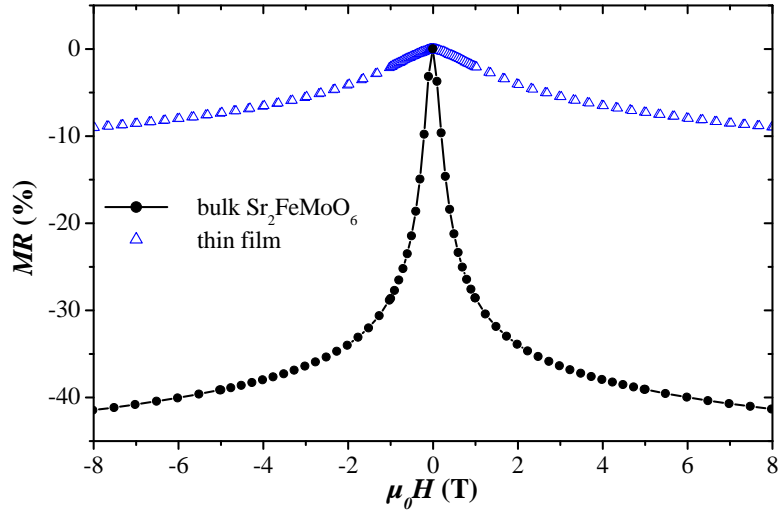
Figure 2.6: *Magnetoresistance versus magnetic field for bulk polycrystals and epitaxial thin films.*

Generally the acquired curves are analysed with respect to the magnetoresistance effect in the low field range (LFMR), typically defined by the saturation field of the respective material $H \approx H_s$, and in the high field region (HFMR) at several Teslas. A large LFMR is observed in the polycrystalline bulk samples which is attributed to the strong contribution of grain boundaries as described in section 1.1.2. In the epitaxial film this contribution is small due to the absence of large angle GB's with appreciable barrier height. The HFMR on the contrary is of comparable size for both sample types being consistent with the assumption that disorder induced magnetic defects act as scattering centres. Paramagnetic defects as well as AFM coupled regions and frustrated spin configurations which have been suggested by the magnetic analysis in section 1.3.2 contribute in this regime. Within our used measurement range of up to 8 T these contributions are decreasing almost linearly suggesting that much higher fields are necessary in order to fully saturate the spin disordered regions.

Since we are interested in the change of the resistance with applied field, it can be instructive to study the derivative of the magnetoresistance instead of the MR itself. The numerically determined *MR'* values of the previously discussed data is presented in Fig. 2.7.
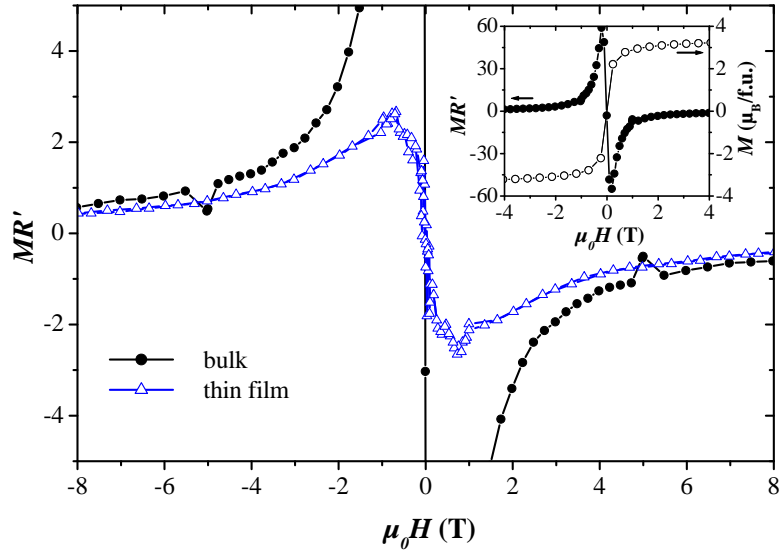
Figure 2.7: *Derivative of MR versus magnetic field for bulk polycrystals and epitaxial thin films. The inset illustrates the close relation between evolution of MR effect and the sample magnetisation as function of the applied field for the bulk polycrystal.*

In these plots the crossover between LFMR and HFMR becomes more evident. To illustrate the close relationship between the magnetisation M and the MR effect, MR' and M are shown in the inset of Fig. 2.7 for the polycrystalline sample. The maximum in MR' is observed around 200 mT, corresponding to the region in which the magnetisation switches to about 65% of the saturation value. In the intermediate field range as M_s is approached more and more gradually, MR' decreases. Once the sample is fully saturated, MR enters into the linear region of HFMR.

For the epitaxial thin films the maximum of MR' is reached at slightly higher fields compared to the bulk material though their magnetisation curves are alike. This fact suggests that an additional contribution becomes important in the films. As an alternative source of LFMR García-Hernández *et. al.* [50] suggested that the antisite disordered regions, i. e. the antiferromagnetic (AFM) Fe-O-Fe patches, and to a much lesser extent the paramagnetic Mo-O-Mo ones, could form boundaries which will then act in a similar way as the grain boundaries. Furthermore, provided the Fe-O-Fe patches are not very large, the AFM interaction within these regions has to compete with the FM ones imposed by the surrounding material. Thus, the AFM order is partially broken when an external field is applied, reducing the effective size of these patches as shown in Fig. 2.8. In this approach the crossover to the high field regime occurs when the disordered regions become disjunct. As a consequence they can be regarded as randomly distributed defects in an ordered matrix acting as scattering centres as described above.
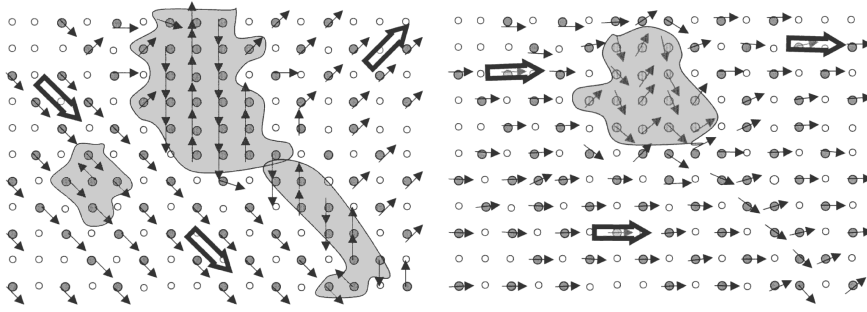
Figure 2.8: *Antisite boundaries as a source of low field magnetoresistance as suggested by García-Hernández et. al. [50]. The grey dots (open circles) represent the Fe (Mo) ions. For simplicity, the magnetisation vector is indicated only at the Fe ions.*

This model is commonly regarded as being of little relevance for the LFMR seen in polycrystalline bulk samples, though initially developed for this purpose. Nevertheless, the present study provides evidence that such effects do exist. Due to the much lower influence of grain boundaries in the epitaxial thin films the antisite contribution seems to govern the low temperature regime in these samples.

In the following the field dependent MR measurements have been carried out with the magnetic field direction perpendicular to the sample surface. For this configuration the demagnetisation factor $D \approx 1$ has to be taken into account. As a result the sample only sees a reduced field which is given by

$$H_{sample} = (H_{ext} - M), \tag{2.9}$$

where H_{ext} is the applied field and M the respective sample magnetisation.

2.2.1 Magnetoresistance in thin film series B and C

After pointing out the obvious differences between MR in bulk polycrystals and epitaxial thin films, I want to draw the reader's attention to the comparable subtle distinction between thin film samples of series B and C. Already from the zero and high field resistivity measurements of the previous section we learn that the MR ratio at 8 T is always smaller for samples C. The MR as plotted in Fig. 2.9 is extracted from the data of Fig. 2.1 using the formula

$$MR[\%] = \frac{\rho(T, H) - \rho(T, 0)}{\rho(T, H)}. \tag{2.10}$$

The origin of a different MR response becomes evident when the magnetoresistance as a function of field is analysed. In Figure 2.10 the respective measurements and their derivatives are shown. Consistent with the improved crystal
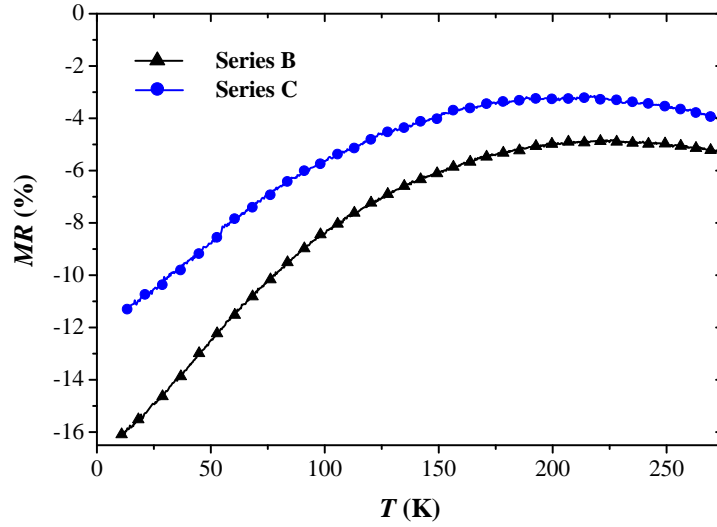
Figure 2.9:   *Temperature dependent magnetoresistance ($\mu_0 H = 8$ T) in representative samples of series B and C.*

quality of series C these samples exhibit a lower LFMR, while the derivatives suggest that the HFMR contributions are comparable. This is in accordance with our expectations since similar values of M_s, associated with a certain amount of antisite disorder, should render similar defect densities.
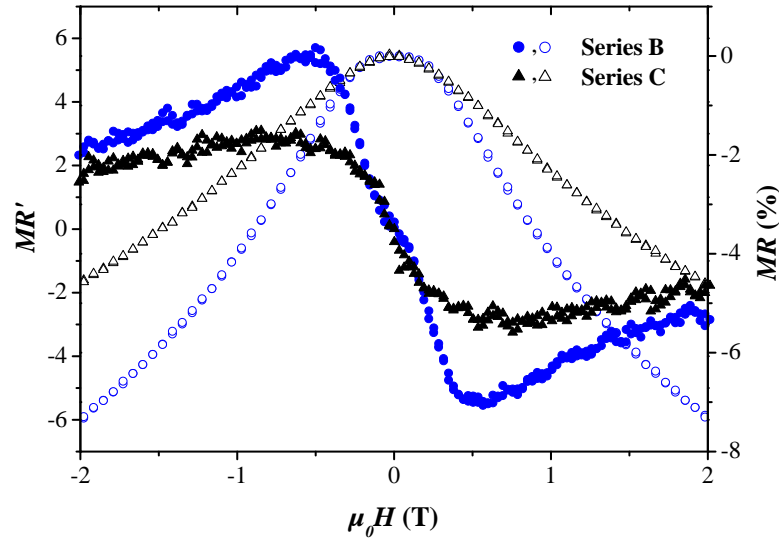
Figure 2.10:   *Magnetoresistance and derivative versus magnetic field for epitaxial thin films of series B and C at $T = 10$ K. MR (right scale) and its derivative MR' (left scale) are plotted using open and filled symbols, respectively.*

However, one has to remember that for samples with much higher disorder levels, the spin polarisation will decrease and therefore an overall reduction of the MR response is observed.

2.2.2 Magnetoresistance in highly epitaxial and textured thin films

With the analysis of the MR effect in a highly epitaxial Sr_2FeMoO_6 layer on $DyScO_3$ and a textured film on $Ba_{0.4}Sr_{0.6}TiO_3$ this chapter will conclude. It is exemplified that the rules which have been worked out in the previous section remain valid also for these two extreme cases of reduced structural defects and enhanced GB contributions, respectively.

Figure 2.11 is obtained from the temperature dependent resistivity data of Figs. 2.2 and 2.3. Due to a magnetic field induced phase transition of the $DyScO_3$ which occurs at approximately 5 T at room temperature, the high field curve could not be recorded for the respective sample. In order to point out more clearly the strong increase of MR when using a $Ba_{0.4}Sr_{0.6}TiO_3$ buffer layer, the 8 T curve is plotted in the inset of Fig. 2.11 alongside with the previously discussed result for a representative sample of series B.
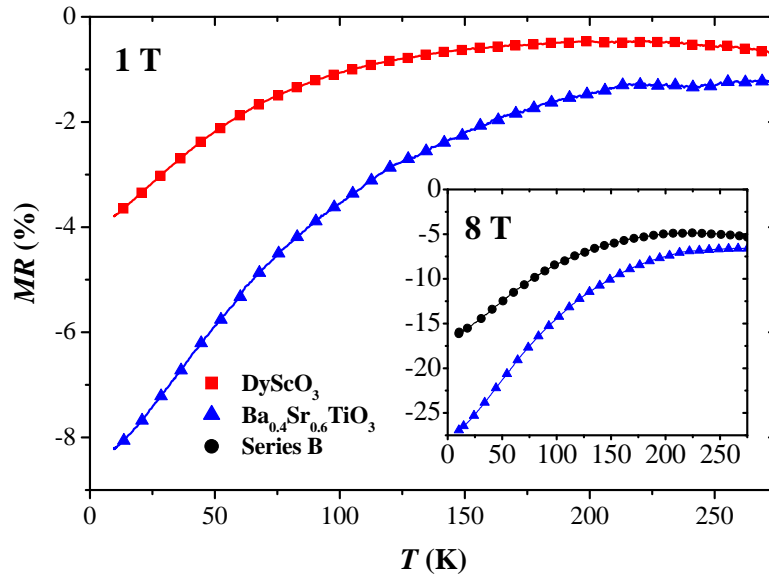
Figure 2.11: *Temperature dependent magnetoresistance ($\mu_0 H = 1$ T) in Sr_2FeMoO_6 thin films on $DyScO_3$ substrates and on $SrTiO_3$ with a $Ba_{0.4}Sr_{0.6}TiO_3$ buffer layer.*

Though the resistance versus temperature curve in Fig. 2.3 does not reveal a distinct difference in the transport behaviour when comparing epitaxial and textured layers, the increase in MR as shown above is dramatic especially with respect to the low field contribution (see Fig. 2.12). This behaviour is attributed to the influence of two main effects both originating from the reduced structural impact of the substrate. Firstly, the increased crystal texture leads to the formation of large angle grain boundaries and secondly, the reduction of strain by the nearly perfect lattice match between $Ba_{0.4}Sr_{0.6}TiO_3$ and Sr_2FeMoO_6 reduces the

probability of defect formation in the grains. Therefore the increase of LFMR is identified as a grain boundary contribution while the HFMR remains practically the same.
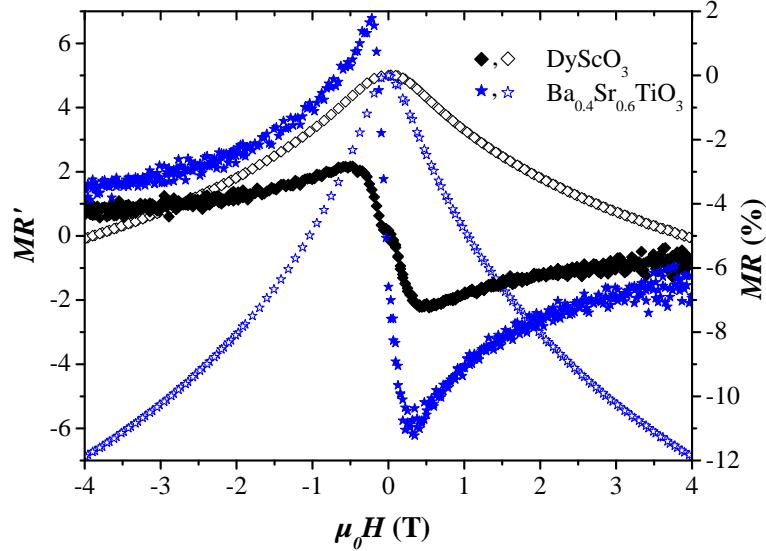
Figure 2.12: *Magnetoresistance and derivative versus magnetic field for epitaxial thin films on $DyScO_3$ and textured thin films using a $Ba_{0.4}Sr_{0.6}TiO_3$ buffer layer. MR (right scale) and its derivative MR' (left scale) are plotted using open and filled symbols, respectively.*

The films deposited on $DyScO_3$ exhibit a considerably lower magnetoresistance over the whole field range as shown in Fig. 2.12. From the reduction of the HFMR it can be concluded that these films have the lowest defect density of all prepared samples. Moreover, the observed magnetoresistance is comparable to the effect in bulk single crystals of Refs. [22, 23].

The careful study, involving samples on different types of substrates, allowed us to get a close insight into the complex mechanisms of charge transport and magnetoresistance in this material. The temperature dependence of resistivity in films with high epitaxial quality and well ordered cation sublattice can be reproduced by small-polaron transport. Deviations, which occur for temperatures below 50 K, are attributed to the small but non-zero structural disorder. However, it was shown that quantum corrections due to Coulomb interaction and dephasing cannot play an important role here.

In a detail analysis of the field dependent magnetoresistance intra- and inter-grain contributions have been identified in the low temperature regime. We arrive at the conclusion that grain boundaries are effectively contributing to the LFMR in this system but their influence is outweighed by disorder induced LFMR in the epitaxial samples.

Investigating the spin polarisation of magnetoresistive materials by point contact spectroscopy

An important task in the investigation of potential half-metallic materials is the experimental validation of a high spin polarisation value. To date a variety of methods have become available, but many still have to give proof of their experimental feasibility. Amongst them the analysis of the Andreev reflection process in point contact junctions (PCAR) has attracted much interest. In need of a straightforward method, the study of its physical limitations has been neglected so far. Consequently, this chapter will be devoted to the clarification of a basic problem, which is frequently encountered in experimental studies, namely the influence of specific resistivity on the resulting spin polarisation in highly resistive probe materials.

I will start with a short introduction of the most commonly used techniques, ranging from optical measurements to the evaluation of transport phenomena. In preparation for the analysis of experimental results, the theoretical background of PCAR is studied in detail.

3.1 Experimental methods for probing the spin polarisation

One could argue that once a trilayer tunnelling device, consisting of an insulating barrier sandwiched between two magnetic layers, has been fabricated, the spin polarisation of the magnetic electrode can be inferred from the magnitude of the

tunnelling magnetoresistance (TMR) effect. But this method suffers for example from the influence of non-ideal interfaces, current distribution effects [63], and the impact of different barrier materials is still under discussion [64]. Therefore the real potential of the investigated material may remain unrecognised. Apart from this, it is desirable to measure the spin polarisation prior to the time-consuming development of such a tunnelling device. In consequence alternative methods are needed. Most prominent candidates are spin-polarised photoemission experiments, the Meservey-Tedrow technique and the analysis of Andreev reflection suppression in point contacts.

3.1.1   Spin-polarised photoemission

Photoemission is widely used in the study of the electronic structure of solids (see for example Ref. [65, 66]). It utilizes the photoelectric effect in which an electron is ejected from the occupied electronic levels of the sample as shown in Fig. 3.1.
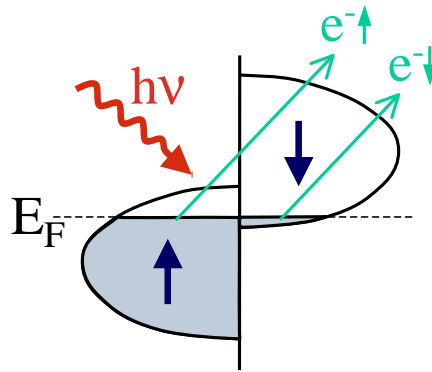
Figure 3.1:   *To study the spin polarisation by photoemission experiments, the excitation energy, which is supplied by laser or synchrotron radiation, is tuned to the Fermi level and the spin of the emitted electrons is analysed.*

By either using circularly polarised light to excite the electrons or employing a spin sensitive detector [65] the spin state of the emitted electrons can be resolved. It should be emphasised that this method allows a direct probe of the density of states spin polarisation P_0 which is simply given by the imbalance of up and down spin density of states $N_{\uparrow\downarrow}$

$$P_0 = \frac{N_\uparrow - N_\downarrow}{N_\uparrow + N_\downarrow}. \tag{3.1}$$

In a photoemission experiment, the kinetic energy of the photoelectrons usually varies from a few electron volts up to a few hundred electron volts, depending on the photon energy used. As a result this technique is highly surface sensitive with the inelastic mean free path of a typical photoelectron in the solid ranging between 5-30 Å.

This has consequences concerning the applicability of the technique. While thin films of elementary metals, which have been widely studied, are prepared in ultra high vacuum conditions and analysed in situ, the investigation of complex materials, in our case the double-perovskite oxide Sr_2FeMoO_6, usually involves a sample transfer from the preparation chamber to the photoemission setup. Even when all precautions to avoid degradation are taken, a surface modification by minor contamination levels cannot be fully excluded. Furthermore, the existence of a surface/interface alone can have a detrimental effect on the level of spin polarisation, which has been shown for some complex materials by band structure calculations [67, 68].

3.1.2 The Meservey-Tedrow technique

The method of studying spin-dependent tunnelling in a junction between a thin superconducting Al layer and a magnetic film (see Fig. 3.2), pioneered by Meservey and Tedrow [69], exploits some convenient properties of Al. Besides being comparably simple to prepare as a thin film, Al surface oxidation is self-limiting which is ideal for obtaining a well-defined tunnelling barrier. But most importantly Al thin films with thicknesses of 4 nm or less exhibit enhanced T_C values of up to 2.5 K and large critical fields $H_{C2\parallel}$ which are Pauli limited. This is resulting from a combination of different effects. For a very thin film with thickness d much smaller than the superconductor penetration depth, the orbital depairing parameter becomes very small.
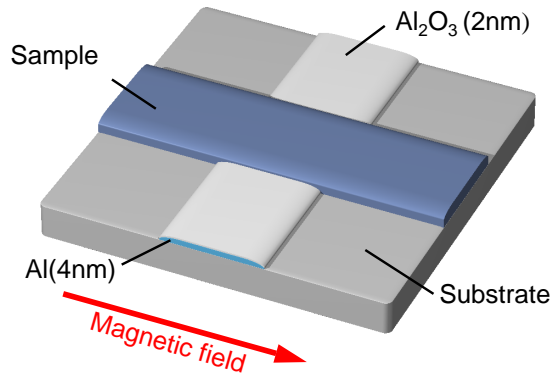
Figure 3.2: *Typical sample layout for Al-Al_2O_3-metal junctions. To obtain a well defined Al_2O_3 barrier and optimum properties of the superconducting Al electrode, it is useful to start with an Al base electrode, which is then carefully oxidised. The probe material is subsequently deposited on top.*

When a magnetic field parallel to the film surface is applied, it penetrates the sample nearly uniformly and thus the orbital effects of screening currents are negligible. As spin-orbit scattering is proportional to Z^4, with Z the atomic number, it is small for Al. In this case the Pauli paramagnetism, which leads

to a reduction of the normal state energy, limits the critical field. At sufficiently low temperatures and high magnetic fields the strong spin interaction with the magnetic field lead to a Zeeman splitting of the quasiparticle density of states as illustrated in Fig. 3.3.
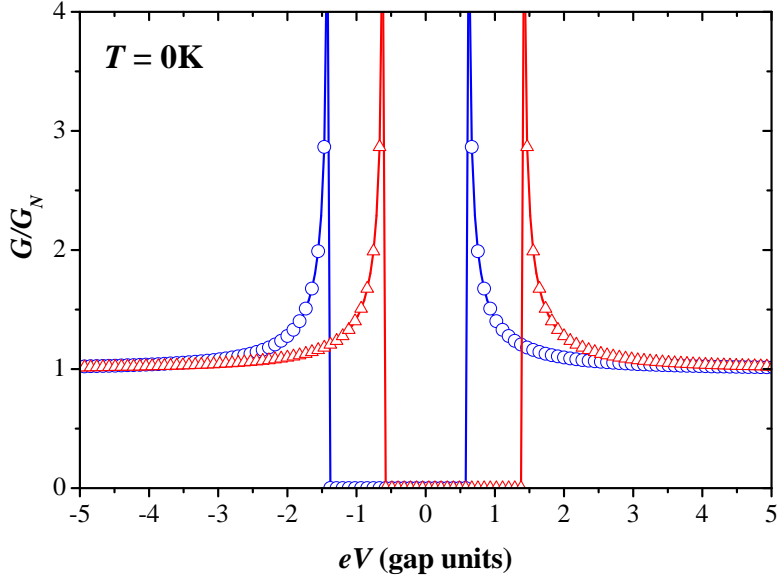
Figure 3.3: *Zeeman shifted quasiparticle density of states as seen by the electrons with spin up (blue circles) and spin down (red triangles) when approaching the junction.*

As the density of states has sharp peaks at the energy value of the superconducting gap, the Zeeman shift can be easily resolved in the conductance of a $Al-Al_2O_3$-metal tunnelling junction. As an example simulations for two contrasting cases have been performed (see Fig. 3.4). When probing an unpolarised material, which means that $P = 0$, a symmetric spectrum is obtained. In the second example, where a transport spin polarisation of $P = 0.5$ was assumed, the imbalance of spin up and spin down charge carriers lead to an asymmetric shape of the spectrum.

For a quantitative analysis of experimental data the field depairing parameter ζ and spin-orbit scattering b are introduced in the fitting routine. Using this technique a variety of different materials, ranging from elementary ferromagnetic metals and different 3d metal alloys to the half-Heusler NiMnSb or the perovskite oxide $La_{2/3}Sr_{1/3}MnO_3$, have been analysed [70, 71, 72]. Though the results are often compared to those values which have been obtained from photoemission, one has to keep in mind that tunnelling experiments are sensitive mainly to the charge carriers with high mobility and thus the probed spin polarisation is given by

$$P_1 = \frac{N_\uparrow v_\uparrow T_\uparrow - N_\downarrow v_\downarrow T_\downarrow}{N_\uparrow v_\uparrow T_\uparrow + N_\downarrow v_\downarrow T_\downarrow}, \tag{3.2}$$
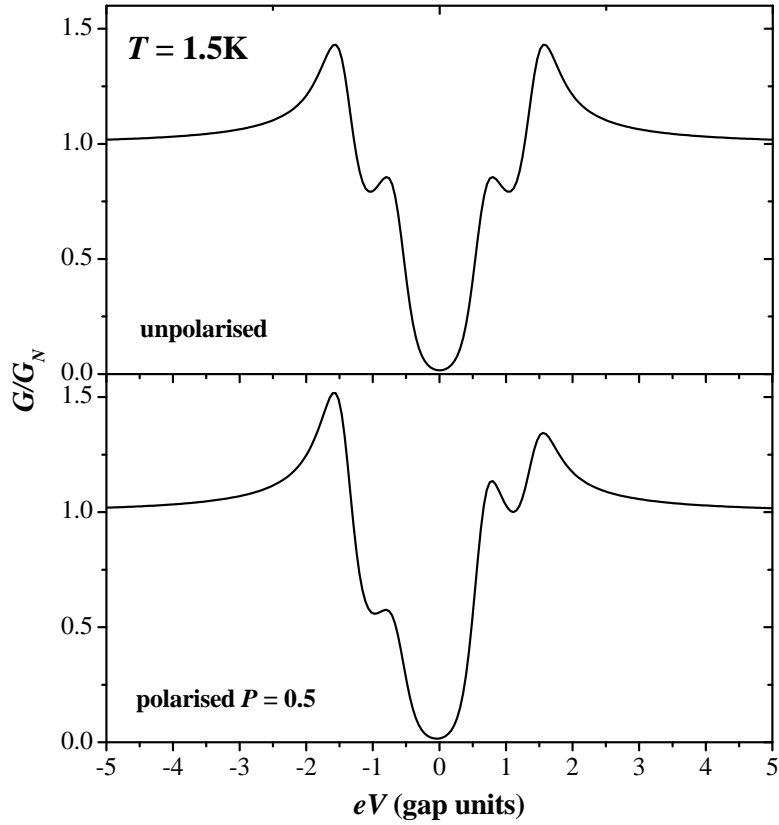
Figure 3.4: *Simulations of Meservey-Tedrow spectra corresponding to Al-AlO$_3$-metal junctions with unpolarised (upper panel) and 50% spin polarised (lower panel) probe materials at $T = 1.5$ K. The shift corresponds to Δ=0.3 meV and a magnetic field of $B = 2$ T.*

where $N_\uparrow$ and $N_\downarrow$ are the up and down spin density of states, $v_{\uparrow\downarrow}$ and $T_{\uparrow\downarrow}$ the respective Fermi velocities and transmission coefficients. Moreover, as this method discriminates between majority and minority carrier also the sign of spin polarisation can be extracted.

Though having emerged as a powerful tool, the Meservey-Tedrow technique cannot be applied easily to new materials. Comparable to the fabrication of magnetic tunnelling devices it poses high demands on sample preparation. However it has the advantage of being insensitive to the junction size as a potential difference parallel to the junction is ruled out due to the superconducting electrode.

3.1.3 Point Contact Andreev Reflection

Another widespread method for probing the degree of spin polarisation is to study the spin-dependent suppression of Andreev reflection at a transparent metal/superconductor nanocontact as proposed by Soulen *et. al.* [73] and Upadhyay *et. al.* [74].

The Andreev reflection process occurs when a single electron with energy below the superconducting energy gap Δ propagates from the metal to the superconductor and vice versa. At the interface it is transformed into a Cooper pair by reflecting a hole with opposite spin and momentum. For the simplest case of a non-magnetic metal and matching fermi-surfaces the conductance across the interface for applied voltages $eV < \Delta$ is thus doubled. Due to an imbalance of the current transport for up and down spin electrons, referred to as transport spin polarisation P, this effect can be suppressed as illustrated in Fig. 3.5. Thus analysing measured $dI/dV(V)$ conductance curves allows in principle determination of P.
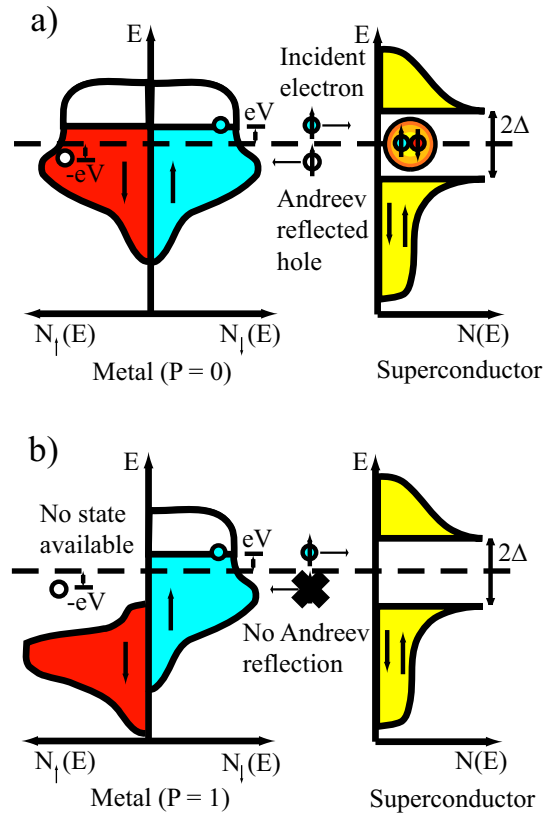
Figure 3.5:   *Schematic representation of the Andreev reflection process (a) and its total suppression for a fully spin polarised metal electrode (b). Please note that the superconducting gap is exaggerated with respect to the size of the metal bands and that the Cooper-pairs do not show up in this superconductor representation. (Taken from Ref. [73])*

Compared to the previously introduced techniques, the PCAR method has the advantage of a comparably simple experimental setup which allows to investigate bulk as well as thin film samples. By establishing a contact between the probe material and a sharp superconducting tip, degraded surface layers are penetrated and thus the influence of surface effects are minimised.

Typical junction diameters of such mechanical contacts are of the order of

10 nm to 100 nm. The contact area a is a crucial parameter since the anomalies in the linear-response conductance are only observable for coherent transport, i.e. in the limit of either ballistic transport $l_e > a$ (Sharvin limit) or diffusive transport $l_i > a > l_e$, where l_e and l_i are the elastic and inelastic mean free paths of the electron.

Experimentally the limit of ballistic transport can be attained for good conductors especially 3d metals in contact with a BCS superconductor. However, for a large number of promising materials, amongst them most metallic oxides, the specific resistivities observed are magnitudes larger. In the case of the widely studied manganites specific resistivities around 100 $\mu\Omega$cm are observed for single crystals and thin films [75, 76]. For Sr_2FeMoO_6 single crystals $\rho \approx 200$ $\mu\Omega$cm is found [22, 77], whereas for thin films $\rho \approx 500$ $\mu\Omega$cm [78] is achieved. Therefore contacts with such materials are expected to exhibit either diffusive or thermal transport. Due to the strong dependence of the transport regime on contact radius and specific resistivity, i.e. mean free path, a crucial point for the analysis is the determination of these quantities for each contact. From the bulk conductivity the specific resistivity and thus the mean free path can be estimated. By employing Wexler's formula [79]

$$R_K \approx \frac{4}{3\pi} \frac{\rho l}{a^2} + \frac{\rho}{2a},\qquad(3.3)$$

which describes the contact resistance R_K with an expression depending on the specific resistivity ρ, the mean free path l and the contact radius a, an approximation for a can be derived. Yet this estimate is very rough for a couple of reasons. For example Eq. (3.3) is only true for a perfectly transparent junction, i.e. the influence of a barrier on the contact resistance is not taken into account and also the bulk specific resistivity can be changed at the junction due to the influence of the surface. To improve the approximation of the contact size the fraction $R_M = \rho/2a$ was identified in previous studies by comparing the T-dependent resistivity of the probed material with the T-dependence of R_K [80]. In the case of Sr_2FeMoO_6 and $Co_2Cr_{0.6}Fe_{0.4}Al$ the T-dependence in the relevant temperature range is small, so this method cannot be applied here.

Without the possibility to deduce a reliable value for the contact radius a directly from the measured quantities one has to rely on the power of the theoretical models, which will be described in the following section. In order to obtain a decisive result it has to be shown that the spectra can be interpreted uniquely within one of these pictures. Thus, in the discussion of the experimental results various approaches will be considered.

Furthermore, one has to be aware that the extracted transport spin polarisation P is not uniquely defined. Its magnitude and sign are not necessarily

reflecting the up and down spin density of states P_0, since P not only depends on P_0 but also on mobility of the charge carriers, the overlap between the Fermi surfaces of the superconductor and the respective minority and majority surfaces of the metal, as well as the transport regime [81, 82, 83, 84, 85]. Therefore it is useful to introduce a generalised transport spin polarisation P_n, defined as

$$P_n = \frac{N_\uparrow v_\uparrow^n T_\uparrow - N_\downarrow v_\downarrow^n T_\downarrow}{N_\uparrow v_\uparrow^n T_\uparrow + N_\downarrow v_\downarrow^n T_\downarrow}. \tag{3.4}$$

Yet, only for clean contacts in the ballistic <u>or</u> diffusive regime Eq. (3.4) is explicitly known, i. e. the transmission coefficients T_σ approach 1 and n is well defined. The spin polarisation probed by ballistic contacts is P_1, which means that the up and down density of states are weighed linearly with the respective Fermi velocities v_σ whereas P_2 is measured in the diffusive case.

3.2 Theoretical basis of Andreev reflection in metal/superconductor junctions

The comprehension of metal/superconductor junctions has been strongly promoted by a work of Blonder, Tinkham and Klapwijk [86], which was established by employing the concepts of BCS theory. Therefore my short review will start with some basic remarks on the microscopic theory of superconductivity before proceeding with a description of the BTK model.

3.2.1 BCS theory of superconductivity

Bardeen, Cooper and Schrieffer successfully proposed the BCS theory as a microscopic explanation for superconductivity. The starting point of this work was the discovery, that two electrons above the Fermi sea can form an energetically favoured pair, a so called Cooper pair, when an attractive interaction is present, no matter how small. It was shown that a positive interaction can originate from the interaction of the electrons with a lattice of ion cores. The first electron travels through the lattice polarising the medium by attracting the positively charged ions. Due to the stiffness of the ion cores an excess positive charge remains which attracts a second electron and leads to a net attraction between the electrons. The electron pair, which is characterised by a singlet wavefunction is found to have minimum energy. It is given in second quantisation by the expression

$$|\psi_0\rangle = \sum_{k>k_F} g_{\vec{k}} c_{\vec{k}\uparrow}^\star c_{-\vec{k}\downarrow}^\star |F\rangle, \tag{3.5}$$

where $c^{\star}_{\vec{k}\uparrow}$ ($c_{\vec{k}\uparrow}$) is the creation (annihilation) operator for an electron of momentum $\vec{k}$ with spin up and $|F\rangle$ the Fermi sea with all states filled up to k_F.

If an instability with respect to the formation of one Cooper pair is present, electrons are going to condense into pairs until equilibrium is reached. The resulting ground state, assuming a large number of Cooper pairs, has the form

$$|\psi_G\rangle = \prod_{\vec{k}=\vec{k}_1,...,\vec{k}_M} \left(u_{\vec{k}} + v_{\vec{k}} c^{\star}_{\vec{k}\uparrow} c^{\star}_{-\vec{k}\downarrow} \right) |\phi_0\rangle. \tag{3.6}$$

The BCS coherence factors $u_{\vec{k}}$ and $v_{\vec{k}}$ have to fulfil the relation $|u_{\vec{k}}|^2 + |v_{\vec{k}}|^2 = 1$, where $|v_{\vec{k}}|^2$ ($|u_{\vec{k}}|^2$) is the probability for the pair state ($\vec{k}\uparrow, -\vec{k}\downarrow$) to be occupied (unoccupied), and $|\phi_0\rangle$ is the vacuum state.

To solve the problem explicitly the coherence factors need to be determined. This can be done either with a variational calculation or by canonical transformation. After introducing the BCS pairing Hamiltonian $\mathcal{H}$ I will proceed with the latter approach. By writing

$$\mathcal{H} = \sum_{\vec{k}\sigma} \epsilon_{\vec{k}} c^{\star}_{\vec{k}\sigma} c_{\vec{k}\sigma} + \sum_{\vec{k}\vec{l}} V_{\vec{k}\vec{l}} c^{\star}_{\vec{k}\uparrow} c^{\star}_{-\vec{k}\downarrow} c_{-\vec{l}\downarrow} c_{\vec{l}\uparrow}, \tag{3.7}$$

the Cooper pair interaction with the interaction potential $V_{\vec{k}\vec{l}}$ is taken to render the only significant contribution to the problem, which is usually a good approximation. Due to the large number of pairs it is useful to express the pair annihilation operator as a sum of its expectation value $b_{\vec{k}} = \langle c_{-\vec{k}\downarrow} c_{\vec{k}\uparrow} \rangle$ and the fluctuation, which should be small

$$c_{-\vec{k}\downarrow} c_{\vec{k}\uparrow} = b_{\vec{k}} + (c_{-\vec{k}\downarrow} c_{\vec{k}\uparrow} - b_{\vec{k}}). \tag{3.8}$$

Upon substituting Eq. (3.8) into Eq. (3.7) and linearisation, the Hamiltonian no longer conserves particle number N. Consequently, one introduces the chemical potential μ to control N, yielding

$$\mathcal{H}_M = \sum_{\vec{k}\sigma} \xi_{\vec{k}} c^{\star}_{\vec{k}\sigma} c_{\vec{k}\sigma} + \sum_{\vec{k}\vec{l}} V_{\vec{k}\vec{l}} (c^{\star}_{\vec{k}\uparrow} c^{\star}_{-\vec{k}\downarrow} b_{\vec{l}} + b^{\star}_{\vec{k}} c_{-\vec{l}\downarrow} c_{\vec{l}\uparrow} - b^{\star}_{\vec{k}} b_{\vec{l}}), \tag{3.9}$$

with $\xi_{\vec{k}} = \epsilon_{\vec{k}} - \mu$. By defining

$$\Delta_k = -\sum_{\vec{l}} V_{\vec{k}\vec{l}} b_{\vec{l}}, \tag{3.10}$$

which will later turn out to be the quasi-particle energy gap, one can rewrite Eq. (3.9) as

$$\mathcal{H}_M = \sum_{\vec{k}\sigma} \xi_{\vec{k}} c^{\star}_{\vec{k}\sigma} c_{\vec{k}\sigma} - \sum_{\vec{k}} (\Delta_{\vec{k}} c^{\star}_{\vec{k}\uparrow} c^{\star}_{-\vec{k}\downarrow} + \Delta^{\star}_{\vec{k}} c_{-\vec{k}\downarrow} c_{\vec{k}\uparrow} - \Delta_{\vec{k}} b^{\star}_{\vec{k}}). \tag{3.11}$$

An appropriate canonical transformation for diagonalising this Hamiltonian, as found by Bogoliubov and Valatin, is

$$
\begin{pmatrix} c_{\vec{k}\uparrow} \\ c^{\star}_{-\vec{k}\downarrow} \end{pmatrix} = \begin{pmatrix} u^{\star}_{\vec{k}} & v_{\vec{k}} \\ -v^{\star}_{\vec{k}} & u_{\vec{k}} \end{pmatrix} \begin{pmatrix} \gamma_{\vec{k}0} \\ \gamma^{\star}_{\vec{k}1} \end{pmatrix},
\tag{3.12}
$$

where $\gamma_{\vec{k}0}$, $\gamma^{\star}_{\vec{k}1}$ are fermion excitations decreasing the system momentum by $\vec{k}$. The Hamiltonian, which is obtained upon substituting Eq. (3.12) into Eq. (3.11), has a physically relevant solution when constant terms and terms proportional to the occupation numbers $\gamma^{\star}_{\vec{k}}\gamma_{\vec{k}}$ exist exclusively. By setting all other terms to zero, one obtains the condition

$$
2\xi_{\vec{k}}u_{\vec{k}}v_{\vec{k}} + \Delta^{\star}_{\vec{k}}v^2_{\vec{k}} - \Delta_{\vec{k}}u^2_{\vec{k}} = 0,
\tag{3.13}
$$

which allows to determine the coefficients

$$
|v_{\vec{k}}|^2 = 1 - |u_{\vec{k}}|^2 = \frac{1}{2}\left(1 - \frac{\xi_{\vec{k}}}{E_{\vec{k}}}\right).
\tag{3.14}
$$

Thus, Eq. (3.11) reduces to

$$
\mathcal{H}_M = \sum_{\vec{k}}(\xi_{\vec{k}} - E_{\vec{k}} + \Delta_{\vec{k}}b^{\star}_{\vec{k}}) + \sum_{\vec{k}} E_{\vec{k}}(\gamma^{\star}_{\vec{k}0}\gamma_{\vec{k}0} + \gamma^{\star}_{\vec{k}1}\gamma_{\vec{k}1}),
\tag{3.15}
$$

where

$$
E_{\vec{k}} = (\xi^2_{\vec{k}} + |\Delta_{\vec{k}}|^2)^{1/2}
\tag{3.16}
$$

is identified with the excitation energy of a fermion quasi-particle excitation $\gamma_{\vec{k}}$. It turns out that $\Delta_{\vec{k}}$ is well approximated by a temperature dependent, but $\vec{k}$-independent parameter, the minimum energy which is necessary to excite a quasi-particle.

The probability of such excitations in thermal equilibrium at $T > 0$ are described by the Fermi function $f(E_{\vec{k}})$. Rewriting the right side of Eq. (3.10) in terms of $\gamma_{\vec{k}}$ and substituting with $f(E_{\vec{k}})$ yields

$$
\Delta(T) = -\sum_{\vec{k}} V \frac{\Delta(T)}{2E_{\vec{k}}}\tanh\frac{\beta E_{\vec{k}}}{2},
\tag{3.17}
$$

where $\beta = 1/k_B T$. From this expression the temperature dependence of the superconducting gap $\Delta(T)$ can be computed numerically. For practical reasons I have used the closed expression

$$
\Delta(T) = \Delta(0)\cos^{1/2}\left(\frac{\pi}{2}\left(\frac{T}{T_C}\right)^2\right)
\tag{3.18}
$$

in my calculations, which is a good approximation to the BCS result as shown in Fig. 3.6.
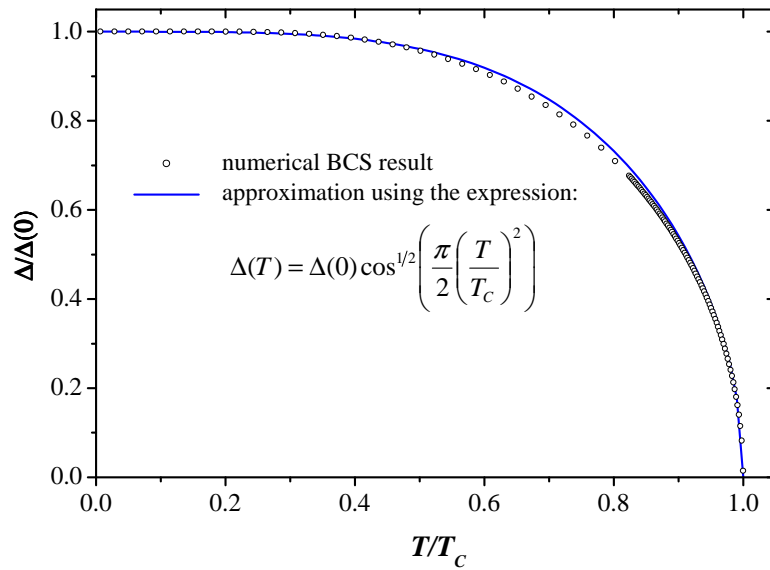
Figure 3.6:   *Comparison between the BCS temperature dependence of the superconducting energy gap and its approximation as a closed expression.*

3.2.2   BTK theory of transparent normal metal/BCS superconductor junctions

The BTK theory has been developed to deal with the phenomena occurring in the ballistic regime of coherent transport across a normal metal/BCS superconductor junction. The authors have worked out a unified treatment which embraces all the range from classic tunnel junctions (high barrier) to barrierless contacts. An essential result of their approach is the computation of the I-V characteristics as determined solely by the dimensionless barrier strength Z. This generalised yet simple model provides the theoretical basis for a variety of experimental studies. More elaborate models on the contrary often fail due to the inaccessibility of a number of parameters depending on the material properties as well as details of the experimental setup. For example, in the analysis of ferromagnet/superconductor junctions by Žutić and Valls [81] detailed knowledge on the investigated system with concern to variables such as incident angles or Fermi surface mismatch are required.

The basic idea of Blonder, Tinkham and Klapwijk was to employ the Bogoliubov equations at the N/S interface. With this ansatz the solutions for incident, transmitted and reflected particles can be identified with the BCS quasiparticle excitations if energies E larger than the superconducting gap Δ are considered. By inserting

$$\xi_k = \frac{\hbar^2 k^2}{2m} - \mu \tag{3.19}$$

into Eq. (3.16), the relevant states are obtained. As only the square of k and ξ_k enter into the expression for E_k, the four states characterised by

$$\hbar k^{\pm} = \pm(2m)^{1/2}[\mu \pm (E_k^2 - \Delta^2)^{1/2}]^{1/2} \tag{3.20}$$

are degenerate in energy. While the elementary quasi-particle excitations γ_k change the system charge by a fractional value, physically relevant excitations have to conserve it. Therefore it is useful to introduce operators, which create excitations and change the charge by $\pm e$. The respective electron and hole operators, using the Bogoliubov transformation have the form

$$\begin{aligned} \gamma_{ek0}^{\star} &= u_k c_{k\uparrow}^{\star} - v_k S^{\star} c_{-k\downarrow}, \\ \gamma_{hk0}^{\star} &= u_k S c_{k\uparrow}^{\star} - v_k c_{-k\downarrow}, \end{aligned} \tag{3.21}$$

where $S^{\star}(S)$ creates (destroys) a Cooper pair. The other three sets corresponding to the degenerate quasiparticle states can be obtained by using the complementary BCS operators $\gamma_{ek1}^{\star}$ and $\gamma_{hk1}^{\star}$ as well as including both signs of k. In the case of fermion excitations such as these the energy of a system with N electrons can be written as

$$E = E_G + \sum_k E_k \gamma_k^{\star} \gamma_k + \mu N, \tag{3.22}$$

where E_G is the ground-state energy and k absorbs all quantum numbers. Consequently the required energy for an excitation changing the charge of the system by $\pm e$ amounts to $E_{ek} = \mu + E_k$ and $E_{hk} = -\mu + E_k$, respectively.

Considering the allowed transitions between two subsystems under the condition of charge conservation leaves us with four processes, listed in table 3.1 for which the respective energy conservation criteria can be easily deduced from above.

Table 3.1: *Allowed processes of charge transfer between two subsystems.*

Process	Energy condition
1. Electron from $1 \to 2$ (or reverse)	$\mu_1 + E_{k1} = \mu_2 + E_{k2}$
2. Hole from $1 \to 2$ (or reverse)	$\mu_1 - E_{k1} = \mu_2 - E_{k2}$
3. Create electron in 1 and hole in 2 (or destroy both)	$\mu_1 + E_{k1} = \mu_2 - E_{k2}$
4. Create hole in 1 and electron in 2 (or destroy both)	$\mu_1 - E_{k1} = \mu_2 + E_{k2}$

Taking into account that an electron incident from the left will either be transmitted with positive or reflected with negative group velocity $dE/d\hbar k$, a schematic diagram of energy versus momentum as shown in Fig. 3.7 can be drawn. The left side of this diagram, representing the normal state, is obtained for $\Delta \to 0$

considering that electronlike excitations cannot be made inside the Fermi surface, as there are no free states in the ground state while holelike excitations are allowed only there.
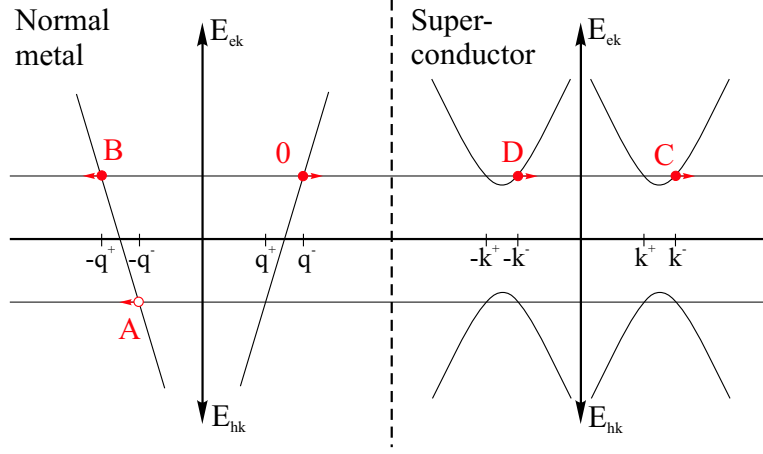
Figure 3.7:   *Schematic diagram of transfer processes at the N-S interface.*

The incident electron in the state labelled 0 has finite probabilities $C(E)$ and $D(E)$ for transmission without and with crossing through the Fermi surface. $A(E)$ and $B(E)$ are the probabilities for the Andreev reflection and ordinary reflection processes. By matching the slope and magnitude of the wave function at the interface, the coefficients A, B, C and D can be determined.

In order to include the basic influence of scattering, a delta function potential $H\delta(x)$ located at the N-S interface is added, while the microscopic details arising from a variety of possible contributions, such as a Fermi surface mismatch, an interfacial oxide layer or disorder in the contact region, are neglected. Now the Bogoliubov equations employing the discussed boundary conditions can be used to calculate the values of A, B, C and D. The results, as listed in Table 3.2, are subdivided into two energy regimes, namely $E < \Delta$ and $E > \Delta$. Additionally, they have been simplified by the introduction of the dimensionless barrier strength $Z = H/\hbar v_f$ and u_0, v_0, the energy dependent BCS coherence factors.

Table 3.2:   *Calculated BTK transmission and reflection coefficients with* $\gamma^2 = [u_0^2 + Z^2(u_0^2 - v_0^2)]$, $u_0^2 = 1 - v_0^2 = \frac{1}{2}\left\{1 + [(E^2 - \Delta^2)/E^2]^{1/2}\right\}$.

	A	B	C	D
$\|E\| < \Delta$	$\dfrac{\Delta^2}{E^2+(\Delta^2-E^2)(1+2Z^2)^2}$	$1 - A$	0	0
$\|E\| > \Delta$	$\dfrac{u_0^2 v_0^2}{\gamma^2}$	$\dfrac{(u_0^2-v_0^2)^2 Z^2(1+Z^2)}{\gamma^2}$	$\dfrac{u_0^2(u_0^2-v_0^2)^2(1+Z^2)}{\gamma^2}$	$\dfrac{v_0^2(u_0^2-v_0^2)^2 Z^2}{\gamma^2}$

In the approximation of ballistic transport across the junction it can be assumed that the incoming particle distribution is given by the equilibrium Fermi function which is simply shifted by eV when an external voltage V is applied. Consequently the incoming and outgoing populations, $f_\rightarrow(E)$ and $f_\leftarrow(E)$, read

$$
\begin{aligned}
f_\rightarrow(E) &= f_0(E - eV), \\
f_\leftarrow(E) &= A(E)\left[1 - f_\rightarrow(-E)\right] + B(E)f_\rightarrow(E) + \left[C(E) + D(E)\right]f_0(E).
\end{aligned}
\tag{3.23}
$$

Since the relevant energy range eV, which is of the order of the superconducting gap Δ, is much smaller than the bandwidth in the normal metal, the density of states can be well approximated by a constant. Thus, the current across the interface is then determined by

$$
\begin{aligned}
I_{NS} \quad &\propto \quad \int_{-\infty}^{\infty} [f_\rightarrow(E) - f_\leftarrow(E)]dE \\
&\propto \quad \int_{-\infty}^{\infty} (f_0(E - eV) - \{A(E)[1 - f_0(-E + eV)] \\
&\qquad + B(E)f_0(E - eV) + [C(E) + D(E)]f_0(E)\}) \, dE.
\end{aligned}
\tag{3.24}
$$

Equation (3.24) can be simplified by taking advantage of some basic properties of the transmission and reflection probabilities and the Fermi distribution function. The coefficients $C(E) + D(E)$ can be substituted by $1 - A(E) - B(E)$ due to the conservation of probabilities $A + B + C + D = 1$. With the symmetry relation $f_0(-E) = 1 - f_0(E)$ the final form of the current across the interface

$$
I_{NS} \propto \int_{-\infty}^{\infty} [f(E - eV) - f(E)][1 + A(E) - B(E)]dE.
\tag{3.25}
$$

is obtained. From this results we can easily arrive at the simple picture that was invoked at the beginning of this section. The expression $[1 + A(E) - B(E)]$ reveals that the Andreev reflection contribution $A(E)$ enhances the current whereas the normal reflection reduces it. Then the coefficients in Table 3.2, analysed in terms of an ideal transparent interface, i. e. $Z = 0$, lead to a doubling of the current for energy values inside the superconducting gap as expected. With the introduction of an effective barrier Z the Andreev coefficient A is reduced and the normal scattering increases. Outside the gap region A decays as the BCS coherence factor v_0 vanishes which makes the situation more complicated in the vicinity of Δ. For high voltages though, the normal state conductance is found.

To include a transport spin polarisation, the model has been extended by separating the current in an unpolarised I_u and fully polarised part I_p for which

the Andreev reflection probability A is set to zero [73, 87]. The ordinary reflection parameter B for the polarised current is thereby changed due to a renormalisation of the probabilities. Strictly speaking, this extension of the model is not correct, since the assumption of $A = 0$ is only true for the subgap region. As pointed out by Mazin *et al.* [88] evanescent Andreev reflection changes the transparency of the interface for energies slightly above the gap.

3.2.3 Mazins generalisation of the BTK approach

Mazin *et al.* generalised the BTK approach to deal with a spin polarised metal/ BCS superconductor junction including the evanescent Andreev reflection amplitude in their calculations. In addition they extended the model from the ballistic to the diffusive transport regime by the introduction of a diffusive region larger than the electronic mean free path, which separates the two sides of the N/S-contact in addition to the interface [88].

As a common starting point for treating contacts in the ballistic as well as diffusive limit, Mazin *et. al.* reproduce the respective conductivities in the "mesoscopic" picture where each electron channel has a conductance of $G_0 = \frac{e^2}{h}$ while N_{cc} conduction channels, characterised by the quasimomentum in the interface plane $\vec{k}_\parallel$, contribute. It is important to note that in the diffusive case each conduction channel has a finite probability for an electron to pass through.

Based on the findings of Beenakker [89], who succeeded in expressing the probability of the Andreev process in terms of the normal state transparency, the BTK current Eq. (3.25), can be reformulated

$$I_{NS} = \frac{e^2}{h} \sum_\kappa T_S(\kappa) = \frac{e^2}{h} \sum_\kappa (1 + A_\kappa - B_\kappa), \tag{3.26}$$

where the summation is over the states $\kappa = \{\vec{k}_\parallel, i, \sigma\}$ with band index i and electron spin σ. For $E < \Delta$ the transmission coefficient T_S, expressed in terms of the normal state transparency T_N is

$$T_S = 2T_N^2 (1 + \beta^2) / [\beta^2 T_N^2 + (2 - T_N)^2], \tag{3.27}$$

with the coherence factor $\beta = V / \sqrt{|\Delta^2 - V^2|}$. In the special case of a specular barrier the normal state transparency is simply given by $T_N = 1/(1+Z^2)$. A short calculation shows that Eq. (3.27) then becomes identical to the BTK formula, as expected.

In order to solve the problem for half-metallic conduction channels, Mazin *et. al.* considered the reflected state of an incoming plane wave to be a combination of a plane wave and an evanescent wave, in contrast to previous approaches. For the

differential conductance dI/dV at $eV > \Delta$ carried by the spin polarised current fraction they get

$$G_{HS} \propto \frac{4\beta}{(1+\beta)^2 + 4Z^2}. \tag{3.28}$$

It is important to note that this solution differs from the result obtained by a simple renormalisation of the normal current above the gap.

The diffusive limit is modelled by an additional diffusive region with transmittance t. Accordingly, the normal state transmittance T_N, which was used to express the probability of the Andreev reflection process in the ballistic case, has to be replaced by $\tilde{T}_N$ with

$$\frac{1}{\tilde{T}_N} - 1 = (\frac{1}{T_N} - 1) + (\frac{1}{t} - 1) = Z^2 + \frac{1}{t}. \tag{3.29}$$

Equation (3.26) then transforms to

$$I_{NS} = \frac{e^2}{h} \sum_{\vec{k}_\parallel, i} \frac{4\tilde{T}_N^2(\kappa)(1 + \beta^2)}{\beta^2 \tilde{T}_N^2(\kappa) + [2 - \tilde{T}_N(\kappa)]^2}. \tag{3.30}$$

The distribution of t is chosen as to reproduce the Bloch-Boltzmann conductivity $\sigma = \frac{e^2}{h} \langle N v_x^2 \rangle \tau$ while taking into account Ohm's law and the normalisation criterion. After some calculation the following differential conductance is obtained

$$\begin{aligned} G_{NS} &\propto \int_0^\infty \frac{1 + \beta^2 dy}{\beta^2 + (2Z^2 + \cosh y)^2} \\ &\propto \frac{1 + \beta^2}{\beta} \mathrm{Im}[\mathrm{F}(-\mathrm{i}\beta) - \mathrm{F}(\mathrm{i}\beta)], \end{aligned} \tag{3.31}$$

with

$$F(s) = \cosh^{-1}(2Z^2 + s)/\sqrt{(2Z^2 + s)^2 - 1} \ . \tag{3.32}$$

For the half-metallic conduction channels in the diffusive regime the differential conductance is

$$\begin{aligned} G_{NS} &\propto \int_0^\infty \frac{2\beta dy}{(\beta + 1)^2 + 2(2Z^2 - 1 + \cosh y)} \\ &\propto \beta F[(\beta + 1)^2/2 - 1]. \end{aligned} \tag{3.33}$$

In summary the coefficient sets for the ballistic and diffusive regime are listed in table 3.3.

Table 3.3: *Normalised differential conductance at $T = 0$ in different regimes by Mazin et al. [88] with: $F(s) = cosh^{-1} \frac{2Z^2+s}{\sqrt{(2Z^2+s)^2-1}}$ and $\beta = \frac{V}{\sqrt{|\Delta^2-V^2|}}$.*

	$\lvert E \rvert < \Delta$	$\lvert E \rvert > \Delta$
ballistic unpolarised	$\dfrac{2(1+\beta^2)}{\beta^2 + (1+2Z^2)^2}$	$\dfrac{2\beta}{1+\beta+2Z^2}$
ballistic polarised	0	$\dfrac{4\beta}{(1+\beta)^2 + 4Z^2}$
diffusive unpolarised	$\dfrac{1+\beta^2}{\beta}\mathrm{Im}[F(-i\beta) - F(i\beta)]$	$2\beta F(\beta)$
diffusive polarised	0	$\beta F[(1+\beta)^2/2 - 1]$

3.2.4   MATLAB simulation with the Mazin model

The Mazin approach constitutes the basis of our simulation model which was established using the MATLAB® software [90]. By varying the values of spin polarisation P and barrier strength Z different spectra can be simulated and compared with the experimental results, if desired.

Before going into the details of the simulation routine, I want to point out some main features of the simulated spectra and discuss the differences arising from the transport regime. Though the temperature influence will be of vital importance for comparing simulation and experiment, I will start this discussion with a set of conductance curves at $T = 0$, as the temperature smearing obscures the typical features of the spectra.

In Fig. 3.8 the normalised differential conductance in the ballistic regime with four different parameter choices is shown. For $Z = 0$ and $P = 0$ we get a doubling of the conductance in the gap region as previously discussed. Consistent with our expectations a tunnelling spectrum results for large Z, which is characterised by a divergent conductivity peak at the gap energy. Introducing a spin polarisation dramatically changes the dI/dV characteristics for transparent junctions and leads to a full suppression of the conduction for $Z = 0$ and $E < \Delta$ as motivated in Fig. 3.5. In the high barrier limit no change is observed upon the introduction of a spin polarisation. It should be noted that the continuous crossover for $Z = 0$ at energies just above the gap is a consequence of the evanescent Andreev mode introduced by Mazin *et. al.* When this contribution is omitted a jump in the conductance curve results.

Simulations in the diffusive limit are shown in Fig. 3.9. The most obvious difference to the ballistic case appears for a transparent contact with $P = 0$ in the sub-gap region. An electron approaching the contact from the normal metal
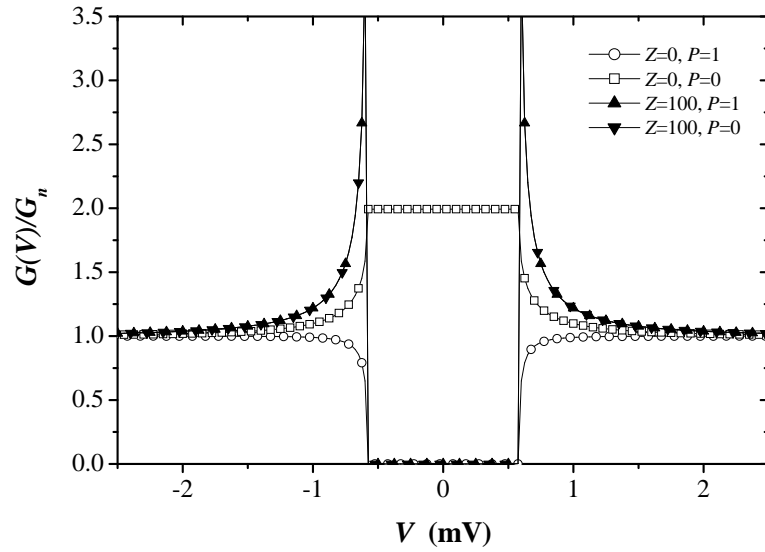
Figure 3.8: *Calculated normalised conductance at $T = 0$ using the model for ballistic transport with Mazins approach [88] for the fully spin polarised conduction channel. The gap value $\Delta = 0.58$ of tin is used and different combinations for the two free parameters Z and P are presented.*
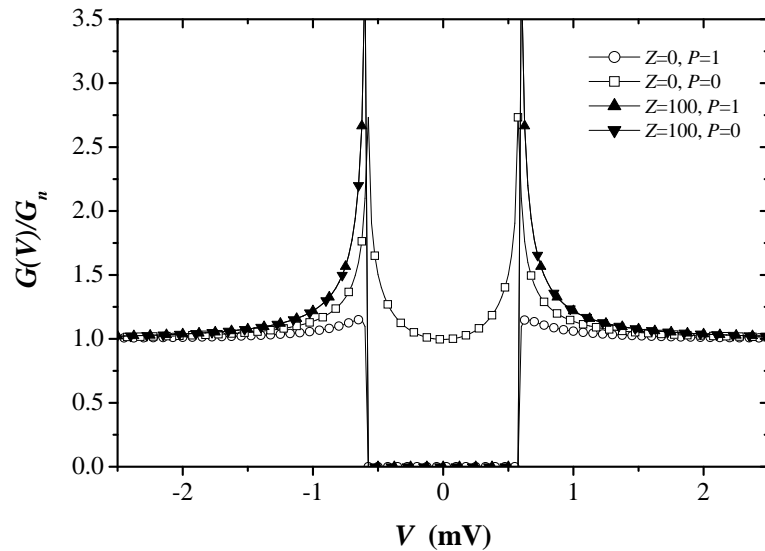
Figure 3.9: *Calculated normalised conductance at $T = 0$ using the model for diffusive transport.*

side will enter the superconductor as a Cooper pair but may diffuse back thereby reducing the conductance at small energy values. The resulting spectrum could be mistaken for a ballistic one with $Z \approx 0.55$ according to Mazin, and Woods *et. al.* [91] show that this ambiguity exists for a whole range of parameter settings. Nevertheless the effect of Andreev reflection suppression at high polarisation values can be clearly distinguished from the influence of a barrier as the resulting spectrum for $Z = 0$, $P = 1$ in Fig. 3.9 demonstrates. Thus studying transparent

metal/superconductor junctions in the ballistic **or** diffusive regime should in theory be a decisive method for evaluating the transport spin polarisation of a wide variety of materials and sample textures. To what extent these theoretical expectations are confirmed and which restrictions are encountered in practice need to be clarified. We will address these issues in the discussion of our experimental results including a detailed analysis of the spectral features with respect to the influence of a finite temperature and heating effects.

For the moment I want to come back to the realisation of our simulation routine based on MATLAB. In the basic implementation of the Mazin model four parameters, namely P and Z as variables, the superconducting gap Δ and the temperature T which are fixed quantities, enter into the calculation. To introduce finite temperatures in our simulation model a numerical integration of the transmission coefficient T_S taken from table 3.3 convoluted with the respective Fermi-Dirac distribution, which is shifted by the external voltage V, has to be performed. As the derivative of the Fermi distribution is no longer described by a delta function, the differential conductance is given by

$$G(V) = \int \frac{df(E,V)}{dV} T_S dE. \tag{3.34}$$

For evaluating this integral the stepsize ΔE of the integration variable E was set to about 0.2% of its maximum value. In turn the numerical integration is replaced by a summation which is carried out by multiplying two vectors. The elements of these vectors are the derivative of the Fermi distribution and the transmission coefficients at energy values spanning the integration range, while the respective cutoff values have to exceed the voltage range. The output of this calculation yields one data point of the differential conductance at the respective voltage V. To get the whole spectrum this expression is computed repeatedly for discrete values $V \pm \Delta V$ within the relevant voltage range from $-V_{max}$ to V_{max}. V_{max} is usually several millivolts and $\Delta V \approx \Delta E$. Finally the obtained values are normalised $G_N = G(V_{max})$.

The code of the simulation routine modelling a ballistic junction is provided as an example in appendix A.1. I would like to emphasise, that whether the calculation is done using the ballistic or diffusive model only depends on the set of transmission coefficients which are used in Eq. (3.34).

In several cases the experimental data is poorly reproduced unless a serial resistance R_s and a parallel conduction path G_p, which do not contribute to the I-V anomalies, are introduced [83, 84]. The latter is included in the simulation procedure by adding G_p to the calculated differential conductance dI/dV. The serial resistance accounts for some voltage drop, which does not occur at the junction. Thus, the simulation variable V has to be substituted by $V + I \cdot R_s$.

In our analysis we are taking it one step further by assuming that this ohmic background should be related to a fraction of thermal transport. In consequence one has to take into consideration that the dissipation of energy in the contact region will cause local heating. For the problem of RI^2 heat that is generated by a current in the constriction a classical theory has been developed by Holm [92] which is valid in the limit of thermal transport. It can be used in the present case to calculate the effective temperature in a steady state at the contact region assuming that a fraction of the voltage drop $U = xV$ at the junction has to be associated with inelastically scattered electrons. According to Holm the effective temperature is given by

$$T_{eff} = \sqrt{T_0^2 + \frac{U^2}{4L}} \qquad (3.35)$$

where the Lorentz number L determines the heat conduction. The simulation routine is then modified by replacing the temperature measured far away from the contact $T_0 = T(V = 0)$ by the voltage dependent temperature T_{eff} according to Eq. (3.35). Thus an individual temperature is assigned to each measurement point of the spectrum. Moreover, the reduction of the superconducting gap, associated with T_{eff}, is modelled according to the BCS temperature dependence in Eq. (3.18).

These extensions have been introduced to the diffusive model in order to deal with junctions where the bad metallicity of the probe material may lead to a situation were diffusive as well as thermal transport appears. In appendix A.1 the respective MATLAB routine is reproduced.

3.3 Experimental setup and test measurements

3.3.1 Experimental setup for point contact Andreev reflection studies

The suppression of Andreev reflection in point contacts was studied between a superconducting tip and metallic bulk as well as thin film samples. To achieve high stability in a temperature range of a few Kelvins, the samples were immersed in a liquid helium bath, while its temperature was controlled by decreasing and increasing the vapour pressure. For establishing the contacts a lever mechanism initially developed for the study of break junctions was employed. Its original design has been broadly described in Ref. [93]. To carry the superconducting wire in place of the breaking edge, the sample holder was slightly modified. In Figs. 3.10 and 3.11 the low temperature inset and zoomed views of the fine approach mechanism and sample section are shown.

Tip and sample were brought into contact at 4.2 K while checking the junction resistance with a probe current of a few μA. Once a stable contact with resistance
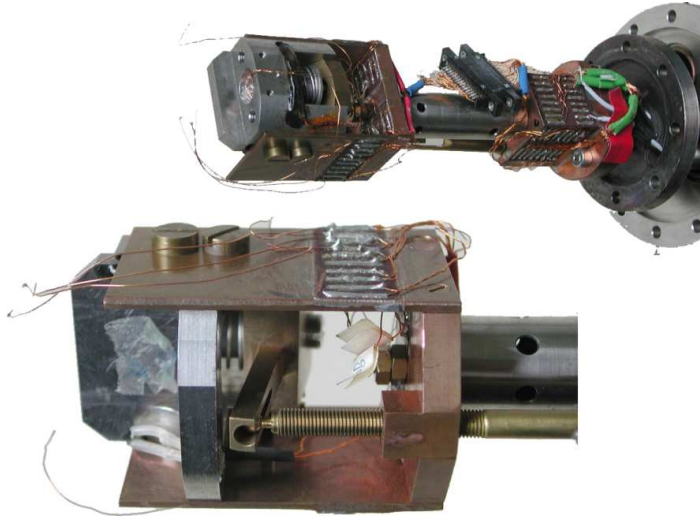
Figure 3.10: *Low temperature inset for PCAR measurements. In the lower part the lever mechanism driven by a micrometer screw is enlarged.*
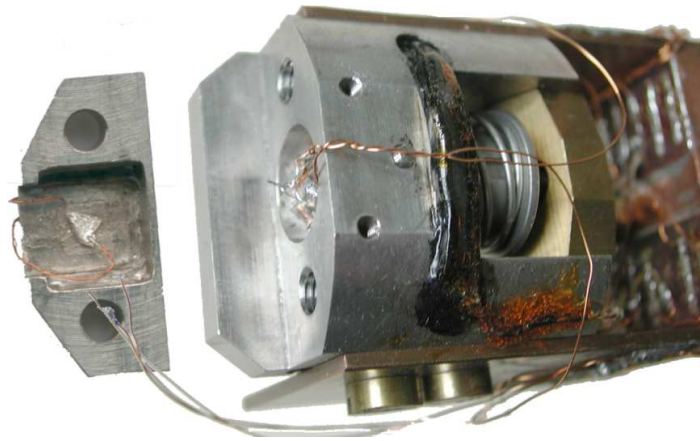
Figure 3.11: *Sample section of PCAR inset before the sample is mounted. For rough tuning of the sample-tip distance the tin wire is mounted on a slide which can be adjusted with a screw on its backside.*

between 1 and 100 Ω is established, the helium reservoir is evacuated. At reaching a temperature of 1.6 K the pump is turned off and the measurement is launched. By standard 4-probe method I and V across the junction were measured. The differential conductance dI/dV was determined directly by ac lock-in technique at a frequency of 1.7 kHz and a modulation current equal to the stepwidth. Typically the stepwidth was chosen such that voltage steps of about 0.1 mV resulted. For current driven measurements a series resistance R much larger than the contact resistance was used to convert the voltage output of the lock-in to a current output. The spectra were recorded continuously while the temperature increased slowly from 1.6 to 4.2 K at a rate of approx. 0.025 K/min. In Fig. 3.12 the basic measurement components and their setup are shown.
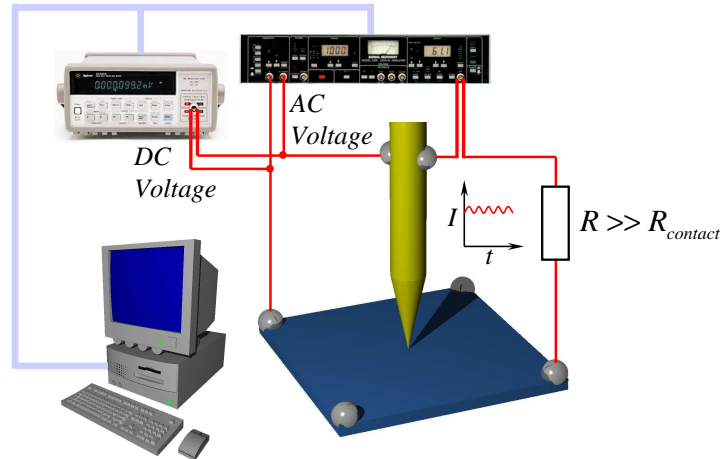
Figure 3.12:　*Point contact Andreev reflection measurement setup. The measurements are current driven with a modulated input from the lock-in amplifier. The AC output voltage of the junction is analysed by the lock-in amplifier and a nano-voltmeter is used to record the DC contribution. This allows to determine the I-V characteristics of the junction and its conductance independently and with highest possible accuracy.*

First test measurements were performed using lead and niobium junctions as described below. For the investigation of metallic Sr_2FeMoO_6 thin films and polycrystalline $Co_2Cr_{0.6}Fe_{0.4}Al$ a tin probe was employed. Using this material has the advantage that the measurement range exceeds its superconducting ordering temperature of $T_C = 3.7$ K, while keeping the samples immersed in liquid He. The possibility to measure the contact in the superconducting as well as normal conducting state of the tip allows to verify the causal relationship between the superconducting phase transition and the appearance of the *I-V* anomalies as visible in Figs 3.15 and 3.18.

3.3.2　Test measurements on Cu-Pb junctions

The proper functioning of the equipment was checked with test measurements of Cu-Pb and Cu-Nb junctions. High purity bulk samples of copper were used to ensure that ballistic contacts are obtained while the voltage drop takes place solely at the junction, meaning that the potential difference between the two probes on the sample surface is negligible. Fig. 3.13 represents the typical spectra which have been measured reproducibly.

As expected the obtained spectra can be well understood in the ballistic model assuming zero spin polarisation. A doubling of the conductance for small enough voltages is not achieved due to a barrier parameter of $Z = 0.31$ and a significant temperature smearing at 4.2 K. The barrier parameter Z varies from contact to contact, yet a small contribution is present in all measurements. This behaviour has been observed in several studies [91, 94, 95], and it is understood that Z can
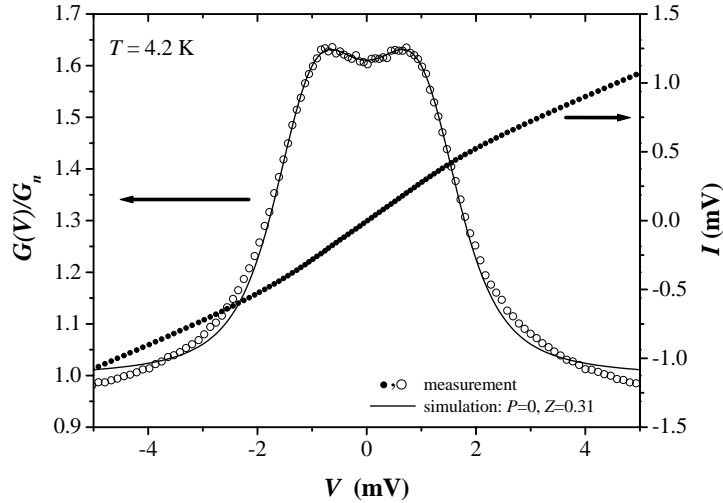
Figure 3.13: *Measurement and simulation of a Cu-Pb contact at 4.2 K. The DC current (right scale) and the normalised differential conductance (left scale) are presented as function of the applied voltage. The simulation of dI/dV is plotted as a line.*

be interpreted as a generalized barrier parameter which is not only determined by the physical barrier between the junction materials but also absorbs the influence of a Fermi surface mismatch. In this case the minimum achievable Z for a series of different contacts is non-zero.

Another consequence of the strong inherent simplifications of the model are the deviations for absolute voltage values much larger than the superconducting gap. While a continuous decrease of the conductance for $|V| > 4$ mV was observed in this work, Upadhyay *et. al.* [74] have seen positive as well as negative deviations from the theory. One might speculate about a number of possible causes. They suggest that the strong coupling effects in lead or the high current density, which can lead to a partial gap suppression, might be the reason. Discrepancies may also arise due to the fact that the junctions are modelled by a single homogeneous contact whereas real contacts are certainly much more sophisticated. It is found that the mechanical size of the contact is much bigger than the electrical one. This may lead to several complications. One can easily imagine to get multiple contacts with different characteristics inducing an additional broadening. Furthermore in case the surrounding material makes a bad contact instead of being completely inactive a background signal may appear. Additionally the dead contact material may disturb the highly sensitive thermal balance by decreasing the coupling of the junction to the helium bath.

With this in mind one can claim to have achieved good agreement between the test setup results and theoretical predictions. On this basis I will now address some recent issues in the investigation of potential half-metallic materials.

3.4 PCAR analysis of potential half-metals with high resistivities

Section 3.3.2 gave a first taste of how the interpretation of PCAR spectra can be complicated by the experimental conditions. Nevertheless one could still be sure that a ballistic contact between the two junction materials was realised. Yet, for the analysis of many complex materials with predicted 100% spin polarisation this assumption has to be abandoned, too.

In order to obtain fully spin polarised conduction electrons, the s-electrons which usually form broad bands have to be caught in localised states leaving behind only the narrow bands formed by the d-orbitals. With an exchange splitting these narrow bands can then be shifted sufficiently to obtain a high density of states for electrons of one spin direction while a gap appears in the other one. Unfortunately the conduction via d-electrons involves a lowering of the carrier mobility and leads to a significant rise of the specific resistivity for these materials.

The described situation is encountered for example in the intermetallic Heusler compound Co_2CrAl. Figure 3.14 illustrates the crystal structure of this material including a schematic representation of its band configuration which was taken from Ref. [96]. On the basis of band structure calculations the composition can be systematically tuned in order to obtain full spin polarisation in conjunction with a van-Hove singularity at the Fermi energy in the majority spin channel [97]. As a most promising candidate for exhibiting half-metallicity $Co_2Fe_{0.6}Cr_{0.4}Al$ (CCFA) has been prepared in bulk form [98] and measured by PCAR.
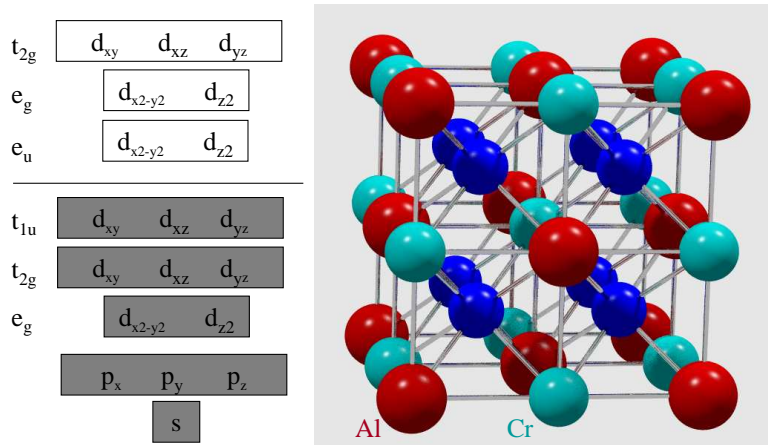
Figure 3.14:   *Crystal structure and band configuration of Co_2CrAl according to Galanakis [96].*

In the perovskite oxides, like the manganites and Sr_2FeMoO_6, charge transport has been identified to be mediated by a double-exchange mechanism as was

discussed in section 1.1.2. In consequence, the specific resistivities are typically several orders of magnitude higher than for 3d metals while the mean free paths are reduced accordingly. Thus, for the investigated Heusler and double-perovskite compounds Wexlers formula (3.3) does not allow a clear-cut predetermination of the transport regime — and this is more a rule than the exception within the respective material classes.

3.4.1 Analysis of Sr_2FeMoO_6-Sn spectra

Figure 3.15 shows a series of PCAR measurements obtained from the same Sr_2FeMoO_6-Sn contact at different temperatures. In accordance with $T_C(\text{Sn}) = 3.7$ K the contact is ohmic at $T = 4.2$ K, indicated by the constant response. As the superconducting gap of tin opens up, a dip in the differential conductance dI/dV appears. This anomaly becomes more pronounced, the lower the temperature. In these measurements the contact resistance was $R_C \approx 25\Omega$. Measurements up to $R_C \approx 250\Omega$ were performed yielding similar results.
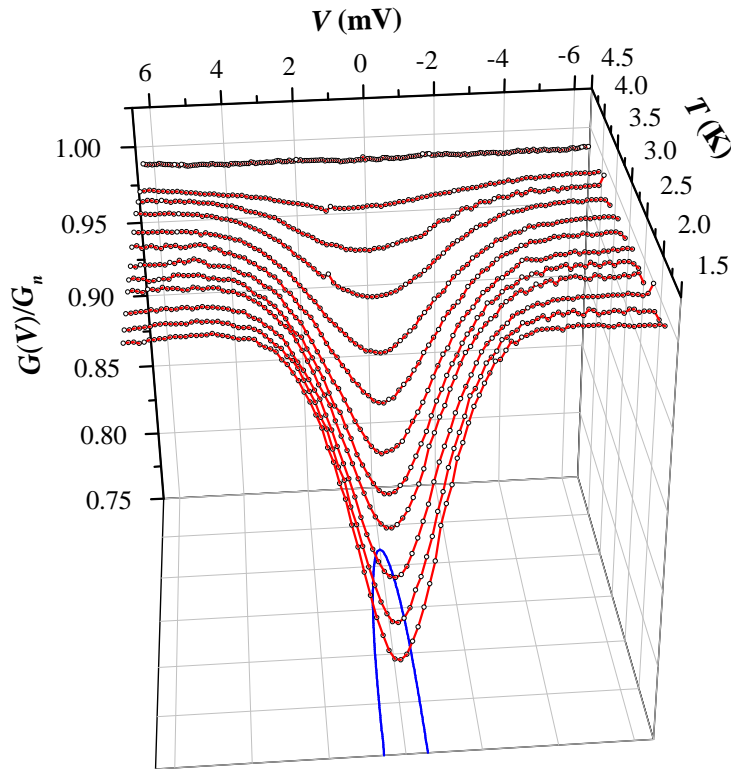
Figure 3.15:   *Measured normalised differential conductance vs. bias voltage for a Sr_2FeMoO_6-Sn contact at different temperatures. The blue curve illustrates the evolution of the superconducting energy gap Δ of Sn.*

As discussed in section 2.1 the typical resistivity range of our samples is 500 $\mu\Omega$cm. From Hall effect measurements [78] the elastic mean free path can be estimated ($l_e \approx 1$ nm) using the one band approximation. Simple arithmetic

reveals that we are far away from the ballistic limit. Therefore any further interpretation of the spectra has to be based on the diffusive model. Whether or not a thermal contribution needs to be taken into account cannot be decided by this simple argument.

In a first approach the purely diffusive model is applied. Simply fitting the depth of the dip in the conductance by adjusting the parameters P and Z does not lead to a satisfying description of the data. In the experimental spectra the anomaly is much wider than the bare energy gap of tin, sketched on the bottom of Fig. 3.15. A serial resistance R_s must be introduced which can attribute for the broadening of the spectra in this approach. In addition a fraction of ohmic response is accounted for by allowing a parallel conductivity G_p that does not contribute to the dI/dV anomalies. By adjusting these two parameters a reasonable approximation of the measured data can be obtained if a high spin polarisation P is assumed. For a measurement at 1.8 K (see Fig. 3.16) the best agreement with the experiment was achieved for $R_s/R_k = 2$, $G_p/G_n = 3.25$, $Z = 0$ and $P = 0.98$, where R_k denotes the contact resistance and G_n the normal state conductivity. In comparison to this a simulation is shown that has been performed with the same correction parameters but for $P = 0$ and a barrier strength $Z = 100$ to match the depth of the minimum. It is clear that in this approach a high transport spin polarisation is needed to fit the data.
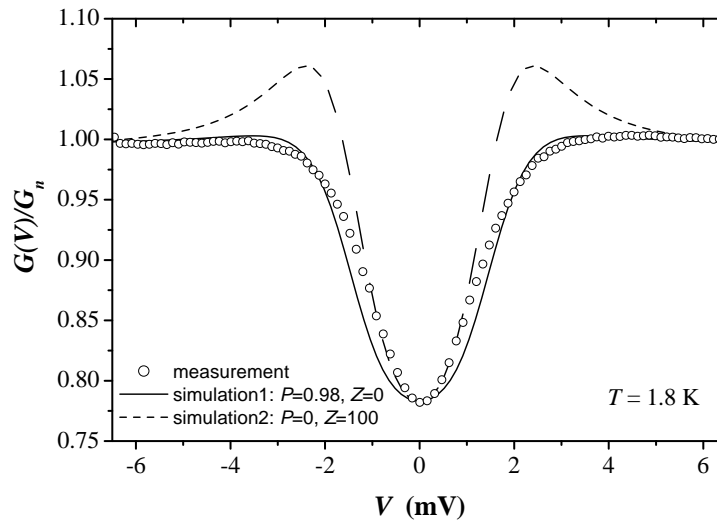
Figure 3.16:   *Experimental data at T=1.8 K. The lines are fits with the diffusive transport model for different values of Z and P as indicated in the figure.*

Yet the vee shape of the measured curves is not reproduced well by the simulation. Interestingly this kind of systematic deviation from the theory has been seen previously in different studies [83, 94, 99]. Generally the effect is strongest for junctions with a rather low contact resistance where high spin polarisation

values are fitted. In an early study by Osofsky *et. al.* [99] $La_{0.67}Ca_{0.33}MnO_3$-Pb and CrO_2-Pb contacts are analysed. In the junctions with CrO_2, which has a ten times smaller residual resistivity compared to $La_{0.67}Ca_{0.33}MnO_3$, the vee shape is much less pronounced. These observations clearly indicate that the diffusive model alone fails for the unfavourable situation of a large contact size, if materials with high residual resistance are studied. Nevertheless a possible contribution of inelastic scattering effects as the ratio between contact size and mean free path increases has been completely ignored up to now. Given the fact that the same problems are faced when studying the highly prized diluted ferromagnetic semiconductors [100], a clarification of the phenomenon is overdue.

For this task our initial idea to include a contribution of thermal transport proves useful. Compared to the simulation routine adopting the purely diffusive model a single parameter, namely the fraction of the voltage drop $U = xV$ which leads to heating in the contact area, is introduced additionally. As shown in Fig. 3.17 a very good agreement between measurement and simulation is achieved, especially the vee shape of the measured curves can be reproduced very well. It should be noted that the effective temperature stays below the superconducting transition temperature within the nonlinear region. As soon as T_C is reached the conductivity returns to the normal state value G_n.
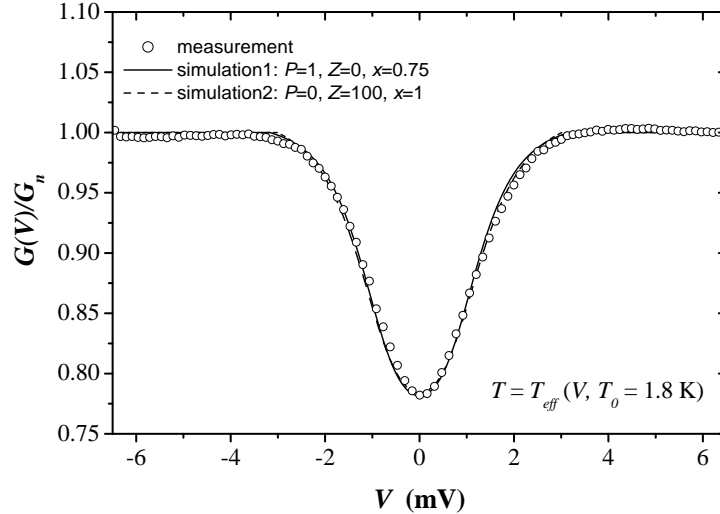
Figure 3.17: *Experimental data at T=1.8 K. The lines are fits with the diffusive transport model that has been extended by the introduction of an effective temperature T_{eff}. The critical temperature $T_{eff} = T_c$ is reached for a voltage of 3.2 mV (3.7 mV) in simulation 1 (simulation 2), i.e. outside the region of nonlinear response.*

According to this approach, the qualitative change in the shape is caused by the heavy temperature smearing of the typical gap structures which becomes more and more important as the bias voltage V is increased. This effect is so

strong that it can lead to a total suppression of the characteristic peaks in the conductivity even for contacts with a large tunnelling contribution, which turn out to be of particular importance for a correct interpretation of the acquired spectra. Figure 3.17 reveals that even the two extreme cases, namely no barrier, full spin polarisation and strong barrier, no spin polarisation are equally suited to describe the data. In view of the simplifications of the model tiny differences between the fits cannot be considered to be decisive. Therefore no conclusion can be drawn about the value of P with this kind of experiment in the case of a highly resistive material such as Sr_2FeMoO_6.

3.4.2 Analysis of $Co_2Cr_{0.6}Fe_{0.4}Al$-Sn spectra

In pressed powder samples, consisting of $Co_2Cr_{0.6}Fe_{0.4}Al$ with 5 to 15 % of Al_2O_3, large negative magnetoresistive effects up to 60 % at room temperature have been observed. Due to the additional features of a high Curie temperature (800 K) and good compatibility with standard semiconductor technology, the intermetallic Heusler compound $Co_2Cr_{0.6}Fe_{0.4}Al$ has been recognised as an interesting candidate for MR applications [97, 98, 101]. Motivated by this discovery, PCAR measurements at a cleaved surface of a bulk polycrystal were performed.

Compared to Sr_2FeMoO_6 the arc-melted polycrystal had a significantly lower resistivity of about $\rho = 90\mu\Omega$cm. In the $Co_2Cr_{0.6}Fe_{0.4}Al$-Sn PCAR experiments the contact resistances varied between 1 and 20 Ω. A typical series of spectra from one contact at variable temperature is presented in Fig. 3.18. In contrast to the previous measurements on Sr_2FeMoO_6 only a small broadening of the spectra is observed. This can be easily seen in Fig. 3.18 by comparing Δ with the position of the conductance maxima. Due to the smaller specific resistivity of the material and supported by the use of a bulk sample this is in accordance with the expectations.

Recalling that the transport regime for these contacts is not well known, the analysis has to be performed for both transport regimes. In a first approach the data is simulated with the ballistic model implying fixed temperatures (as an example see Fig. 3.19). The resulting values, $P = 0.49 \pm 0.01$ and $Z = 0$, are unique as long as only one model is considered. However, it is possible that the assumption of ballistic transport is not justified and heating occurs. In this case the diffusive limit is appropriate. Following the diffusive approach, as discussed in detail for Sr_2FeMoO_6, yields $P = 0.06$ and $Z = 0$ instead (see Fig. 3.20). Thus again the value of the transport spin polarisation depends strongly on the ansatz chosen for simulating the spectra. Since the quality of the simulations is not significantly different in both cases a non-ambiguous determination is not possible.
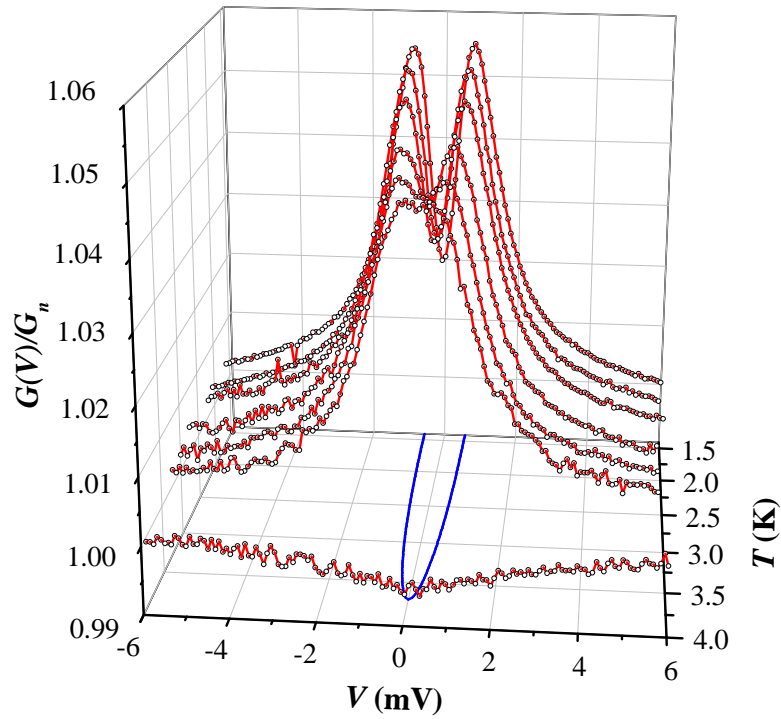
Figure 3.18: *Measured normalised differential conductance vs. bias voltage for a $Co_2Cr_{0.6}Fe_{0.4}Al$-Sn contact at different temperatures. $\Delta(T)$ is plotted as a blue curve.*
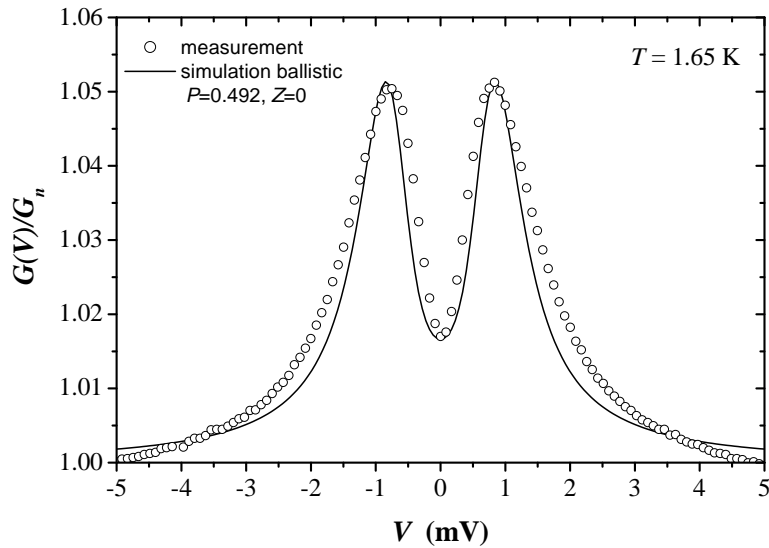
Figure 3.19: *Experimental data at $T=1.65$ K with a simulation in the ballistic limit. A small contribution of parallel conductance $G_p/G_n = 0.1$ and a serial resistance $R_s/R_k = 0.8$ were used to simulate the data.*

Neither the diffusive nor the ballistic result are supporting the theoretically expected half-metallic nature of this material. From the observation of a strong ferromagnetism and a large MR it is clear that the result, which has been obtained
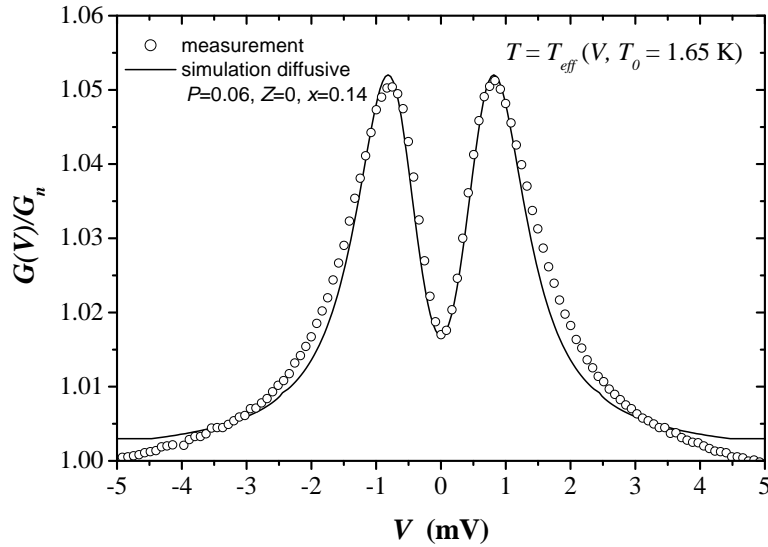
Figure 3.20:   *Experimental data at T=1.65 K with a simulation in the diffusive limit for T_{eff}. The critical temperature $T_{eff} = T_c$ is reached for a voltage of 4.5 mV.*

by the diffusive analysis cannot be correct. This might be judged as an affirmation of the ballistic approach. However, another consequence of the elevated resistivity, or rather the reduced mean free path of the electrons, is the reduction of the information depth. As mentioned in section 3.1.1 a modification of the contact interface, either by a degraded surface layer or a strong deformation due to the penetration of the tip, can destroy the spin polarisation in the relevant sample volume. Recent photoemission studies [102] indicate that a selective oxidation of the Cr at the surface does occur, which is assumed to be the reason for the observed discrepancies.

3.5   Concluding discussion on practical limits of the PCAR method

In order to investigate the transport spin polarisation, point contacts between a superconducting tip and a ferromagnetic material were realised. The observed dI/dV anomalies, commonly attributed solely to coherent transport, have been analysed in a generalised framework where a possible contribution of thermal transport is considered. For the first time the implications of this scenario, especially concerning the determination of P, have been critically discussed.

It has been shown that for the highly resistive material Sr_2FeMoO_6 the spectra are most likely dominated by thermal transport. In this case it is impossible to decide whether the observed dI/dV characteristics are caused by a fraction of coherent transport exhibiting the effect of Andreev reflection suppression or just

the result of a strongly broadened spectrum dominated by electron tunnelling at the effective barrier Z. This result suggests that the same problem will be encountered for any material in the resistivity range of 500 $\mu\Omega$cm or above and constitutes the upper limit where the PCAR method can be applied.

For $Co_2Cr_{0.6}Fe_{0.4}Al$, representing materials with a specific resistivity in the range of 100 $\mu\Omega$cm, the dI/dV anomalies can be clearly attributed to coherent transport. Here the ballistic and diffusive model yield comparable descriptions of the data but the different simulations again lead to incompatible values of the transport spin polarisation. To justify the use of one specific approach further studies are needed, especially with respect to mean free path of the charge carriers and the influence of surface effects, but this is not a principle problem as in the case of Sr_2FeMoO_6.

Convincing experiments, where a non-ambiguous interpretation of the results was achieved, have been carried out on CrO_2 samples [103]. For the investigated thin films a specific resistivity of 10 $\mu\Omega$cm has been found, whereof the authors estimate a mean free path of about 1000Å. This means that the bulk material rather than its surface is probed. A collection of spectra from the work of Ji *et. al.* is shown in Fig. 3.21.
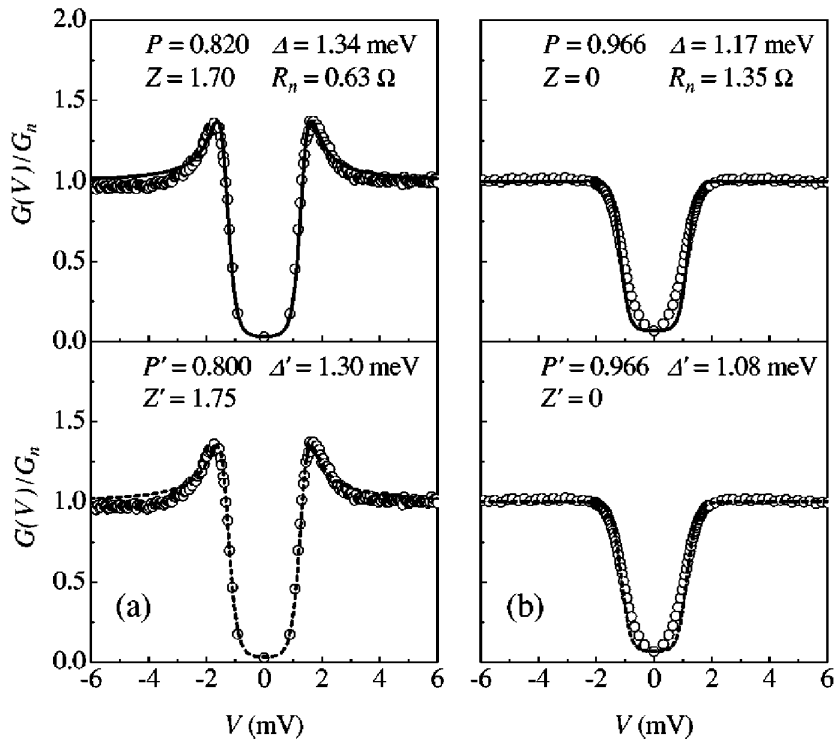
Figure 3.21: *Experimental spectra and analysis of CrO$_2$-Pb point contacts. Two different contacts are analysed once in the ballistic (upper row) and again in the diffusive limit (bottom row). The resulting spin polarisations (P, P′) are nearly identical. Taken from [104].*

All contacts were well described in the ballistic limit and a comparison with the diffusive fits was consistent [104]. Since no background conductivity or broadening of the spectra was observed, heating certainly does not play a role here. Nevertheless, some deviations are still present, which underlines that the real contact behaviour is complex and cannot be fully described by the simplified models of BTK and Mazin.

According to the current progress, PCAR can be regarded as a good method for probing the spin polarisation of materials with a specific resistivity of 10 $\mu\Omega$cm or less. However, the discussion in this thesis shows that the same is not true for materials with higher residual resistivities. In the case of significant inelastic scattering contributions the standard descriptions are oversimplified. By introducing an extended model which accounts for heating in the constriction, the main deviations were eliminated but at the expense of obtaining several equally suited sets of junction parameters, which eventually renders impossible to determine the spin polarisation.

Nanopatterning by Focussed Ion Beam Etching and Electron Beam Lithography

Aiming at the possibility to study new materials in a device-oriented setup of technical relevance, the group's patterning facilities where extended. During the course of this thesis an electron beam lithography (EBL) and a focussed ion beam (FIB) system specified for achieving sub-micrometer structures were put into operation and fully characterised. The issue of general and system specific resolution limits is addressed, which is substantiated by discussing several examples of patterned magnetic media and their physical or technological interest. The required process chains for nanopatterning have been established in this work. They are depicted in detail to allow a subsequent use of the EBL and FIB systems for standard patterning tasks, emphasising the pros and cons of the employed systems.

During the last years a quickly growing number of methods for fabricating structures with submicron dimensions have emerged. While optical lithography has survived all odds for large-scale applications due to enormous technological efforts, a variety of different techniques have become available for basic research and limited-lot production. A wide scale of pattern sizes is covered down to the atomic level, where self assembly is discussed as a future candidate to overcome the limits of present structuring techniques. Though bottom up approaches have gained increasing attention and promising routes of combining self assembled structures with conventional lithography are emerging, the patterning of functional layers such as the magnetoresistive materials relies on top down methods.

Commercially available systems include focussed ion beam, electron beam lithography, nano-imprinting and scanning probe microscopy based equipment,

to mention the most popular ones. Amongst them imprinting techniques have the highest potential to become a serious rival for optical lithography due to a high throughput [2]. EBL and FIB etching/induced deposition, on the other hand, are the most versatile tools for device fabrication on the fundamental research level.

4.1   Basic setup of EBL and FIB systems

The general setup of of EBL and FIB systems is very similar. Their basic units are the so called electron and ion guns. They contain the emission source and the optics which is used to focus and navigate the beam. A simplified schematic drawing of the main components is shown in Fig. 4.1.
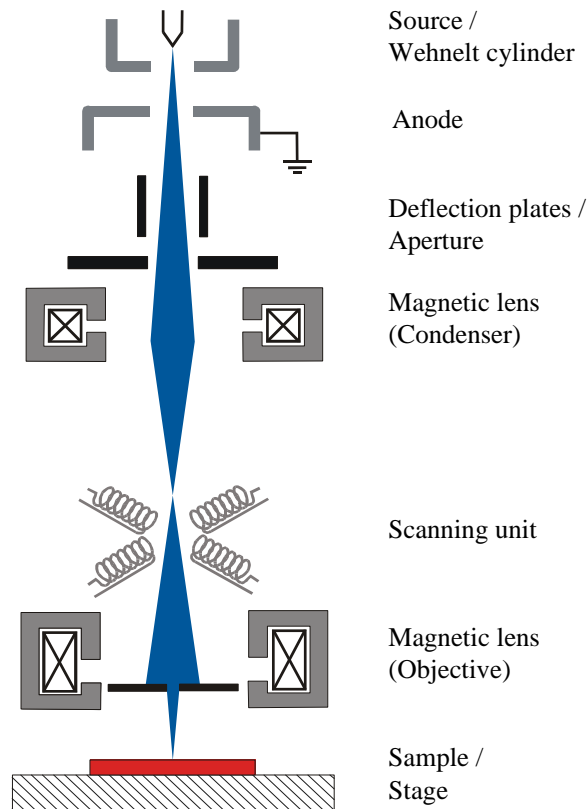
Figure 4.1:   *Basic setup of electron and ion guns. Compared to an electron microscope the beam blanking unit consisting of deflection plates and aperture has been added.*

In order to provide optimum conditions for high resolution nano-fabrication a small beam probe is required. One pre-requisite is the use of emitters with small lateral dimensions. But the advantage of a small emission region has to be balanced against the resulting reduction of the emission current. Therefore field emitters, which have a much larger brightness than thermal emission cathodes, are widely used. Table 4.1 lists the most commonly used electron sources. The ion

sources, which are typically used for FIB applications, are similar to an electron field emission setup, where the tungsten tip is coated with the desired ion species, in most cases gallium. Ion generation is accomplished by a field evaporation mechanism from the tip apex, which is a few nanometre in diameter [105].

Table 4.1: *Some features of electron emission sources. Taken from [106].*

Material	W	LaB_6	ZrO/W	W
Type of Emission	Thermionic	Thermionic	Schottky	Field Emission
Source Size	25 μm	10 μm	20 nm	5 nm
Brightness $(A/cm^2/sr)$	$\approx 10^5$	$\approx 10^6$	$\approx 10^8$	$\approx 10^9$
Current Stability (% per minute)	< 1	< 1	< 1	$2 - 10$
Lifetime	100 hrs.	1000 hrs.	4000 hrs.	3000 hrs.

The emitted particle beam initially passes through the condenser lens where it is demagnified. The field strength of the condenser lens determines the lateral dimensions of the resulting intermediate image as shown in Fig. 4.2. When the probe size decreases the amount of electrons/ions, which do not pass through the final aperture increases, again reducing the net beam current.
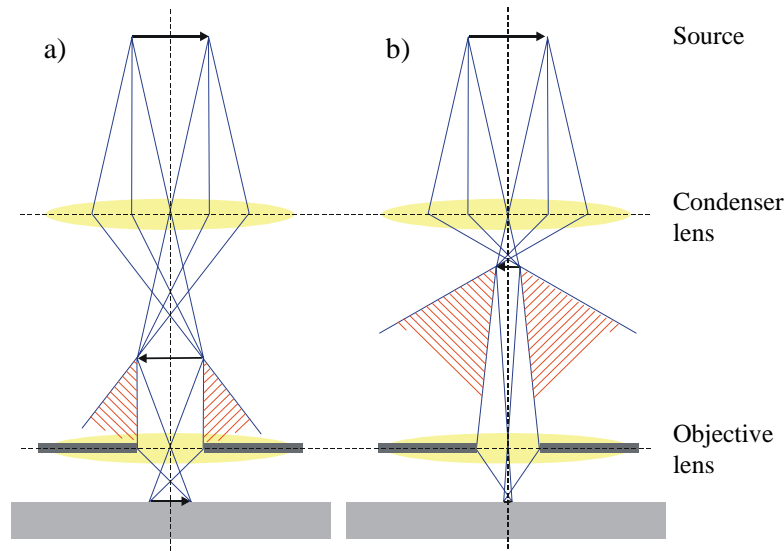
Figure 4.2: *Formation of the electron probe in an SEM. By increasing the strength of the condenser lens magnets, the size of the intermediate image and the total probe current are reduced.*

The objective lens focusses the beam onto the sample. An important parameter is the working distance (WD), i. e. the distance between observed sample surface and the bottom surface of the objective lens. Typically WD can be varied from a few millimetres to 30-40 mm. Since a stronger lens leads to a smaller probe image, the best resolution is achieved for small WD, while the depth of focus improves by choosing longer distances.

In many practical cases, i. e. for small sources and low beam currents, the minimum diameter of the beam spot is mainly determined by the axial aberrations of the optical components. Since magnetic lenses are by far not as perfect as the ones available for light, care has to be taken in order to achieve best possible congruence between beam path and optical axis. Nevertheless imperfections always lead to a noticeable widening of the beam.

By employing stigmator coils in the objective lens it is possible to correct an elliptical beam shape (astigmatism) during operation. For the spherical aberration the aperture size plays an important role. By decreasing its size the deviations resulting from the angle of beam spread are reduced thus improving the image accuracy. It does not, as one might suppose, directly reduce the spot size. Similarly, increasing the acceleration voltage leads to a decrease of the spherical aberration. Additionally, the relative energy spread of the electrons/ions which is the origin of chromatic aberration is reduced. But especially for electrons a change of the acceleration voltage has significant influence also on the penetration depth and the possible interaction processes between probe and sample which will be discussed in section 4.2.2.

So far the discussion is identical for EBL/FIB systems and the respective microscopy tools. Yet lithography applications are somewhat more demanding. While optimum spot sizes in microscopes only needs to be achieved at high magnification, a small beam diameter over the whole magnification range is desirable for FIB and EBL systems since the processable write field size is defined by the magnification value. Consequently these systems should additionally be equipped with an amplifier for the scanning coils exhibiting high signal to noise ratio, which ensures that high resolution can be achieved nearly independent of the magnification settings.

Another special requirement concerns sample positioning. Accurate positioning becomes important when several processing steps are involved or the pattern size exceeds the maximum write field. Consequently many systems are equipped with laser-interference stages which allow a stitching accuracy of about 2 nm and the implementation of a drift correction which monitors the stability of the sample position during processing.

4.2 Electron beam lithography

The potential of using electron beams as lithography tools for micrometer and sub-micrometer patterning was recognized by many workers in the 1960s. But it was only until Hatzakis and co-workers discovered Poly-methyl-methacrylate (PMMA) as a high resolution electron resist that EBL emerged as a technique for small device fabrication [107]. Additionally they introduced the lift-off process which allowed to produce sub-micrometer metal connectors and thus became the key technology for the fabrication of micrometer transistors. The typical sequence of EBL fabrication with a subsequent lift-off process is illustrated in Fig. 4.3.
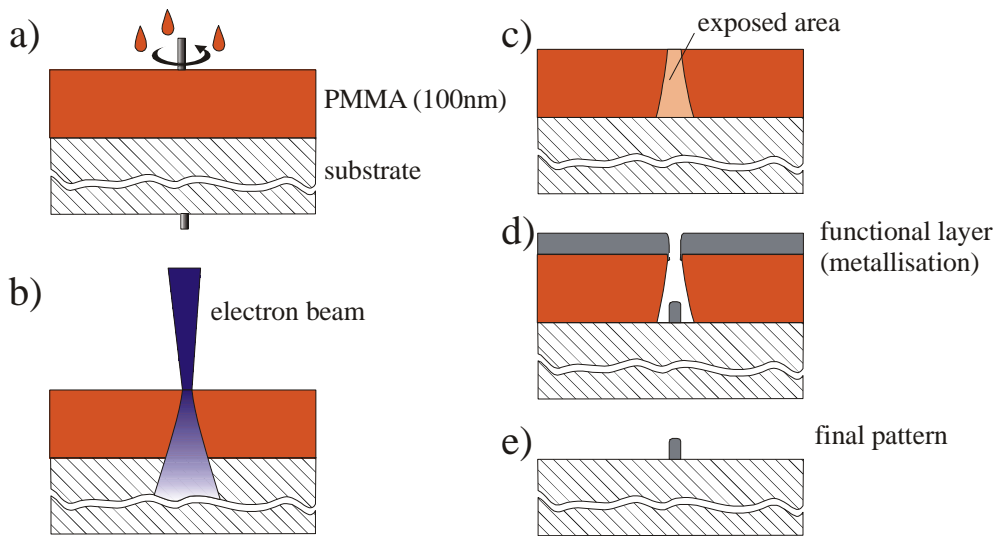
Figure 4.3: *Patterning process by electron beam lithography. (a) The electron sensitive resist material is homogeneously dispersed on the substrate by spin coating. (b,c) The desired structures are defined by electron exposure of the respective sample parts. (c) The exposed areas are developed and removed to create a resist mask. In a metallisation step (d) the whole sample is covered with the functional layer. (e) Using an appropriate solvent the remaining resist is removed.*

4.2.1 The electron resist and pre-exposure steps

The general principle which is exploited in any kind of lithographic resist material is the modification of its solubility by irradiation. Positive tone photoresists, for example, consist of macromolecules which contain certain functional groups. When exposed to light these groups undergo a photochemical reaction. Typically the functional groups are thereby replaced by carboxyl groups, thus making the exposed photoresist soluble in aqueous alkali solutions.

Electron beam resists exploit another mechanism, namely the possibility to alter the size of macromolecules. The effects of ionising radiation on polymers is

twofold. Cross-linking of neighbouring chains and random scission of the chains take place simultaneously, but in individual polymers generally one of the two effects dominates. PMMA, which is still the most commonly used electron resist, degrades upon electron-bombardment as depicted in Fig. 4.4, thus rendering it a positive tone resist.
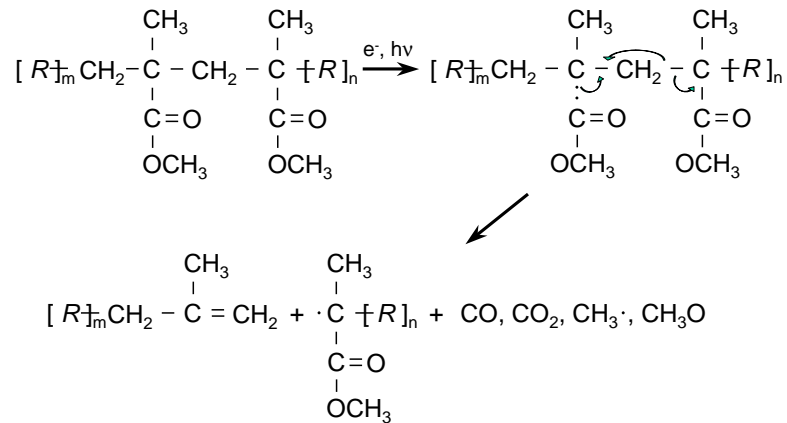
Figure 4.4: *Mechanism of electron radiation induced chain scission in PMMA taking place at a random monomer pair $R_{m+1} - R_{m+2}$. (After Ref. [108])*

To obtain a lithography resist with good contrast nearly monodisperse solutions of the macromolecules are prepared. Development is achieved by using a mixture of two liquids where one is a good solvent for the particular polymer irrespective of its molecular weight and the other is not. For a certain relative amount it is possible to obtain a solvent for the respective polymer below a critical molecular weight.

The EBL patterns, which are presented in this work, were fabricated with the resist system consisting of 2% PMMA 950k in Anisole and Methyl Isobutyl Ketone (MIBK)/Isopropanol (IPA) 1:3 developer. By using polymer chains of high molecular weight, i. e. 950000, in combination with a strongly diluted solvent, high resolution can be achieved at the expense of a low sensitivity. This means that an areal dose of about $50 - 500\mu C/cm^2$ is necessary in order to obtain a residue-free development of the exposed pattern.

The resist material is dispersed on the sample by spin coating. Figure 4.5 clarifies the thickness dependence of the resist film with respect to spin speed and solid content [109]. It is found that the thickness is only weakly dependent on the rotation speed but it can be effectively tuned by changing the solid content of the polymer solution. Yet the absolute value is influenced additionally by the ambient conditions and the sample size. In contrast to the supplier's recommendation the spin coater is operated without a sample cover. Thus the solvent evaporates quickly and in turn a slight increase of the resist thickness is obtained. But the
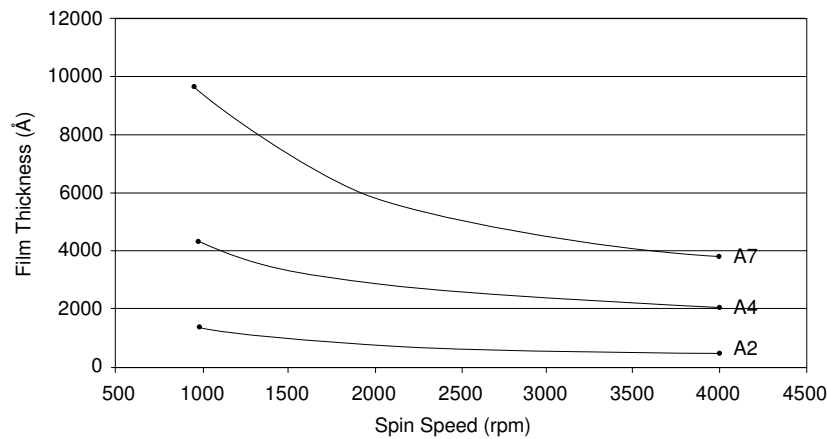
Figure 4.5: *Relation between PMMA thickness and spin speed for three different solutions with a solid content of 2% (A2), 4% (A4) and 7% (A7) in anisole. (Taken from Ref. [109])*

stable clean room conditions ensured a high reproducibility of the results.

A spurious effect is the influence of the sample size. When using samples with small lateral dimensions, e. g. 5x5 mm^2 or 10x5 mm^2, the spreading of the solution is hampered as the resist builds up at the outer edges. Consequently an overall thickness rise results and the inhomogeneities which appear in the outer parts of the sample set a lower limit for the sample size. By spin coating at 3600 rpm for 45 s film thicknesses of about 85 nm were obtained on the 5x5 mm^2 samples while the edge induced inhomogeneities restrict the usable area to about 4x4 mm^2.

To improve adhesion and resistance to chemical etching the coated samples are baked in air at 170 °C for 30 min. Immediately after exposure the specimen are developed by soaking in MIBK/IPA 1:3 for 30 s as suggested by the supplier [109]. After rinsing with IPA they are N$_2$ blow dried to finish. Due to the high contrast of the long-chain PMMA, the development profile can be well approximated by equi-energy contours [110]. Therefore the obtained structures are insensitive to the development time within a broad range of values.

4.2.2 Resolution limits and proximity effect

Several factors other than the beam diameter determine the resolution limit of an EBL system. To address this issue one has to take a closer look into the interaction processes between beam probe and sample. The incoming probe electrons dissipate their energy within a drop shaped volume through several interaction mechanisms (Fig. 4.6) while suffering elastic or inelastic scattering.

Inelastic scattering events can lead to the production of secondary-electrons with energies ranging from zero to half the energy of the scattered electron. Most secondaries have energies up to 50 eV [111], which corresponds to an electronic
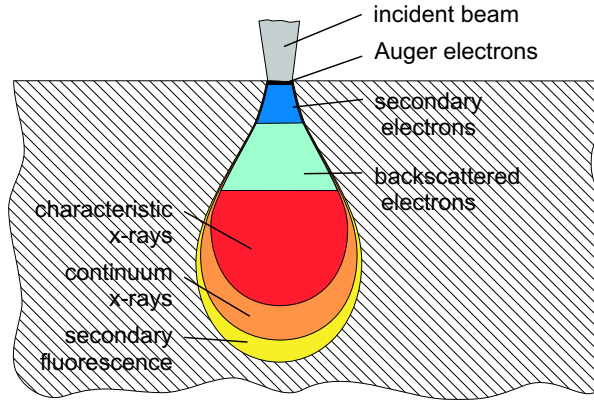
Figure 4.6: *Illustration of the various electron-specimen interaction volumes. Due to their low energies Auger and secondary electrons may only escape from a thin layer of the sample, though they are produced throughout the whole volume.*

mean free path of approximately 10 nm in the polymer. This value can be considered as a lower resolution limit. Other inelastic processes such as plasmon excitation and x-ray production through inner shell ionisation do not contribute to resist exposure.

The elastically scattered electrons, which are subdivided into forward and backward scattered entities, dissipate energy through continuous deceleration. Depending on electron energy, sample materials and thicknesses their relative contribution in the vicinity of the incident beam may vary drastically. In most cases it is a good approximation to assume a Gaussian distribution for each sort with sigma values of σ_f for forward scattering and σ_b for backscattering. The overall normalised exposure distribution is then given by the proximity function

$$F_p(r) = \frac{2}{\pi(1+\eta)} \left\{ \frac{1}{\sigma_f^2} \exp\left(-\frac{2r}{\sigma_f}\right)^2 + \eta \frac{1}{\sigma_b^2} \exp\left(-\frac{2r}{\sigma_b}\right)^2 \right\}, \qquad (4.1)$$

where r is the radial distance from the centre of the exposure and η the ratio between the exposure due to backscattered versus incident electrons [112]; σ_f, σ_b and η are determined by comparing either with Monte-Carlo simulations or experimental results [112, 113, 114]. As an example energy distributions for a 1 μm thick PMMA layer on a silicon substrate at different acceleration voltages and the corresponding parameter values are shown in Fig. 4.7. It is evident that the width of the forward scattering distribution is reduced as the electron energy increases, whereas the disc size of exposure due to backscattering from the substrate increases with rising acceleration voltage.

For very high energies of > 50 keV the distribution width becomes so large (> 5 μm) that the backscattering merely produces a background which reduces the contrast of the resist material. Therefore best resolution can be obtained by using thin layers of a high contrast resist, such as PMMA 950k, together with a
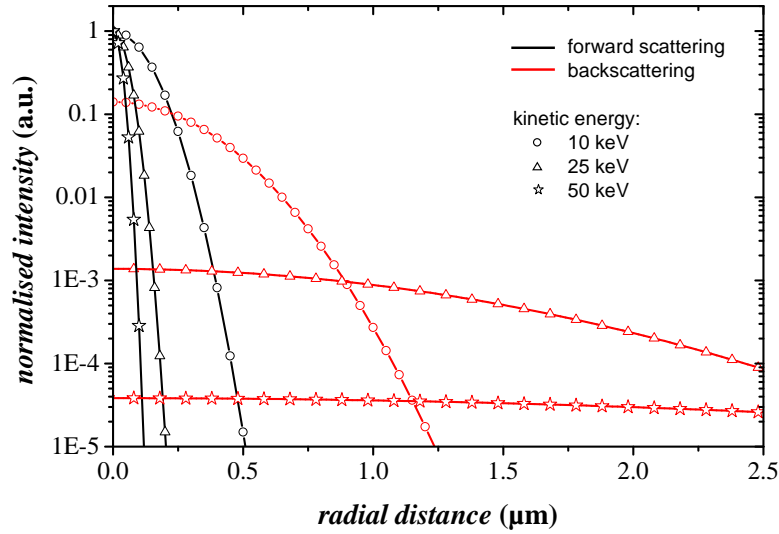
Figure 4.7: *Distribution of the energy deposition due to forward scattered and backscattered electrons in a 1 μm layer of PMMA resist on silicon.*

high acceleration voltage. To prevent over-exposure the proximity effect arising from the backscattering contribution has to be corrected when pattern arrays with spacings smaller than σ_b are fabricated.

For acceleration voltages of the order of 10 keV the proximity effect is more complicated as both the forward as well as backscattered distributions become comparable to the structure sizes. In this case one has to distinguish intraproximity and interproximity effects. While interproximity effects describe the exposure of a structure by other nearby structures, the intraproximity effects are determined by the shape and size of an individual pattern element [110]. A nice example is a homogeneously exposed square with dimensions similar to the distribution width. The energy dissipated at the midpoint of the edges is only 0.5 compared to the centre, while the corners receive 0.25 times the dose of the centre.

The e-beam patterns presented in this work have been produced with 20 keV electrons. Therefore proximity corrections were necessary. As our system, consisting of a JEOL 6300F field emission microscope with a pattern generator and software by Raith (Elphy Plus Ver. 2.07), does not comprise a proximity correction, dose and size adjustments had to be done by hand using a trial and error approach.

An important point which is neglected by the previously discussed treatment of proximity effects is the depth profile of the energy distribution. According to simulations each of the mentioned processes has a typical interaction volume (see Fig. 4.6). As a result of these cone-shaped regions of energy deposition, the developed resist patterns posses a characteristic undercut profile, which means

that the resist pattern is wider at the resist-substrate interface than at the surface. A detailed review on these issues can be found in Ref. [110].

For the lift-off process this feature is advantageous since the material which is deposited over the resist pattern forms free standing structures in the voids, allowing the sacrificial double layer of resist and deposited film to be removed easily. In those cases, where an undercut profile is not desirable, multilayer resists with different sensitivity of the constituents can be used for compensating the inhomogeneous energy distribution.

4.3 Arrays of magnetic structures with submicron dimensions

In view of the technological requirements the fabrication of chains and arrays of identical submicron structures is well suited for testing the performance of an EBL system. Exactly these designs are of main interest in the current progress of nano-structured magnetic materials. Magnetic storage techniques rely on the possibility to save information by modifying the magnetisation orientation of a single element in an array, independent of the state of a neighbouring one. On the other hand, first magnetic devices based on chains of magnetic dots have been produced [6]. They exploit the magnetostatic coupling between sufficiently small elements to execute logic processes. Therefore it is vital to study the behaviour of such structures near the expected crossover.

4.3.1 Micromagnetism

Particles smaller than the characteristic domain wall thickness are either single domain or adopt an incoherent magnetisation pattern. The actual configuration results from a competition between the exchange energy, trying to achieve a parallel alignment of the spins, and the magnetostatic energy of the stray field. In principle, micromagnetic simulations, which give a numerical solution of the Landau-Lifshitz-Gilbert equation [115, 116], can be used to model the possible magnetisation patterns for any arbitrary combination of shapes and sizes. However, identical structures are advantageous as they allow a direct comparison between theory and experiment and minimise computation time.

Pioneering work in the experimental sector has been done by Cowburn and co-workers on $Fe_{80}Ni_{14}Mo_5$ supermalloy structures. They investigated the variation of magnetic properties in different shapes of nanoelements [117], particularly the behaviour of circular dots. As a function of diameter and thickness a crossover in the magnetisation state from vortex to single domain was observed (see Fig. 4.8), in good agreement with recent calculations [118, 119].
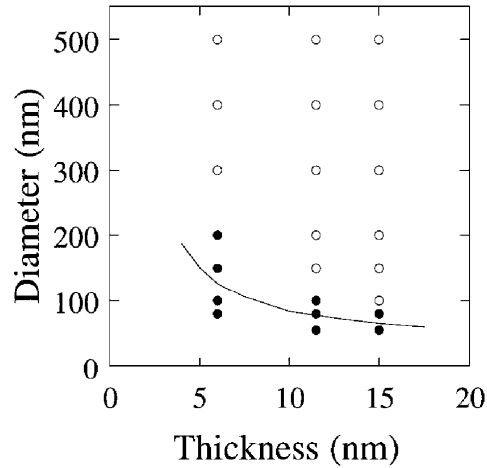
Figure 4.8: *The phase boundary between vortex and single domain state for circular dots is studied with respect to dot diameter and thickness. Experimental data has been taken at the points marked with a circle (○ =vortex, ● =single domain). The theoretical prediction is indicated with a solid line. Taken from [118].*

Due to the characteristic process of magnetisation reversal, as shown in Fig. 4.9, the two states can be distinguished.
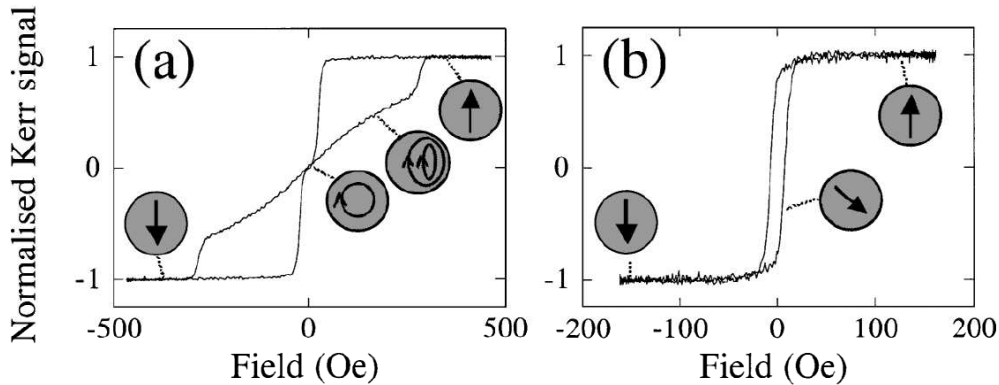
Figure 4.9: *Magnetisation reversal in vortex and single domain nanodots. The hysteresis curves were obtained by measuring the magneto-optical Kerr effect of an array of uncoupled identical dots. Taken from [118].*

In the vortex state the stray fields are minimal, since the magnetisation vectors are in-plane and tangential to a circular path. An exception is the centre of this configuration where the magnetisation points out of plane. By applying an external magnetic field, the vortex core is shifted out of the centre of the circular dot perpendicular to the field direction, while the magnetisation of the particle increases only gradually with increasing field. When the magnetic field gets larger than a certain critical value, the vortex configuration becomes unstable. Once the vortex has left the particle, the magnetisation saturates quickly. Consequently

the unusual shape of the hysteresis curve in Fig. 4.9(a) is obtained.

In the single domain state (Fig. 4.9(b)) the remagnetisation takes place by coherent rotation according to Stoner-Wohlfahrt. A uniform magnetisation is adopted as soon as the stray field energy is outweighed by the gain of exchange energy – compared to the formation of a vortex. Consequently, large stray fields appear, which lead to magnetostatic interactions between neighbouring elements. In a study of 60 nm dots at variable distance, Cowburn *et. al.* found the onset of FM coupling between the elements of a chain for a spacing of 100 nm [120].

In elliptical and rectangular dots a uniform magnetisation is stable for somewhat larger elements, but the process of magnetisation reversal is more complicated in these structures. Calculations by Usov *et. al.* predicted that remagnetisation of an elongated dot should take place due to penetration of several vortices across the element [121]. The resulting hysteresis loops along the easy axis for particles with large aspect ratio are rectangular, but with a reduced coercive field compared to the Stoner-Wohlfahrt model [122, 123].

4.3.2 Line and dot arrays fabricated by EBL

Arrays of identical permalloy lines and circular dots were fabricated on silicon (100) substrates by lift-off. The template resist structures were patterned by electron beam lithography in the previously described system. While the permalloy layer of line arrays was deposited by thermal evaporation, the dots were made by sputtering. For the purpose of lift-off structures the sputtering technique has a grave disadvantage. Due to the necessary argon background pressure of about 0.1mbar the deposited material reaches the substrate with a large spread of incident angles. As a result the typical undercut profile of the PMMA 950k is not sufficient to obtain free standing structures, which are vital for a clean lift-off. Therefore the dots were defined in a double layer resist system consisting of PMMA 950k on top of a copolymer with higher sensitivity. Details on the fabrication and characterisation of these dot arrays, including first measurements of their magnetic properties, can be found in Ref. [124].

In this work I want to focus on the preparation of 20 nm thick permalloy lines of 150 nm to 200 nm width and 1 μm length. For subsequent optical characterisation identical structures were fabricated in an array of 100×100 μm^2 size. An SEM micrograph of a sample section is shown in Fig. 4.10.

Figure 4.11 shows a part of the layout pattern, which is the prescript of how the electron beam is navigated during exposure. Each element of the array consists of a rectangle and central line. This design has been chosen, taking into account the achievable resolution of the system, to obtain lines with rounded ends.
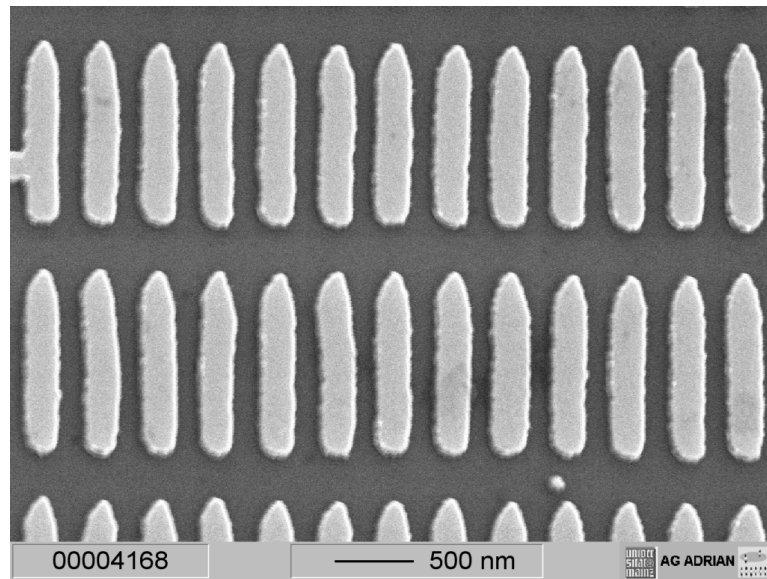
Figure 4.10: *Section of an array of permalloy structures for studying the magnetic behaviour depending on variations of size and spacings.*
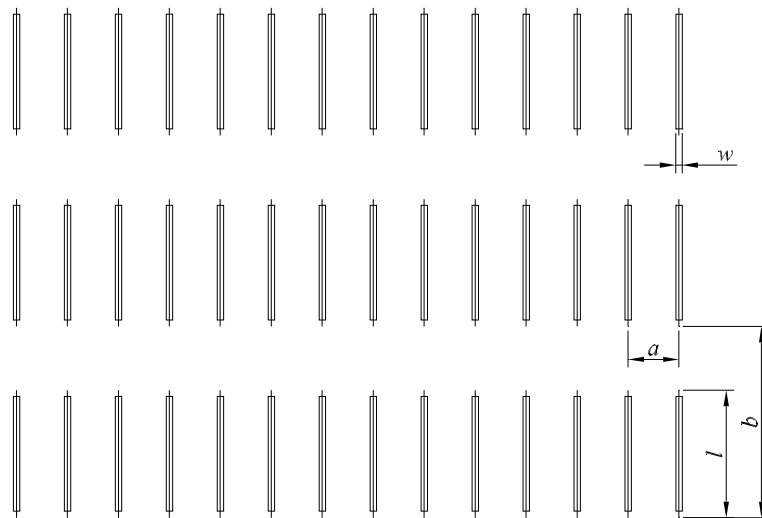
Figure 4.11: *Section of the layout pattern. The corresponding layout producing the structures of Fig. 4.10 is obtained for $a = 50$ nm, $w = 0.4$ μm, $l = 1$ μm and $b = 1.5$ μm.*

Similar arrays with different spacing and variation of the element size have been fabricated. To facilitate the identification of the different samples, each EBL structure was marked with an individual label in the lower right corner as shown in Fig. 4.12.

For all samples the distance between individual elements was of the same order as their width. Recalling the length scale of proximity effects for an accel-
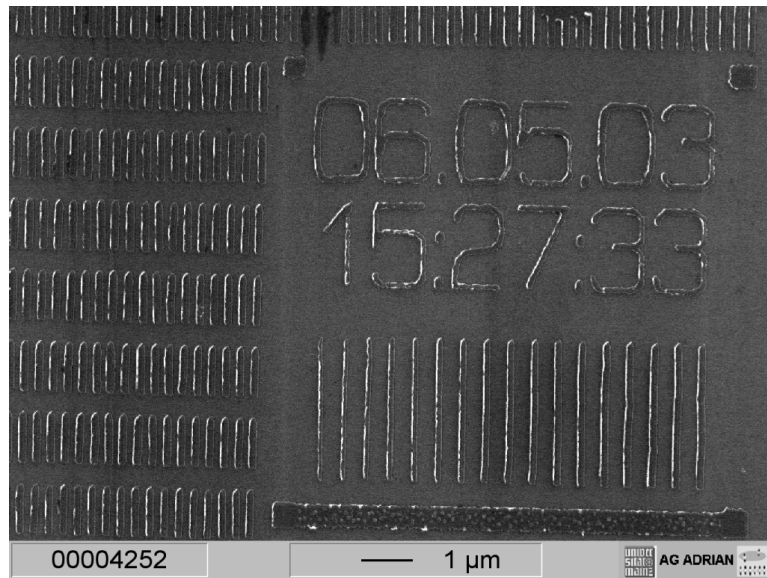
Figure 4.12: *A test pattern with date and time is used as an identifying feature for each sample.*

eration voltage of 20 kV (compare Fig. 4.7), a strong dependence of the necessary exposure dose in various arrays of this type is expected. Indeed best results are obtained for lower doses as the structure density is increased. Typical values range from 100 μC/cm^2 to 200 μC/cm^2 for the area dose and 2000 pC/cm to 10000 pC/cm for the line dose. Apart from the overall dose adjustment no proximity corrections were implemented. Since the total patterned area is at least four times larger than the laser probe spot in the optical measurements, inhomogeneous marginal structures can be tolerated as they are not probed.

As far as possible all patterns were fabricated with identical SEM settings. The working distance was kept at 7 mm and 20 kV acceleration voltage was used, but the beam current could only be adjusted in steps, where changing the setting one step reduces/increases the current roughly by a factor of 2. Accurate dose adjustment is therefore achieved by dwell time variation. An additional degree of freedom is the stepwidth, which denotes the distance travelled by the electron beam between two dwell times. It was fixed at 20 nm.

A reasonable choice for this value should take into account the minimum achievable resolution of the lithography system under the respective operating conditions, which is 80 nm in the present case. For this purpose it is instructive to evaluate a series of line scans with variable dwell time as presented in Fig. 4.13.
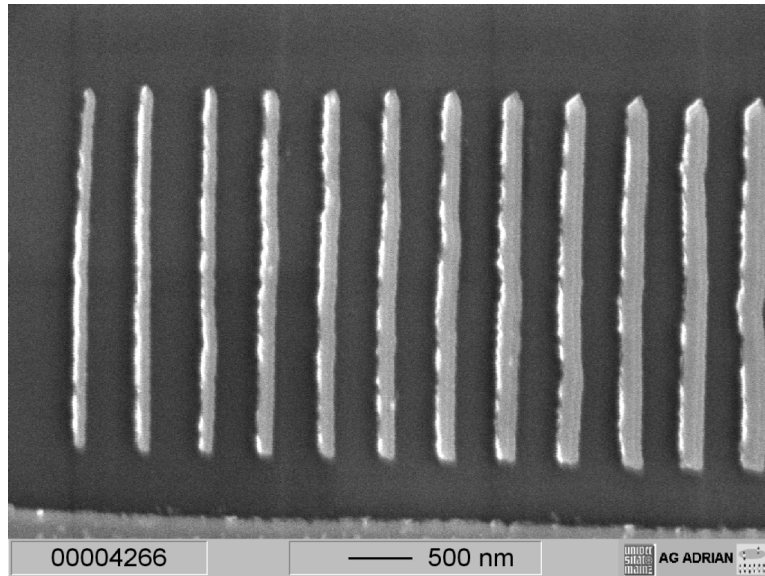
Figure 4.13: *Line test pattern with dwell time variation. From left to right the resulting exposure dose increases from 5000 pC/cm to 16000 pC/cm. The finest continuous line is 80 nm wide.*

4.3.3 MOKE study of the remagnetisation process

The ideal method for probing the magnetisation behaviour of such structures is the magneto-optical Kerr effect (MOKE). Hysteresis loops and their angular dependence may be studied averaged over a sample area down to a few micrometers.

In the presented experiments, the external magnetic field was parallel to the sample surface and parallel to the incident plane of the light (longitudinal MOKE). By using s-polarised light, the measurements are sensitive only to the magnetisation component in the incident plane. The titanium-sapphire laser can be tuned from 750 nm to a wavelength of 850 nm and focussed into a spot of 20-30 μm diameter. Further details on this method and the respective experimental setup can be found in Ref. [125].

Measurements were performed with the magnetic field parallel and perpendicular to the permalloy lines. Abiding by the previous example of Fig. 4.10, MOKE results from the respective structures are presented in Fig. 4.14. A linear background in the Kerr signal, originating for example from the Faraday effect in the lenses, is typically observed and has been corrected. The behaviour in both orientations is clearly different from reference measurements of the unpatterned film, which is attributed to the shape anisotropy of the permalloy lines. As expected, easy axis behaviour with a significantly increased coercive field is found when the external magnetic field is oriented along the lines, while hard axis behaviour has been verified in perpendicular direction.

Following the predictions of Usov *et. al.* the lines are expected to be in the
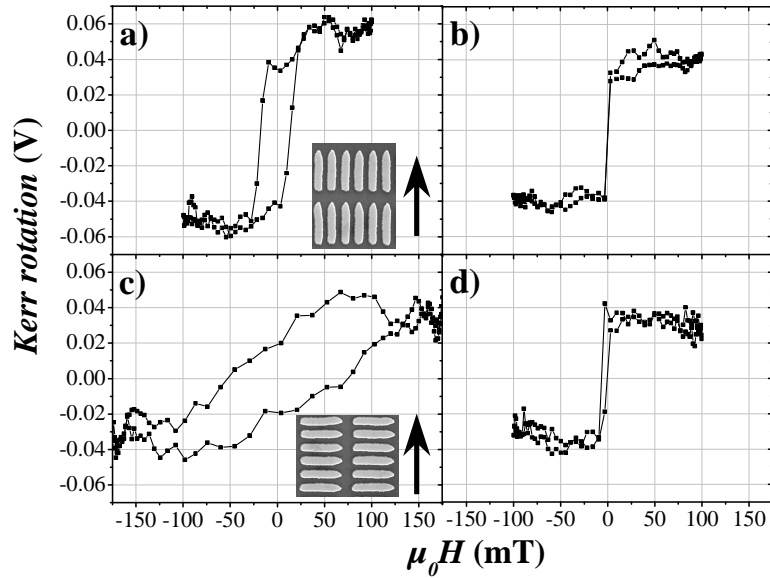
Figure 4.14: *Remagnetisation in 200 nm wide and 1 µm long permalloy lines (a) parallel and (b) perpendicular to the field direction. The reference measurements (b) and (d) were performed on a 100×100 µm² spot of unpatterned film in the vicinity of the sample array.*

quasiuniform state, where the particle is uniformly magnetised apart from some regions at the outer edges. Depending on the specific particle shape different patterns of inhomogeneous magnetisation can be adopted in these regions, which serve to minimise the stray fields. In this state the remagnetisation is initiated by the nucleation of vortices. Accordingly, the rectangular hysteresis loop in Fig. 4.14a) has a reduced coercivity ($H_c \approx 16$ mT) compared to Stoner-Wohlfahrt behaviour.

Similar switching fields have been observed by Kirk *et. al.* [126] in rectangular permalloy structures with flat ends. It was the found that flat ends lead to the nucleation of an end domain which facilitates the formation of a vortex. They also showed that the vortex nucleation can be suppressed in elements with pointed ends, resulting in a strong increase of H_c. The structures in this work have rounded ends. However, the outer edges are frayed, which has been shown previously [117] to cause a reduced coercivity.

Another interesting aspect of Ref. [126] is the dependence of the switching field on structure density. Besides a slight reduction of the average coercivity, the close packed arrays showed a wider distribution of switching fields in comparison to similar elements at larger spacing. The authors attribute this behaviour to the AFM interaction between neighbouring elements which stabilise the magnetisation state in those sample regions where an antiparallel orientation has been adopted, while switching of individual elements is facilitated if neighbouring elements are parallel aligned. In contrast to MOKE, their imaging method allowed

the observation of remagnetisation from a single element in the array.

The detection of the above described phenomenon in the present MOKE experiments is difficult since it will only show up as a rounding of the rectangular hysteresis curve. Unfortunately the experimental resolution does not allow a detailed analysis of this aspect.

4.4 Nanofabrication with a focussed ion beam

An alternative method for submicron patterning is the ion based pendant to EBL – the FIB. The system employed in this work, consists of a FIB column by Orsayphysics (CANION 31 Plus) which has been retrofitted on a JEOL scanning electron microscope (JSM6100) as shown in Fig. 4.15.
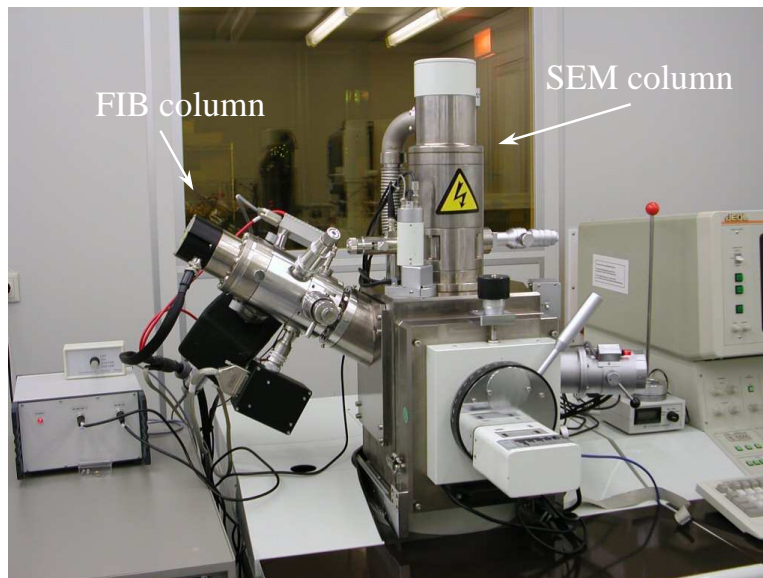
Figure 4.15: *JEOL 6100 scanning electron microscope with retrofitted FIB column by Orsayphysics. The positions of the electron and ion columns are marked in the picture.*

After a short introduction of the basic idea of focussed ion beam processing, the characteristics of our system will be presented. In certain cases it may be advantageous to use EBL and FIB as complementary methods. A good example is the preparation of small area tunnelling junctions, which is described in section 4.5.

As one of a few techniques FIB allows the direct fabrication of nanometre scale structures by ablating material from the exposed areas. Positively charged Gallium ions are extracted from a field emission tip which is covered by the liquid metal. Accelerated to several kilovolts and focussed into a beam with diameter

down to a few nanometres the Ga^+ ions can be used to sputter material from the surface of a target. As shown in Fig. 4.16 the ion beam is scanned across
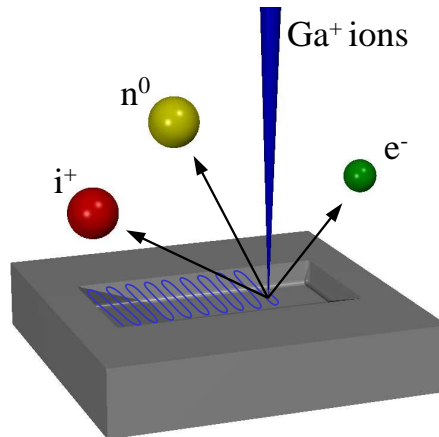
Figure 4.16:   *The interaction between a collimated beam of several keV Ga^+ ions and the target leads to sputter ablation from the sample surface. Positively charged (i^+) as well as neutral atoms (n^0) leave the surface. Additionally secondary electrons (e^-) are produced by the primary beam.*

the sample allowing arbitrary 2D shapes to be produced. In contrast to other methods which employ chemical processes, FIB etching can be done with nearly any kind of material. Besides, element specific gas assisted etching and deposition are also possible. Due to these features the FIB has become a versatile tool in semiconductor industries for prototyping, failure analysis and mask repair.

It is common to combine the FIB system with a scanning electron microscope (SEM) as in our case. In such setups the imaging capability of the FIB, which results from the detection of the secondary electrons, is mainly used to optimize the beam quality. By navigating with the SEM image instead, one can prevent the sample surface from being destroyed by the invasive imaging mode of the FIB. Furthermore real time monitoring of the etching process is enabled.

4.4.1   Performance characteristics of the SEM/FIB facility

The SEM chamber layout permitted the FIB to be placed at an angle of $60°$ with respect to the electron gun. To prevent possible collision of sample stage and FIB gun, the x-range of the stage had to be restricted to about 10 mm. Since both column positions are fixed, a simultaneous SEM and FIB picture of the same sample spot can only be achieved for a certain fixed working distance. In our case the WD of the coincidence point is 24 mm at a tilting angle of $60°$ with respect to the electron gun, which is the position of perpendicular alignment between FIB beam and sample stage. As the depth of focus in FIB systems is generally in the micrometer range or above, which is much larger than the typical etching depth

needed, it would be preferable to work at smaller WD. The impossibility to vary this parameter constitutes a certain restriction of the system.

The gun specifications allow to work with ion energies ranging from 8 to 30 keV at optimum ion currents between 1 and 2 μA. For all structures, which have been produced during the course of this thesis, 20 keV acceleration voltage was used, whereas the beam current varied in the specified range. With these settings minimum structure dimensions of 100-200 nm could be achieved. Figure 4.17 shows an SEM image of a line array fabricated by FIB etching.
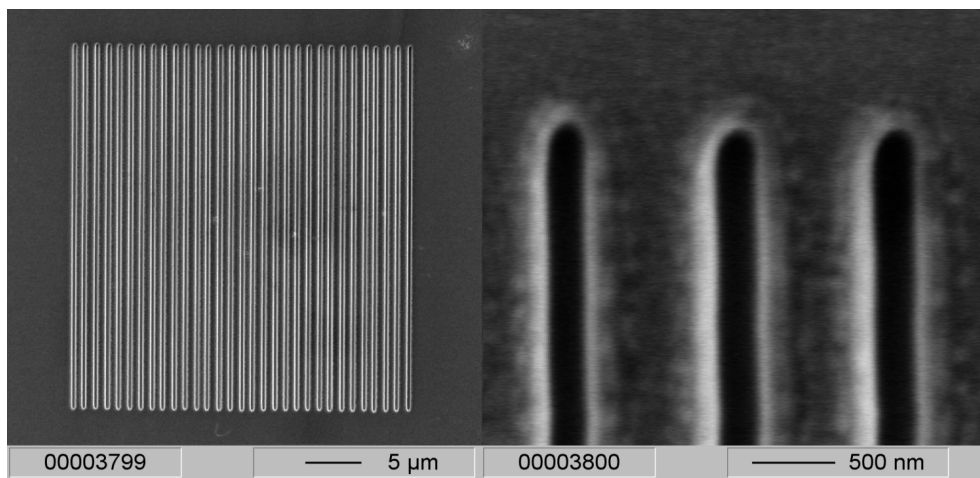
Figure 4.17: *SEM micrographs of a FIB etched line array at two different magnifications. The 200 nm wide lines have been written in a Fe/Mo film on Si substrate. The structure size is close to the resolution limit.*

Here a 25 nm thick Fe film, which has been protected by a thin Mo layer, was employed. To facilitate charge compensation the film was prepared on a doped Si substrate. In this example a single pixel line scan has been performed, rendering a linewidth of about 200 nm. The spacing between two lines is 1 μm. Due to the re-deposition of material in the vicinity of the written structures, the edge contrast is enhanced and may give the impression of a larger size.

It turned out that the careful alignment of aperture, stigmator and fine focus is crucial. In order to achieve minimum feature sizes these three parameters have to be varied iteratively. A short FIB operation manual in Appendix B describes the technical issues in more detail. Though the limited resolution of the SEM does not have a direct impact on the FIB resolution, an equivalent performance would be of significant advantage, as the navigation and etching control is done with the SEM image. However, in our case also the rather bad base pressure of the chamber, which is typically $2 \cdot 10^{-5}$ mbar, may have a detrimental effect on the FIB performance.

4.5   Small area TMR devices

Magnetic tunnel junctions (MTJ), which exploit the TMR effect, have been introduced successfully as storage devices [1, 127]. In this context the need for submicron structures is obvious. However, small area devices are also preferentially used in fundamental studies. Several physical effects, namely current redistribution [63], the influence of domain walls and defects as well as heating, can be controlled more efficiently in junctions of a few micrometers or less.

Certainly the most intuitive way to construct a tunnelling junction is the preparation of crossed wires by shadow masking. For nanoscale junctions EBL patterned resist masks may be used, but the polymers do not withstand the elevated substrate temperatures which are required for the preparation of the discussed oxide materials. In this case a trilayer thin film, which homogeneously covers the whole sample area is prepared and subsequently patterned into a mesa structure. For this purpose the FIB proved to be an appropriate tool.

In contrast to the fabrication of nano-structure arrays in section 4.3.2, the lithography system is not working close to the resolution limit. The main difficulty this time is the precise alignment of several lithography steps and control of the etching depth.

4.5.1   Pre-structuring by optical lithography

For the study of electronic properties it is indispensable to fabricate the mesa on a pre-defined position, which allows subsequent wiring. The required pre-structure is made by optical lithography. The positive tone UV resist AZ-6612 (MicroChemicals GmbH) was dispersed by spin coating at 6000 rpm for 30 s and subsequently baked at 100°C for 20 min. Best results were obtained with a UV exposure time of 50 s, followed by 50s development in NaOH. Depending on the film materials the unprotected sample parts are removed by ion beam or wet chemical etching.

In this first step, the multilayer thin film is patterned into measuring and marker structures as shown in Fig. 4.18. In each corner of the pattern a marker is situated which may serve as an origin for the sample coordinates and for optimising the FIB/SEM settings. The central T-bar contains six working areas of $400 \times 400 \ \mu m^2$ size, defined by crosses, where the mesa structures will be fabricated. Six big crosses situated along two sides of the sample ensure proper alignment of the final optical lithography step, and the rectangular shapes define the position of the bonding pads.
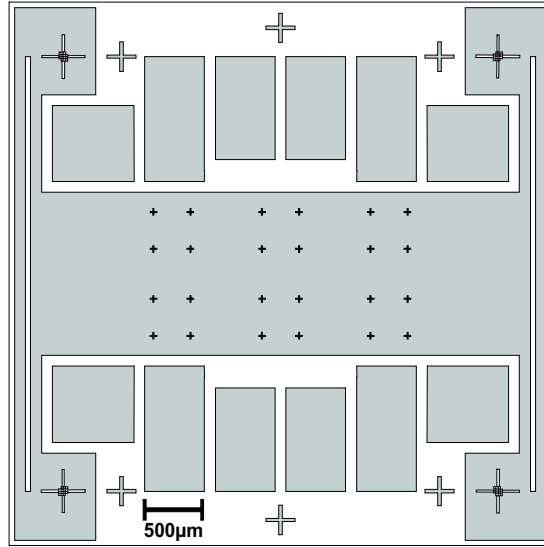
Figure 4.18: *Pre-structure for fabricating small area MTJ's. The grey areas indicated the parts of the pattern were the multilayer thin film is retained. In the white areas the film is removed completely.*

4.5.2 Definition of the mesa structure by FIB etching

A custom made FIB holder (see Fig. B.1) establishes electrical contact between ground and the central T-bar, where FIB processing will take place. This is vital to prevent charging effects. Following the description in Appendix B, FIB and SEM are operated together.

Having chosen one of the pre-defined working areas in the SEM, the respective markers are scanned and adjusted to the writefield corners in the control software. By increasing the FIB attenuation from 1 to 10, the working area is reduced to a 40×40 μm^2 large area in the centre of the initial one. This field is marked by etching a cross in each corner. The actual mesa structure is fabricated in turn at attenuation 50, which corresponds to a field size of 8×8 μm^2. Since the dimensions of the mesa are much smaller than the resolution of the optical pre-structure these additional markers are required for a proper alignment of subsequent fabrication steps. The processed 400×400 μm^2 field is shown in Fig. 4.19.

Typical etching times are several minutes using the smallest aperture size of 20 μm. It is important to note that the mesa is defined by removing the top electrode and barrier around it, while the bottom electrode has to remain intact as sketched in Fig. 4.20. Therefore it is vital to have full control over the etching depth. This is typically done by monitoring the sample current. By multiplying with the respective stepwidth and dwelltime, the exposure dose is obtained. Its value is directly related to the etching yield of a specific material.

The sample current, which is stated in our FIB software, is not a reliable
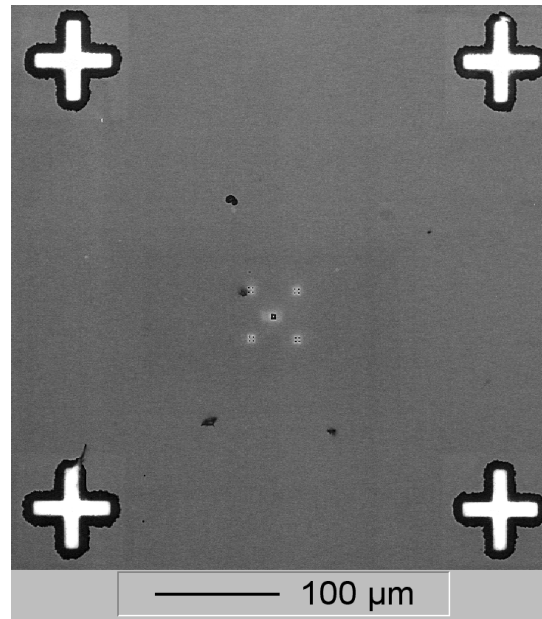
Figure 4.19: *Mesa structure and calibration markers. The large crosses have been fabricated in the pre-structuring step by optical lithography and wet chemical etching. The inner markers and the mesa were added with the FIB.*

Gold cap layer
top magnetic layer
insulating barrier
bottom magnetic layer

substrate
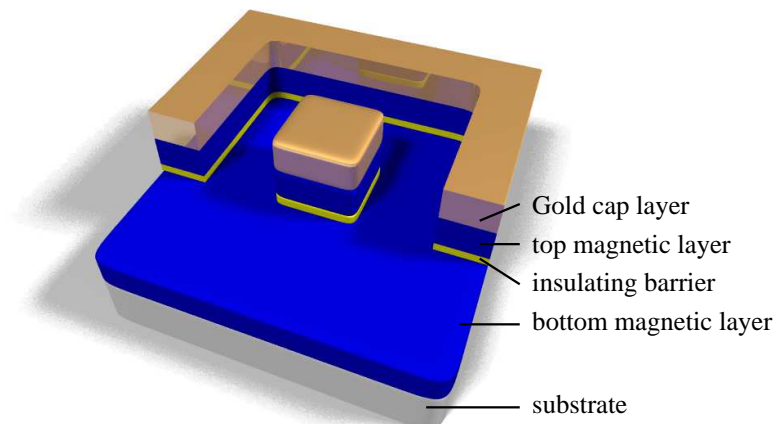
Figure 4.20: *Visualisation of the mesa etching profile. The layer thicknesses are exaggerated as compared to the lateral dimensions of the mesa.*

parameter as it depends on the sample position, presumably due to shadowing by other system components in the vacuum chamber. Therefore the etching speed is calibrated for each sample by fabricating a test pattern. For this purpose the FIB is operated in viewing (SEM/Area) mode at magnification $M = 100$. When the conducting film material has been removed completely from the exposed sample spot, the picture brightness drops drastically. The required time t_0 multiplied by a calibration factor yields the necessary exposure time for the respective pattern

$$t_{exp} = t_0 \cdot x \cdot \frac{A}{45 \mu m^2} \ , \tag{4.2}$$

where a fraction x of the film thickness is removed from the sample area A. The calibration factor has been determined experimentally by comparing the etching depth in two rectangles for identical exposure time, where one has been created as described above and the other by using the standard writing mode. As the etching speed may vary for different types of materials, Eq. (4.2) has to be regarded as an approximation if multilayer systems are processed. Adequate adjustments of the calibration factor may be necessary.

The test mesa of Fig. 4.21 was fabricated in a Co-Al$_2$O$_3$-Co trilayer. Starting from a (190 ± 10) nm thick stack, the mesa surroundings were thinned down to 60 nm. Thus, complete removal of the top layer is ensured, while enough material remains in order to serve as the base electrode.
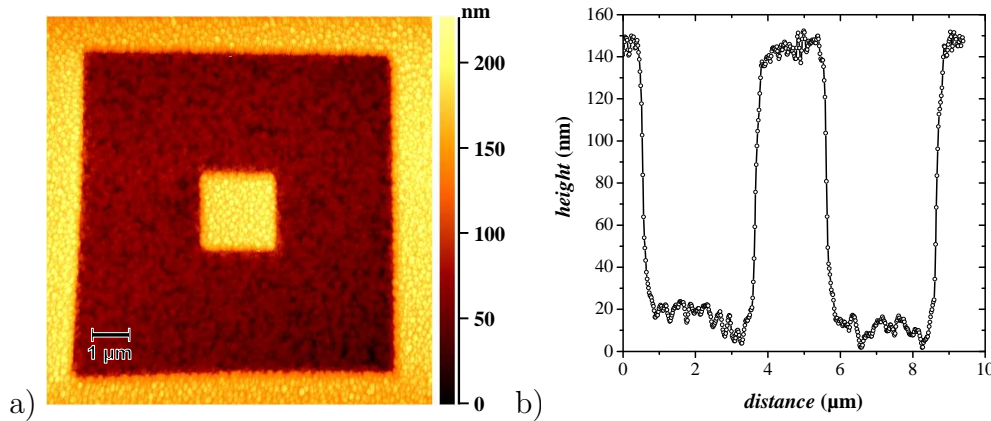
Figure 4.21: *a) AFM micrograph of the mesa. b) A line scan across the image centre reveals an etching depth of 130 nm.*

4.5.3 Finalising steps of mesa fabrication

Technically likewise demanding as the preparation of the mesa is the fabrication of its electrical contacts, which will require two more lithography steps. In a first EBL run a PMMA film is patterned such that a resist free window is formed just on top of the mesa as shown in Fig. 4.22.

The remaining PMMA layer around the contact may serve as insulation once it has been made resistant to acetone. For this purpose the PMMA needs to be exposed to a dose fifty times higher than the standard exposure dose. The gold contacts are subsequently fabricated on top of the resist structure by lift-off with standard UV optical lithography. A cross-section of the proposed layout for the final device is shown in Fig. 4.23.

First investigations show that the EBL system can achieve a positioning accuracy below 1 μm which is sufficient if this design is used. Due to the universal
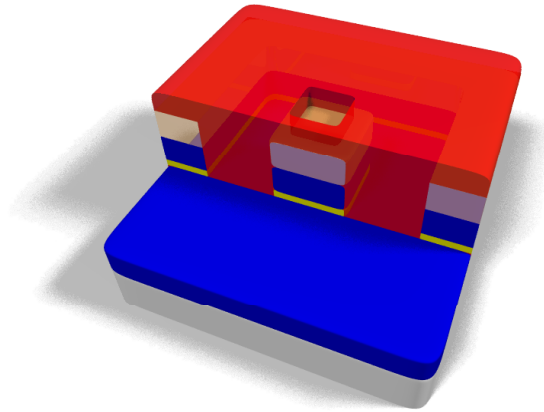
Figure 4.22: *Visualisation of the mesa device after EBL processing. This step is used to define a contact window in PMMA.*
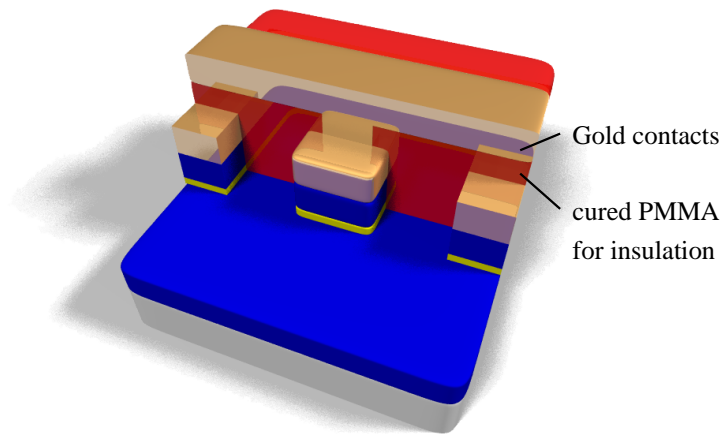
Figure 4.23: *Visualisation of the final mesa device.*

etching capabilities of the FIB small area junctions can be fabricated from any combination of materials as long as charge compensation is ensured.

In order to establish device-oriented submicron patterning as a standard technique, electron beam lithography and focussed ion beam etching facilities have been put into operation. A detailed characterisation of these systems has been performed. Emphasis was put on identifying the lateral resolution under the given experimental conditions. It was demonstrated that EBL structures of 80 nm width can be fabricated, while 200 nm were achieved with the FIB. The current drift of the electron gun, which is a characteristic trait of cold field emission, imposes some restrictions on EBL operation. If structures of 200 nm or below are fabricated, the exposure time should not exceed 15 min. FIB processing is not subject to this limitation.

For each system typical applications have been discussed. The required process chains, developed during the course of this thesis, have been worked out to serve as a general operation guide.

Summary

Starting with the investigation of the magnetoresistive double-perovskite oxide Sr_2FeMoO_6, the thesis developed into a comprehensive study of current tasks in the field of magnetic storage technology. According to the groups main competence, the preparation, characterisation and device oriented nano-processing of thin film samples were accomplished.

Based on the preparatory work of Refs. [62, 32] the fabrication of Sr_2FeMoO_6 thin films by laser ablation was optimised. A close relation was identified between the deposition rate, the oxygen partial pressure during different stages of the preparation process and the antisite disorder. It was found that oxygen deficiency has a detrimental effect on the material properties, while excess oxygen additionally leads to the formation of the $SrMoO_4$ parasitic phase. This is an interesting result concerning the integration of oxide materials into standard semiconductor technology. Despite of their functional potential, the industry hesitates to utilise oxides in their systems due to the necessity of working at high oxygen partial pressures. Therefore the deposition of functional oxide materials in low oxygen environment may open up a promising new route of investigation.

Furthermore it was possible to correlate the antisite disorder directly to the measured saturation magnetisation of the samples. Due to the influence of the $SrTiO_3$ substrate the Sr_2FeMoO_6 layer is subject to an in-plane compressive strain, which seems to promote the formation of the disordered phase and restrict the saturation magnetisation to about 80 % of the theoretical value.

In a comparative study of different film series, transport measurements unveiled the complex nature of the electronic properties. The temperature dependence of resistivity has been broadly discussed and a scenario of small-polaron transport has been proposed as a possible origin for the unusual behaviour. Particular attention has been given to the magnetoresistive response of the samples. Compared to polycrystalline bulk material the epitaxial thin films exhibit a much smaller MR, which can be clearly attributed to the reduction of inter-grain tunnelling in the epitaxial layers. It has been discussed that the remaining MR sig-

nature stems from disorder induced boundaries. While moderate levels of antisite disorder tend to increase the effect, a decrease of the MR ratio is observed for high ASD levels. This result is consistent with theory, which predicts a decrease due to the loss of spin polarisation in the disordered phase.

In the second part of this thesis it was set out to measure the transport spin polarisation of the prepared Sr_2FeMoO_6 thin film samples by point contact spectroscopy. These investigations resulted in a fundamental study on the PCAR method itself.

The spectra of two high resistive materials of potential half-metallic character, namely Sr_2FeMoO_6 and $Co_2Cr_{0.6}Fe_{0.4}Al$, have been analysed. For Sr_2FeMoO_6 the standard treatment by BTK and Mazin's diffusive model did not render a satisfying description of the data. Consequently an extension has been developed in this work, which takes into account the possible influence of inelastic scattering processes in the contact area. One implication is that an individual temperature for each point in the conductance spectra has to be considered by adequate modification of the quasiparticle distribution function. Furthermore, a local temperature increase changes the size of the superconducting gap, which is also implemented in the analysis. Altogether a dramatic effect on the shape of the spectra is observed.

With this approach the systematic deviations between Mazin's model and the acquired measurements could be well explained, yet at the expense of obtaining a whole parameter space of possible P and Z values. The $Co_2Cr_{0.6}Fe_{0.4}Al$ measurements where simulated with the modified diffusive as well as ballistic model. In both cases good agreement was achieved, but for different parameter sets.

Though it was not possible to extract a reliable value of spin polarisation, these investigations provide an insight into practical limitations of the PCAR method. In view of the large number of experimental reports, where this approach is employed for probing the spin polarisation, the reliability of the PCAR method is of vital importance. Though heating is certainly only one aspect, when it comes to a realistic description of the problem, the work presented here exemplifies that inelastic processes may affect the obtained spectra as well as the derived spin polarisation value drastically and that it is not admissible to consider an idealised contact in all cases.

Electron beam lithography and focussed ion beam etching have been implemented for nanopatterning of various materials. A first task was to explore the system specific properties, including lateral resolution, stability during long exposure cycles and the influence of different exposure parameters.

With the EBL system emphasis was put on the fabrication of arrays of identical nanosized magnets due to its high resolution. The patterned particles were

subsequently studied by the magneto-optical Kerr effect. The sharpness of magnetic switching indicates that a narrow size distribution of the structures was obtained. The hysteresis loops in the regime of non-interacting particles can thus be understood as if they were generated by a single nanomagnet allowing a direct comparison with existing simulations.

Good depth control of the etching process combined with sub-micron lateral resolution is the particular benefit of the FIB. An application where these qualities prove advantageous is the fabrication of small area tunnelling junctions. Basic considerations concerning the mark layout, especially with respect to the alignment requirements, have been made. To verify proper operation of the process first steps in the preparation of a $Co/Al_2O_3/Co$ junction have been performed.

Appendix A

PCAR simulation routines

A.1   MATLAB program for ballistic contacts

```
% Normalleiter-SL-Andreev Reflektion
% nach Mazin, Golubov and Nadgorny (ballistic limit)

Delta=1.001; % Energieluecke in meV, Abschaetzung
P=0;
% Delta inkommensurabel mit E waehlen
Z=0.1;
Zs=Z*Z; % Reflection Coefficient
T=1; %Temperatur in K
TeV=T/11.6; % Temperatur in meVDelta2=Delta0^2;
Tc=9; % kritische Temperatur in K
Delta2=Delta.^2;
dE=0.05; dV=0.05; % Schrittweiten in meV
E=-30:dE:30; %Energiebereich in meV ; 1meV=11.6kB;

V=-15:dV:15; % Spannungsbereich in meV
Es=E.*E;

FermiE=1./(exp(E)+1);
DFermiDE=exp(E)./(exp(E)+1).^2;

Es=Es+eps; % Um in folgender Zeile Division durch 0 zu vermeiden
u0s=0.5*(1+sqrt((1-Delta2./Es))); %BCS Kohaerenzfaktoren
urs=real(0.5*(1+sqrt((1-Delta2./Es))));
Es=Es-eps;
v0s=1-u0s;
vrs=1-urs;
bet1=abs(E./sqrt(Delta2-Es+eps)).*(abs(E)<Delta);
```

```matlab
bet2=1./(u0s-v0s+eps).*(abs(E)>Delta);

gs=(urs+Zs*(urs-vrs)).^2;
g=(u0s+Zs*(u0s-v0s));

A=2.*(1+bet1.^2)./(bet1.^2+(1+2.*Zs).^2).*(abs(E)<Delta);
B=1./(g+eps).*(abs(E)>Delta);
Bp=4.*bet2./((1+bet2).^2+4.*Zs).*(abs(E)>Delta);

Trans=(1-P)*(A+B)' + P*(Bp)';

maximum=100;minimum=-100;
for i=1:length(V)
   x=(E+V(i))/TeV; % Energieskala um V(i) verschieben
   ylow=(-100>=x); yhigh=(100<=x); y=and(( ylow),( yhigh));
   x=x.*y+100*yhigh-100*ylow;
   x=exp(x); % sonst num. Fehler 0/0 fuer kl. T in naechster Zeile
   DFermiDEV=x./(x+1).^2; % V(i) verschobene Abl. der Fermifkt*TeV
   DIDV(i)=(DFermiDEV*Trans)*dE/TeV; % =Integration
end;
DIDV=DIDV/DIDV(length(V));

figure(1)
plot(V,DIDV,'-')
xlabel('U (mV)')
ylabel('dI/dV')
axis([-5 5 0 2])
titel=strcat('Simulation result T=',num2str(T),'K Z=',num2str(Z));
title(titel)
```

A.2   MATLAB program for diffusive contacts

```matlab
% Normalleiter-SL-Andreev Reflektion
% nach Mazin, Golubov and Nadgorny (diffusives Limit)

   %----Material- und Mess-Parameter----%

% Delta(Pb)=1.225 Delta(Nb)=1.51 Delta(Sn)=0.58
Delta=0.51; % Energieluecke in meV, Abschaetzung
% Delta inkommensurabel mit E waehlen

   % Tc(Pb)=7.2 Tc(Nb)=9.26 Tc(Sn)=3.72
Tc=3.72; % kritische Temperatur in K
```

```
Z=0; % Reflection Coefficient
T=1.8; % Temperatur in K
P=1; % Polarisation

   %----Korrekturparameter----%

Gp=3.2; % Parallele Leitfaehigkeit
Gu=0.0; % Parallele Leitfaehigkeit linear in V
Rs=1.9; % Serienwiderstand der nicht zum AR-Signal beitraegt
Ru=0; % Serienwiderstandsanteil linear in V
frac=0.75; % Anteil thermisch

   %----Beginn des Programms----%

Zs=Z*Z;
dE=0.05; dV=0.025; % Schrittweiten in meV
E=-30:dE:30; % Energiebereich in meV ; 1meV=11.6kB;
V=0:dV:5; % Spannungsbereich in meV
Es=E.*E;
TeV=T/11.6; % Temperatur in meV

DIDV=0;
for i=1:length(V)
   Teff(i)=sqrt(TeV^2+frac*V(i)^2/12.9)*11.6;

   if Teff(i)<Tc
   DeltaTeff(i)=Delta*sqrt(cos(pi/2*(Teff(i)/Tc)^2));
   Delta2=DeltaTeff(i)^2;

   beta=abs(E./sqrt(Delta2-Es+eps))+eps; %Kohrenzfaktor

   %A(F1):  DNM E<Delta B(F2):  DNM E>Delta C(F3):  DHM E>Delta
   F1=(acosh(2*Zs-j*beta)./sqrt((2*Zs-j*beta).^2-1)-
       acosh(2*Zs+j*beta)./sqrt((2*Zs+j*beta).^2-1)).*(abs(E)<Delta);
   F2=acosh(2.*Zs+beta)./(sqrt((2.*Zs+beta).^2-1)+eps).*(abs(E)>Delta);
   arg3=((1+beta).^2)./2-1;
   F3=acosh(2.*Zs+arg3)./(sqrt((2.*Zs+arg3).^2-1)+eps).*(abs(E)>Delta);

   A=(1./beta+beta).*imag(F1);
   B=2.*beta.*F2;
   C=beta.*F3;
   Trans=(1-P).*(A+B)'+P.*C';

   x=(E+V(i))/sqrt(TeV^2+frac*V(i)^2/12.9);
```

```
    % Energieskala um V(i) verschieben = andere Seite der Barriere
    ylow=(-100>=x); yhigh=(100<=x); y=and(( ylow),( yhigh));
    x=x.*y+100*yhigh-100*ylow;
    x=exp(x); % sonst num. Fehler 0/0 fuer kl. T in naechster Zeile
    DFermiDEV=x./(x+1).^2; % V(i) verschobene Abl. der Fermifkt*TeV
    % =Integration:
    DIDV(i)=(DFermiDEV*Trans)*dE/sqrt(TeV^2+frac*V(i)^2/12.9);
    else DIDV(i)=DIDV(i-1);
    end;
end;
Gclean=DIDV;
DIDV=0;
for i=1:length(V)

    if Teff(i)<Tc
    Delta2=DeltaTeff(i).^2;
    beta=abs(E./sqrt(Delta2-Es+eps))+eps; %Kohrenzfaktor

    %A(F1):  DNM E<Delta B(F2):  DNM E>Delta C(F3):  DHM E>Delta
    F1=(acosh(2*Zs-j*beta)./sqrt((2*Zs-j*beta).^2-1)-
        acosh(2*Zs+j*beta)./sqrt((2*Zs+j*beta).^2-1)).*(abs(E)<Delta);
    F2=acosh(2.*Zs+beta)./(sqrt((2.*Zs+beta).^2-1)+eps).*(abs(E)>Delta);
    arg3=((1+beta).^2)./2-1;
    F3=acosh(2.*Zs+arg3)./(sqrt((2.*Zs+arg3).^2-1)+eps).*(abs(E)>Delta);

    A=(1./beta+beta).*imag(F1);
    B=2.*beta.*F2;
    C=beta.*F3;
    Trans=(1-P).*(A+B)'+P.*C';

    x=(E+V(i))/sqrt(TeV^2+frac*V(i)^2/12.9);
    % Energieskala um V(i) verschieben = andere Seite der Barriere
    ylow=(-100>=x); yhigh=(100<=x); y=and(( ylow),( yhigh));
    x=x.*y+100*yhigh-100*ylow;
    x=exp(x); % sonst num. Fehler 0/0 fuer kl. T in naechster Zeile
    DFermiDEV=x./(x+1).^2; % V(i) verschobene Abl. der Fermifkt*TeV
    % =Integration:
    DIDV(i)=(DFermiDEV*Trans)*dE/sqrt(TeV^2+frac*V(i)^2/12.9);
    %Parallelleifhigkeits-Korrektur:
    DIDV(i)=DIDV(i)+(Gp+Gu*V(i))*Gclean(length(Gclean));
    else DIDV(i)=DIDV(i-1);
    end;
    I(i)=(sum(DIDV)-DIDV(i))*dV;
end;
```

```matlab
Inorm=I./I(length(I));
DIDV=DIDV/DIDV(length(V))*0.997;
%Serienwiderstand-Korrektur:
Vkorr=V+Inorm.*(Rs*V(length(V))+Ru*V*V(length(V)));
%Bereich 0 bis V --> -V bis V
for i=1:length(V)
   Teff2(i)=Teff(length(V)-(i-1));
   DIDV2(i)=DIDV(length(V)-(i-1));
   I2(i)=-I(length(V)-(i-1));
   V2(i)=-Vkorr(length(V)-(i-1));
   Teff2(length(V)+i-1)=Teff(i);
   I2(length(V)+i-1)=I(i);
   V2(length(V)+i-1)=Vkorr(i);
   DIDV2(length(V)+i-1)=DIDV(i);
end;

figure(1)
load sfmo120b.dat;
U=sfmo120b(:,1)*1000;
G=sfmo120b(:,2);
Gn=(G/max(G))*1.03;
plot(V2,DIDV2,'b-',U,G,'g*',V2,Teff2/Tc,'r-')
axis([-6 6 0.7 1.2])
xlabel('U (mV)')
ylabel('dI/dV')
titel=strcat('Andreev Reflection (diffusive limit)
              T=',num2str(T),'K Z=',num2str(Z),' P=',num2str(P));
title(titel)
```

Appendix B

FIB operation manual

B.1 Sample holder and preparatory steps

A sample holder (see Fig. B.1) has been designed to meet the special requirements of FIB work. Due to the restricted movements of the xy-table, the optimum sample size is 5×5 mm^2, which is also the maximum size accepted by the holder.
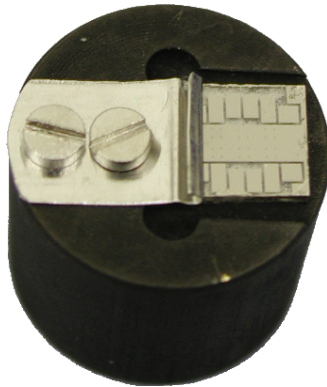
Figure B.1: *Sample holder designed especially for FIB applications. The size of the installed sample is $5 \times 5 \times 0.5$ mm^3.*

By using the provided metal clamp fixation, the sample surface, which has to be **conducting (!)**, is grounded. Alternatively the sample can be glued to a standard holder – remember to contact the surface, if the substrate is insulating!

Sample and holder are placed into the SEM holder and fixed with a screw. Make sure that the sample is on the right side of the holder when the shuttle screwhole is visible as shown in Fig. B.2. To ensure accessibility of the whole sample, its surface has to be aligned to match the height of the SEM holder.

Before opening the SEM chamber check that the **FIB valve is closed**! Now the clamps at the side of the SEM front flange can be opened. To vent the

Figure B.2:   *Proper adjustment of the FIB sample in the SEM holder.*

chamber press the **VENT** button which is situated under the SEM desk to the left (covered with a plastic lid). The sample is introduced with the shuttle screw visible. Please mind the cables when closing the flange. By pressing **VENT** a second time the chamber is evacuated.

B.2   SEM operation

The pumps of the SEM are operating continuously, but the main components of the system are usually switched off. It is started with the metal tappet switch on the backside. The FIB control and the Elphy plus scan generator are situated in the left parral. At start-up these units and the multiway connector have to be switched on – only the control unit of the ion getter pump should be running at all times. **Afterwards** the computer can be started. To ensure that the SEM beam blanker does not interfere when raising the filament current make sure that the blanking unit is disconnected from the SEM and replaced by a 50 Ω terminating resistor. Initially the SEM monitor displays the (empty) image memory. To switch to the current SEM image press **F10**.

When the chamber pressure has become low enough for operating the filament (approx. $4 \cdot 10^{-5}$ mbar) the illumination of the filament current meter lights up.[1] Now the high voltage can be switched on by pressing the filament **ON** button followed by the acceleration voltage **HV**, which should be set to 20 kV maximum. Subsequently the filament current is slowly increased up to approx. 240 μA. It is important to watch the brightness of the image as the current is raised. The

---

[1]If the current meter lights up at too low value, the "VAC high" potentiometer (T5) in the SEM vacuum control unit needs to be adjusted.

respective curve is displayed in Fig. B.3. The proper operating point is the second maximum in the image brightness.
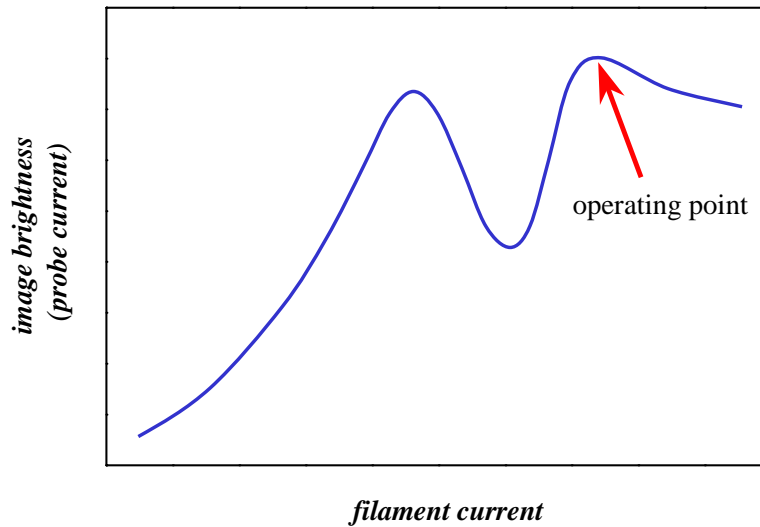
Figure B.3: *Image brightness versus filament current. The proper operating point is marked with an arrow.*

In case of no image:

- Check that the beam blanker is disconnected and terminating resistor installed.

- Reduce the magnification of the SEM.

- Check brightness and contrast of monitor/SEM settings.

While the stage tilting is still zero, the sample should be in focus roughly at a working distance (WD) of 30. Now the stage is tilted by 60°, so that the red dot is congruent with the arrow, and the focus is set to WD 24. To achieve a sharp image the height of the x,y-table is adjusted. If necessary the SEM image may be optimised by controlling the aperture alignment (wobbler) and astigmatism corrections while the focus is adjusted.

B.3 Starting the FIB unit

Start the FIB and Elphy Plus software and open the FIB valve, while checking the pressure indicator of the ion getter pump. The FIB software has to be started/closed/started – otherwise the objective lens is not operating properly.

Open the **ION GUN** dialog in the FIB software and set the voltage to the desired value (20 kV has always been used up to now). The setting is verified

by pressing **GUN ON**. Now the extraction voltage is **slowly** increased until the emission current reaches 2 μA. Emission of a properly working tip should start at $\geq$ 9kV. If the value is much higher or emission does not start at all, the tip must be reformed by heat treatment (refer to the Orsayphysics FIB manual). Exit the dialog with **CONTINUE**.

The condenser and objective lens settings should be roughly 10000 and 18000, respectively. It is useful to start with a set of old parameters for the operating conditions, which can be loaded with the **RECALL** button. Once the FIB produces some picture, the stage height should be adjusted such, that the SEM and FIB image become congruent. While the FIB image moves when the height is changed, the SEM reproduces a fixed sample spot. Thus a striking feature of the sample is chosen, moved to the centre of the SEM image and then sought with the FIB by changing the z-position of the stage. It is important to note that the SEM and FIB magnifications are different, the conversion factor is approximately SEM 340x $\cong$ FIB 1x.

The fine focussing of the FIB requires a little bit of practice. In the **Objective fine** mode the objective lens and astigmatism corrections can be adjusted. Likewise important is the adjustment of the aperture. Optimum conditions can only be achieved if these settings are optimised iteratively.

Remarks

- If perfect congruence of SEM and FIB image is required the height adjustment and focussing have to be done as an iterative process.

- The relative brightness of the SEM and FIB images can be changed by choosing different SEM probe currents. Sometimes it may still be useful to blank the SEM beam. For this task the blanker cable has to be installed, the blanker unit switched on and the knob set to JSM 6100. Now the Elphy Plus software can be used to communicate with the SEM.

B.4   FIB operation with the Elphy Plus software

Operating the FIB with Elphy Plus is necessary for patterns which are more complicated than a single line or single box. In preparation following steps have to be executed:

- set the FIB magnification to 1

- blank SEM with the Elphy plus software

- switch the FIB control from **SEM** to **EXTERNAL** and the blanking control in the right panel of the FIB software from **NONE** to **SOURCE**

- set FIB attenuation to 1 (In the **EXTERNAL** mode the attenuation denotes the magnification of the FIB column.)

- set the rotary switch to FIB

Now the Elphy plus software takes control over the FIB and the electron beam is blanked by default. If this is unfavourable, the beam blanker has to be disconnected again from the SEM. Since the blanking of Elphy plus is still activated the FIB beam remains blanked even when the beam is switched on in the FIB software.

According to the standard procedures, which are described in detail in the Raith manual, the exposure process is prepared. For the FIB just one writefield of $400 \times 400~\mu\text{m}^2$ has been defined. It is called by choosing writefield size 400 and magnification 1. To achieve optimum resolution of the FIB system, the FIB attenuation should be set to a minimum value of 10. At this point the optics has just switched to a state with an additional cross-over. Consequently, the writefield size for this setting is reduced to $40 \times 40~\mu\text{m}^2$ and the parameters in the Elphy plus layouts are reduced by the attenuation factor.

Typical exposure parameters for attenuation 10 are:

- step size: 0.01 μm

- dwell time: 0.01 to 0.05 ms

- no. of cycles: 1 to 10

- probe current measurement is lacking
  $\rightarrow$ area dose is not defined

Remarks

- If the duration of writing one line exceeds 1 s a system hang up may occur, which is caused by a Windows NT time out at the SCSI interface. This problem can be circumvented by using more cycles or by placing several structures on top of each other.

- The written structures are rotated by 180° with respect to the structure layout in the Elphy Plus software.

B.5   System shut-down

To shut down the system, the ion beam is blanked in the FIB software, **EX-TERNAL** is changed to **SEM** and **SOURCE** to **NONE**. It is advisable to save the current operating conditions as starting values for a later use. In the **ION GUN** dialog the extraction is slowly reduced to zero, followed by pressing **SHUTDOWN**.

CLOSE THE FIB VALVE (!!!)

and terminate the program. Now the Elphy software is redirected to control the SEM by setting the rotary switch to JSM6100. Before terminating the software remember to

DEACTIVATE THE BLANKING.

The stage tilt is set back to $0°$. To facilitate the next start-up, the magnification should be reduced to its minimum value followed by a rough adjustment of the focus. Subsequently, the filament current is reduced to about 100 μA, HV and filament are switched off.

WAIT A FEW MINUTES

before removing the sample. Allowing the filament to cool down is important otherwise the filament lifetime is much shorter. For removing the sample refer to section B.1.

Bibliography

[1] Cypress, www.cypress.com.

[2] S. Zankovych, T. Hoffmann, J. Seekamp, J.-U. Bruch, and C. M. Sotomayor Torres, Nanotechnology **12**, 91 (2001).

[3] J. Jorritsma, M. A. M. Gijs, J. M. Kerkhof, and J. G. H. Stienen, Nanotechnology **7**, 263 (1996).

[4] A. Fernandez, M. R. Gibbons, M. A. Wall, and C. J. Cerjan, J. Magn. Magn. Mater. **190**, 71 (1998).

[5] I. W. Hamley, Nanotechnology **14**, R39 (2003).

[6] R. P. Cowburn and M. E. Welland, Science **287**, 1466 (2000).

[7] K. Kobayashi, T. Kimura, H. Sawada, K. Terakura, and Y. Tokura, Nature (London) **395**, 677 (1998).

[8] D. D. Sarma, P. Mahadevan, T. Saha-Dasgupta, S. Ray, and A. Kumar, Phys. Rev. Lett. **85**, 2549 (2000).

[9] Z. Fang, K. Terakura, and J. Kanamori, Phys. Rev. B **63**, 180407 (2001).

[10] A. A. Aligia, P. Petrone, J. O. Sofo, and B. Alascio, Phys. Rev. B **64**, 092414 (2001).

[11] T. Saitoh, M. Nakatake, A. Kakizaki, H. Nakajima, O. Morimoto, S. Xu, Y. Morimoto, N. Hamada, and Y. Aiura, Phys. Rev. B **66**, 035112 (2002).

[12] O. Chmaissem, R. Kruk, B. Dabrowski, D. E. Brown, X. Xiong, S. Koslenik, J. D. Jorgensen, and C. W. Kimball, Phys. Rev. B **62**, 14197 (2000).

[13] C. Zener, Phys. Rev. **82**, 403 (1951).

[14] J. Lindén, T. Yamamoto, M. Karppinen, H. Yamauchi, and T. Pietari, Appl. Phys. Lett. **76**, 2925 (2000).

[15] J. M. Greneche, M. Venekatesan, R. Suryanarayanan, and J. M. D. Coey, Phys. Rev. B **63**, 174403 (2001).

[16] M. Tovar, M. T. Causa, A. Butera, J. Navarro, B. Martinez, J. Fontcuberta, and M. C. G. Passeggi, Phys. Rev. B **66**, 024409 (2002).

[17] M. Retuerto, J. A. Alonso, M. J. Martínez-Lope, J. L. Martínez, and M. García-Hernández, Appl. Phys. Lett. **85**, 266 (2004).

[18] L. Balcells, J. Navarro, M. Bibes, A. Roig, B. Martínez, and J. Fontcuberta, Appl. Phys. Lett. **78**, 781 (2001).

[19] J. B. MacChesney, R. C. Sherwood, and J. F. Potter, J. Chem. Phys. **43**, 1907 (1965).

[20] J. B. Goodenough, Phys. Rev. **171**, 466 (1968).

[21] M. Wojcik, E. Jedryka, S. Nadolski, J. Navarro, and J. Fontcuberta, J. Magn. Magn. Mater. **272-276**, 1834 (2004).

[22] Y. Tomioka, T. Okuda, Y. Okimoto, R. Kumai, K.-I. Kobayashi, and Y. Tokura, Phys. Rev. B **61**, 422 (2000).

[23] H. Yanagihara, M. B. Salamon, Y. Lyanda-Geller, S. Xu, and Y. Moritomo, Phys. Rev. B **64**, 214407 (2001).

[24] J. Ye, Y. B. Kim, A. J. Millis, B. I. Shraiman, P. Majumdar, and Z. Tešanović, Phys. Rev. Lett. **83**, 3737 (1999).

[25] S. H. Chun, M. B. Salamon, and P. D. Han, Phys. Rev. B **59**, 11155 (1999).

[26] T. Saha-Dasgupta and D. D. Sarma, Phys. Rev. B **64**, 064408 (2001).

[27] J. Navarro, C. Frontera, L. Barcells, B. Martínez, and J. Fontcuberta, Phys. Rev. B **64**, 092411 (2001).

[28] N. D. Mathur, G. Burnell, S. P. Isaac, T. Jackson, B. S. Teo, J. L. MacManus-Driscoll, L. F. Cohen, J. Evetts, and M. G. Blamire, Nature (London) **387**, 266 (1997).

[29] K. Steenbeck, T. Eick, K. Kirsch, H.-G. Schmidt, and E. Steinbeiß, Appl. Phys. Lett. **73**, 2506 (1998).

[30] S. P. Isaac, N. D. Mathur, J. E. Evetts, and M. G. Blamire, Appl. Phys. Lett. **72**, 2038 (1998).

[31] W. Westerburg, F. Martin, S. Friedrich, M. Maier, and G. Jakob, J. Appl. Phys. **86**, 2173 (1999).

[32] N. Auth, Master's thesis, Johannes Gutenberg-Universität Mainz, 2001.

[33] T. H. Kim, M. Uehara, and S.-W. Cheong, Appl. Phys. Lett. **74**, 1737 (1999).

[34] D. Niebieskikwiat, A. Caneiro, R. D. Sánchez, and J. Fontcuberta, Phys. Rev. B **64**, 180406R (2001).

[35] T. Manako, M. Izumi, Y. Konishi, K.-I. Kobayashi, M. Kawasaki, and Y. Tokura, Appl. Phys. Lett. **74**, 2215 (1999).

[36] H. Asano, S. B. Ogale, J. Garrison, A. Orozco, Y. H. Li, E. Li, V. Smolyaninova, C. Galley, M. Downes, M. Rajeswari, R. Ramesh, and T. Venkatesan, Appl. Phys. Lett. **74**, 3696 (1999).

[37] H. Q. Yin, J.-S. Zhou, J.-P. Zhou, R. Dass, J. T. McDevitt, and J. B. Goodenough, Appl. Phys. Lett. **75**, 2812 (1999).

[38] M. Besse, F. Pailloux, A. Barthélémy, K. Bouzehouane, A. Fert, J. Olivier, O. Durand, F. Wyczisk, R. Bisaro, and J.-P. Contour, J. Cryst. Growth **241**, 448 (2002).

[39] S. R. Shinde, S. B. Ogale, R. L. Greene, T. Venkatesan, K. Tsoi, S.-W. Cheong, and A. J. Millis, J. Appl. Phys. **93**, 1605 (2003).

[40] A. Venimadhav, F. Sher, J. P. Attfield, and M. G. Blamire, J. Magn. Magn. Mater. **269**, 101 (2004).

[41] M. Kawasaki, K. Takahashi, T. Maeda, R. Tsuchiya, M. Shinohara, O. Ishiyama, T. Yonezawa, M. Yoshimoto, and H. Koinuma, Science **266**, 1540 (1994).

[42] G. Koster, B. L. Kropman, G. J. H. L. Rijnders, D. H. A. Blank, and H. Rogalla, Appl. Phys. Lett. **73**, 2920 (1998).

[43] T. Fix, G. Versini, J. L. Loison, S. Colis, G. Schmerber, G. Pourroy, and A. Dinia, J. Appl. Phys. **97**, 024907 (2005).

[44] H. Asano, Y. Kohara, and M. Matsui, Jpn. J. Appl. Phys. **41**, L 1081 (2002).

[45] J. Rodríguez-Carvajal, Physica B **192**, 55 (1993).

[46] Z.-G. Ban and S. P. Alpay, J. Appl. Phys. **91**, 9288 (2002).

[47] W. Pies and A. Weiss, *Crystal Structure Data of Inorganic Compounds*, Vol. 7e of *Landolt-Börnstein* (Springer-Verlag, Heidelberg, 1977), p. 13.

[48] J. H. Haeni, Ph.D. thesis, Pennsylvania State University, 2002.

[49] G. Shirane, Rev. Mod. Phys. **46**, 437 (1974).

[50] M. García-Hernández, J. L. Martínez, M. J. Martínez-Lope, M. T. Casais, and J. A. Alonso, Phys. Rev. Lett. **86**, 2443 (2001).

[51] L. J. van der Pauw, Philips Res. Repts **13**, 1 (1958).

[52] D. K. de Vries and A. D. Wieck, Am. J. Phys. **63**, 1074 (1995).

[53] J. P. Zhou, R. Dass, H. Q. Yin, J.-S. Zhou, L. Rabenberg, and J. B. Goodenough, J. Appl. Phys. **87**, 5037 (2000).

[54] I. A. Campbell and A. Fert, in *Ferromagnetic Materials*, edited by E. P. Wohlfarth (North-Holland Physics Publishing, Amsterdam, 1987), Vol. 3, pp. 757–758.

[55] K. Kubo and N. Ohata, J. Phys. Soc. Jpn. **33**, 21 (1972).

[56] X. Wang and X.-G. Zhang, Phys. Rev. Lett. **82**, 4276 (1999).

[57] G. Zhao, V. Smolyaninova, W. Prellier, and H. Keller, Phys. Rev. Lett. **84**, 6086 (2000).

[58] J. Kondo, Prog. Theor. Phys. **32**, 37 (1964).

[59] E. Rozenberg, M. Auslender, I. Felner, and G. Gorodetsky, J. Appl. Phys. **88**, 2578 (2000).

[60] B. L. Altshuler and A. G. Aronov, Sov. Phys. JETP **50**, 968 (1979).

[61] I. L. Aleiner, B. L. Altshuler, and M. E. Gershenson, Waves Random Media **9**, 201 (1999).

[62] D. Reisinger, Master's thesis, Johannes Gutenberg-Universität Mainz, 2000.

[63] J. S. Moodera, L. R. Kinder, J. Nowak, P. LeClair, and R. Meservey, Appl. Phys. Lett. **69**, 708 (1996).

[64] J. M. DeTeresa, A. Barthélémy, A. Fert, J. P. Contour, F. Montaigne, and P. Seneor, Science **286**, 507 (2003).

[65] P. D. Johnson, Rep. Prog. Phys. **60**, 1217 (1997).

[66] A. Damascelli, Z. Hussain, and Z.-X. Shen, Phys. Rev. B **48**, 1337 (1993).

[67] G. A. de Wijs and R. A. de Groot, Phys. Rev. B **64**, 020402R (2001).

[68] S. Picozzi, A. Continenza, and A. J. Freeman, J. Appl. Phys. **94**, 4723 (2003).

[69] P. M. Tedrow and R. Meservey, Phys. Rev. Lett. **26**, 192 (1971).

[70] R. Meservey and P. M. Tedrow, Phys. Rep. **238**, 173 (1994).

[71] C. T. Tanaka, J. Nowak, and J. S. Moodera, J. Appl. Phys. **86**, 6239 (1999).

[72] D. C. Worledge and T. H. Geballe, Phys. Rev. B **62**, 447 (2000).

[73] R. J. Soulen Jr., J. M. Byers, M. S. Osofsky, B. Nadgorny, T. Ambrose, S. F. Cheng, P. R. Broussard, C. T. Tanaka, J. Nowak, J. S. Moodera, A. Barry, and J. M. D. Coey, Science **282**, 85 (1998).

[74] K. Upadhyay, A. Palanisami, R. N. Louie, and R. A. Buhrman, Phys. Rev. Lett. **81**, 3247 (1998).

[75] Y. Tomioka, A. Asamitsu, and Y. Tokura, Phys. Rev. B **63**, 24421 (2000).

[76] W. Westerburg, F. Martin, P. J. M. van Bentum, J. A. A. J. Perenboom, and G. Jakob, Eur. Phys. J. B **14**, 509 (2000).

[77] Y. Moritomo, S. Xu, T. Akimoto, A. Machida, N. Hamada, K. Ohoyama, E. Nishibori, M. Takata, and M. Sakata, Phys. Rev. B **62**, 14224 (2000).

[78] W. Westerburg, D. Reisinger, and G. Jakob, Phys. Rev. B **62**, 767 (2000).

[79] G. Wexler, Proc. Phys. Soc. (London) **89**, 927 (1966).

[80] K. Gloos, F. B. Anders, B. Buschinger, C. Geibel, K. Heuser, F. Jährlich, J. S. Kim, R. Klemens, R. Müller-Reisener, C. Schank, and G. R. Steward, J. Low Temp. Phys. **105**, 37 (1996).

[81] I. Žutić and O. Valls, Phys. Rev. B **61**, 1555 (2000).

[82] D. C. Worledge and T. H. Geballe, Phys. Rev. Lett. **85**, 5182 (2000).

[83] B. Nadgorny, I. I. Mazin, M. S. Osofsky, R. J. S. Jr., P. Broussard, R. M. Stroud, D. J. Singh, V. G. Harris, A. Arsenov, and Y. Mukovskii, Phys. Rev. B **63**, 184433 (2001).

[84] B. Nadgorny, M. S. Osofsky, D. J. Singh, G. T. Woods, R. J. S. Jr., M. K. Lee, S. D. Bu, and C. B. Eom, Appl. Phys. Lett. **82**, 427 (2003).

[85] I. I. Mazin, Phys. Rev. Lett. **83**, 1427 (1999).

[86] G. E. Blonder, M. Tinkham, and T. M. Klapwijk, Phys. Rev. B **25**, 4515 (1982).

[87] G. J. Strijkers, Y. Ji, F. Y. Yang, C. L. Chien, and J. M. Byers, Phys. Rev. B **63**, 104510 (2001).

[88] I. I. Mazin, A. A. Golubov, and B. Nadgorny, J. Appl. Phys. **89**, 7576 (2001).

[89] C. W. J. Beenakker, Rev. Mod. Phys. **69**, 731 (1997).

[90] http://www.mathworks.com/.

[91] G. T. Woods, R. J. Soulen Jr., I. I. Mazin, B. Nadgorny, M. S. Osofsky, J. Sanders, H. Srikanth, and W. F. Egelhoff, Phys. Rev. B **70**, 054416 (2004).

[92] R. Holm, *Electric Contacts Handbook*, 3. ed. (Springer, Berlin, Göttingen, Heidelberg, 1958), pp. 65–70.

[93] T. Becherer, Master's thesis, Technische Hochschule Darmstadt, 1990.

[94] Y. Ji, C. L. Chien, Y. Tomioka, and Y. Tokura, Phys. Rev. B **66**, 012410 (2002).

[95] C. H. Kant, O. Kurnosikov, A. T. Filip, P. LeClair, H. J. M. Swagten, and W. J. M. de Jonge, Phys. Rev. B **66**, 212403 (2002).

[96] I. Galanakis, P. H. Dederichs, and N. Papanikolaou, Phys. Rev. B **66**, 174429 (2002).

[97] C. Felser, B. Heitkamp, F. Kronast, D. Schmitz, S. Cramm, H. A. Dürr, H.-J. Elmers, G. Fecher, S. Wuhrmehl, T. Block, D. Valdaitsev, S. A. Nepijko, A. Gloskovskii, G. Jakob, G. Schönhense, and W. Eberhardt, J. Phys.: Condens. Matter **15**, 7019 (2003).

[98] T. Block, Ph.D. thesis, Universität Mainz, 2002.

[99] M. S. Osofsky, B. Nadgorny, R. J. Soulen, Jr., G. Trotter, P. Broussard, W. Desisto, G. Laprade, Y. M. Mukovskii, and A. Arsenov, Physica C **341-348**, 1527 (2000).

[100] R. P. Panguluri, B. Nadgorny, T. Wojtowicz, W. L. Lim, X. Liu, and J. K. Furdyna, Appl. Phys. Lett. **84**, 4947 (2004).

[101] S. Wurmehl, Master's thesis, Johannes Gutenberg-Universität Mainz, 2002.

[102] H. J. Elmers, G. H. Fecher, D. Valdaitsev, S. A. Nepijko, A. Gloskovskii, G. Jakob, G. Schönhense, S. Wurmehl, T. Block, C. Felser, P.-C. Hsu, W.-L. Tsai, and S. Cramm, Phys. Rev. B **67**, 104412 (2003).

[103] Y. Ji, G. J. Strijkers, F. Y. Yang, C. L. Chien, J. M. Byers, A. Anguelouch, G. Xiao, and A. Gupta, Phys. Rev. Lett. **86**, 5585 (2001).

[104] Y. Ji, G. J. Strijkers, F. Y. Yang, and C. L. Chien, Phys. Rev. B **64**, 224425 (2001).

[105] M. Fehringer, F. Rüdenauer, and W. Steiger, *Space-proven indium liquid metal field ion emitters for ion microthruster applications*, 33rd AIAA Joint Propulsion Conference, 1997.

[106] M. A. McCord and M. J. Rooks, in *Handbook of Microlithography, Micromachining and Microfabrication*, edited by P. Rai-Choudhury (SPIE Optical Engineering Press, Bellingham, 1994), Vol. 1, Chap. 2.

[107] I. Haller, M. Hatzakis, and R. Srinivasan, IBM J. Res. Develop. **12**, 251 (1968).

[108] C. G. Willson, in *Introduction to Microlithography, ACS symposium Series 219*, edited by L. F. Thompson, C. G. Willson, and M. J. Bowden (American Chemical Society, Washington D. C., 1983), p. 124.

[109] *NANO PMMA and Copolymer*, MicroChem Corp., 2001.

[110] R. J. Hawryluk, J. Vac. Sci. Technol. **19**, 1 (1981).

[111] J. I. Goldstein, D. E. Newbury, P. Echlin, D. C. Joy, C. Fiori, and E. Lifshin, in *Scanning Electron Microscopy and X-Ray Microanalysis* (Plenum Press, New York and London, 1981), p. 57.

[112] M. Parikh, J. Appl. Phys. **50**, 4371, 4378 and 4383 (1979).

[113] I. Adesida, E. Everhart, and R. Shimizu, J. Vac. Sci. Technol. **16**, 1743 (1979).

[114] J. S. Greeneich, J. Vac. Sci. Technol. **16**, 1749 (1979).

[115] N. A. Usov and S. E. Peschany, J. Magn. Magn. Mater. **130**, 275 (1994).

[116] M. R. Scheinfein, http://llgmicro.home.mindspring.com/.

[117] R. P. Cowburn, J. Phys. D: Appl. Phys. **33**, R1 (2000).

[118] R. P. Cowburn, D. K. Koltsov, A. O. Adeyeye, M. E. Welland, and D. M. Tricker, Phys. Rev. Lett. **83**, 1042 (1999).

[119] R. Höllinger, A. Killinger, and U. Krey, J. Magn. Magn. Mater. **261**, 178 (2003).

[120] R. P. Cowburn, A. O. Adeyeye, and M. E. Welland, New J. Phys. **1**, 16.1 (1999).

[121] N. A. Usov, C.-R. Chang, and Z.-H. Wei, J. Appl. Phys. **89**, 7591 (2001).

[122] Z.-H. Wei, M.-F. Lai, C.-R. Chang, N. A. Usov, J. C. Wu, and J.-Y. Lai, https://gra103.aca.ntu.edu.tw/gdoc/D90222026a.pdf (2003).

[123] J. A. Johnson, M. Grimsditch, V. Metlushko, P. Vavassori, B. Ilic, P. Neuzol, and R. Kumar, Appl. Phys. Lett. **77**, 4410 (2000).

[124] M. Gacic, Master's thesis, Johannes Gutenberg-Universität Mainz, 2004.

[125] M. Kallmayer, Master's thesis, Johannes Gutenberg-Universität Mainz, 2003.

[126] K. J. Kirk, J. N. Chapman, and C. D. W. Wilkinson, Appl. Phys. Lett. **71**, 539 (1997).

[127] Motorola, *Motorola Produces World's First 4 Mbit MRAM Chip, Honeywell Licenses Motorola's MRAM Technology to Develop Non-Volatile Aerospace Memory Component*, http://www.motorola.com/mediacenter.

List of Publications

Pulsed laser deposition of Sr_2FeMoO_6 thin films
D. SÁNCHEZ, N. AUTH, G. JAKOB, J. L. MARTÍNEZ, AND
M. GARCÍA-HERNÁNDEZ
J. Magn. Magn. Mater. **294**, e119–e122 (2005).

Thin epitaxial films of the Heusler compound $Co_2Cr_{0.6}Fe_{0.4}Al$
G. JAKOB, F. CASPER, V. BEAUMONT, S. FALK, N. AUTH, H.-J. ELMERS,
C. FELSER, AND H. ADRIAN
Proceedings of the **J**oint **E**uropean **M**agnetic **S**ymposia 2004, Dresden, Germany
J. Magn. Magn. Mater. **290–291**, e1104–e1107 (2005).

Structural, magnetic, and transport properties of high-quality epitaxial Sr_2FeMoO_6 thin films prepared by pulsed laser deposition
D. SÁNCHEZ, M. GARCÍA-HERNÁNDEZ, N. AUTH, AND G. JAKOB
J. Appl. Phys. **96**, 2736–2742 (2004).

Crystal Structure and magnetism of the double perovskites A_2FeReO_6 (A=Ca, Sr, Ba)
N. AUTH, G. JAKOB, W. WESTERBURG, C. RITTER, I. BONN, C. FELSER,
AND W. TREMEL
Proceedings of the **I**nternational **C**onference on **M**agnetism 2003, Rome, Italy
J. Magn. Magn. Mater. **272–276**, e607–e608 (2004).

Spin polarization of magnetoresistive materials by point contact spectroscopy
N. AUTH, G. JAKOB, T. BLOCK, AND C. FELSER
Phys. Rev. B **68**, 024403 (2003).

Magnetotransport Properties of Thin Films of Magnetic Perovskites
G. JAKOB, W. WESTERBURG, F. MARTIN, D. REISINGER, AND N. AUTH
Advances in Solid State Physics **41**, 589 (2001).